



TITLE:

# Multiscale and hierarchical reaction mechanism in a lithium-ion battery

AUTHOR(S):

Orikasa, Yuki; Yamamoto, Kentaro; Shimizu, Takeshi; Uchimoto, Yoshiharu

---

CITATION:

Orikasa, Yuki ...[et al]. Multiscale and hierarchical reaction mechanism in a lithium-ion battery. *Chemical Physics Reviews* 2022, 3(1): 011305.

ISSUE DATE:

2022-03

URL:

<http://hdl.handle.net/2433/278909>

RIGHT:

© 2022 Author(s); All article content, except where otherwise noted, is licensed under a Creative Commons Attribution (CC BY) license.


# Multiscale and hierarchical reaction mechanism in a lithium-ion battery F

Cite as: Chem. Phys. Rev. **3**, 011305 (2022); <https://doi.org/10.1063/5.0062329>

Submitted: 04 July 2021 • Accepted: 30 December 2021 • Published Online: 02 February 2022

 Yuki Oriksa,  Kentaro Yamamoto,  Takeshi Shimizu, et al.

## COLLECTIONS

 This paper was selected as Featured



View Online



Export Citation



CrossMark

## ARTICLES YOU MAY BE INTERESTED IN

[Fundamentals of metal oxide/oxyfluoride electrodes for Li-/Na-ion batteries](#)

Chemical Physics Reviews **2**, 041306 (2021); <https://doi.org/10.1063/5.0052741>

[Perspectives for next generation lithium-ion battery cathode materials](#)

APL Materials **9**, 109201 (2021); <https://doi.org/10.1063/5.0051092>

[Machine learning on neutron and x-ray scattering and spectroscopies](#)

Chemical Physics Reviews **2**, 031301 (2021); <https://doi.org/10.1063/5.0049111>

Learn More

The Journal of Chemical Physics **Special Topics** Open for Submissions

# Multiscale and hierarchical reaction mechanism in a lithium-ion battery

 Cite as: Chem. Phys. Rev. **3**, 011305 (2022); doi: [10.1063/5.0062329](https://doi.org/10.1063/5.0062329)

Submitted: 4 July 2021 · Accepted: 30 December 2021 ·

Published Online: 2 February 2022



View Online



Export Citation



CrossMark

 Yuki Orika<sup>s,a)</sup>  Kentaro Yamamoto,<sup>2</sup>  Takeshi Shimizu,<sup>1</sup>  and Yoshiharu Uchimoto<sup>2</sup> 

## AFFILIATIONS

<sup>1</sup>Department of Applied Chemistry, College of Life Sciences, Ritsumeikan University, 1-1-1 Noji Higashi, Kusatsu, Shiga 525-8577, Japan

<sup>2</sup>Graduate School of Human and Environmental Studies, Kyoto University, Yoshida-nihonmatsucho, Sakyo-ku, Kyoto 606-8501, Japan

<sup>a)</sup>Author to whom correspondence should be addressed: [orikasa@fc.ritsumei.ac.jp](mailto:orikasa@fc.ritsumei.ac.jp)

## ABSTRACT

The key to improving the performance of lithium-ion batteries is to precisely elucidate the temporal and spatial hierarchical structure of the battery. Lithium-ion batteries consist of cathodes and anodes and a separator containing an electrolyte. The cathodes and anodes of lithium-ion batteries are made of a composite material consisting of an active material, a conductive material, and a binder to form a complex three-dimensional structure. The reaction proceeds as lithium ions are repeatedly inserted into and removed from the active material. Therefore, the lattice of the active material is restructured due to ion diffusion, which results in phase change. At the active material–electrolyte interface, the insertion and de-insertion of lithium ions proceed with the charge transfer reaction. The charge–discharge reaction of a lithium-ion battery is a nonequilibrium state due to the interplay of multiple phenomena. Analysis after disassembling a battery, which is performed in conventional battery research, does not provide an accurate understanding of the dominant factors of the reaction rate and the degradation mechanism, in some cases. This review introduces the results of research on the temporal and spatial hierarchical structure of lithium-ion batteries, focusing on *operando* measurements taken during charge–discharge reactions. Chapter 1 provides an overview of the hierarchical reaction mechanism of lithium-ion batteries. Chapter 2 introduces the *operando* measurement technique, which is useful for analysis. Chapter 3 describes the reaction at the electrode–electrolyte interface, which is the reaction field, and Chapter 4 discusses the nonequilibrium structural change caused by the two-phase reaction in the active material. Chapter 5 introduces the study of the unique reaction heterogeneity of a composite electrode, which enables practical energy storage. Understanding the hierarchical reaction mechanism will provide useful information for the design of lithium-ion batteries and next-generation batteries.

© 2022 Author(s). All article content, except where otherwise noted, is licensed under a Creative Commons Attribution (CC BY) license (<http://creativecommons.org/licenses/by/4.0/>). <https://doi.org/10.1063/5.0062329>

## TABLE OF CONTENTS

I. SPATIAL AND TEMPORAL SCALES OF THE REACTION IN LITHIUM-ION BATTERIES . . . . .	1
II. METHOD FOR <i>OPERANDO</i> X-RAY MEASUREMENT DURING CHARGE–DISCHARGE . . . . .	4
III. ELECTRODE–ELECTROLYTE INTERFACE . . . . .	7
IV. CRYSTAL AND ELECTRONIC STRUCTURE CHANGES OF ELECTRODE ACTIVE MATERIALS. . . . .	10
V. REACTION INHOMOGENEITY WITHIN A COMPOSITE ELECTRODE . . . . .	18
VI. SUMMARY . . . . .	28

## I. SPATIAL AND TEMPORAL SCALES OF THE REACTION IN LITHIUM-ION BATTERIES

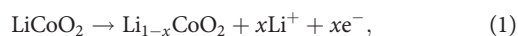
Lithium-ion batteries are not only globally utilized as a power source for laptops and smartphones but are also expected to be employed as a key large-scale energy storage device for promoting a carbon-free society. Therefore, lithium-ion batteries were the subject of the Nobel Prize in Chemistry in 2019, and research and development are actively conducted worldwide.<sup>1</sup>

Many technologies are incorporated into lithium-ion batteries, many of which are designed based on physicochemical reaction mechanisms.<sup>2–4</sup> To improve the performance of lithium-ion batteries

exhibiting higher performances, such as high energy density, durability, and safety, it is necessary to understand the hierarchical multiscale reaction that progresses sequentially in the device with respect to space and time. Since multiple reactions are intertwined in a nonequilibrium state in a lithium-ion battery, understanding the overall reaction mechanism leads to an accurate grasp of the factor governing the reaction kinetics and degradation mechanism.

A lithium-ion battery is an energy storage system in which lithium ions shuttle electrolytes between a cathode and an anode via a separator (Fig. 1). Chemical energy is stored by utilizing the redox reaction of electrode active materials, which involves the charge transfer between lithium ions and electrons at the electrode–electrolyte interface. Regarding the discharge reaction, lithium ions are removed from anodes by an oxidation reaction, and the lithium ions are transferred to the cathode side via the electrolyte. Additionally, electrons formed by the oxidation reaction of the anode also pass through the external circuit to the cathode. On the cathode side, a reduction reaction of active materials is caused by electrons and transferred lithium ions, which are inserted into active materials. In this way, the chemical energy can be converted into electrical energy during discharge. When charging, by connecting a power source to an external circuit, a reaction opposite to that at the time of discharge, that is, an oxidation reaction, occurs at the cathode, and a reduction reaction occurs at the anode. Lithium ions are transferred from the cathode to the anode; thus, electrical energy can be converted into chemical energy and stored in the battery.

At present, in a commonly used lithium-ion battery, lithium transition-metal oxide such as  $\text{LiCoO}_2$  is mainly used as a cathode active material,<sup>5</sup> and graphite is mainly used as an anode active material.<sup>6</sup> The chemical reaction formula at the time of charging these active materials is shown below



Although the above is the most basic chemical reaction proceeding in a cell, it is necessary to store a large amount of charge to use it as an actual device. Therefore, in commercialized lithium-ion batteries, the chemical reactions become complicated, and there are many factors affecting their performance. Figure 2 shows the reaction caused in lithium-ion batteries. The horizontal axis is represented by classifying the space scale, and the vertical axis is represented by the time scale for the reaction. The chemical reaction of the active material described above occurs at the interface where the electrode active material and electrolyte contact each other. At the electrode–electrolyte interface, which is the reaction starting point, the insertion and removal of lithium ions proceed with the desolvation reaction and charge transfer reaction, respectively. It is estimated that the region where the reaction proceeds is extremely narrow, in the range of several nanometers, and the reaction time is also extremely fast.<sup>7,8</sup>

At the electrode–electrolyte interface, desolvated lithium ions are inserted into the active material. In the cathode active material, lithium ions are inserted when the material is discharged and are removed when charged. In the active material, the rearrangement of the lattice by ion diffusion occurs, and the crystal phase changes with this reaction. The dimension of the reaction, which corresponds to the particle size of the active material, is often several micrometers, and the reaction time in one particle is estimated to be approximately a few seconds from the reported diffusion coefficients.<sup>9,10</sup>

Many active materials need to be packed into one electrode sheet to incorporate the amount of charge that can be used for a long time in our daily life. Therefore, a composite electrode is used in which active materials, binder, and a conductive agent are mixed and pasted on current collectors. The thickness of this electrode is approximately  $100 \mu\text{m}$ .<sup>11</sup> When the charge–discharge reaction occurs, the reaction time is generally on the hour scale, depending on the conditions. The produced lithium-ion battery is located on the upper right of a large spatial and timescale and is incorporated into a sealed container by laminating a sheet consisting of a cathode, an anode and a separator

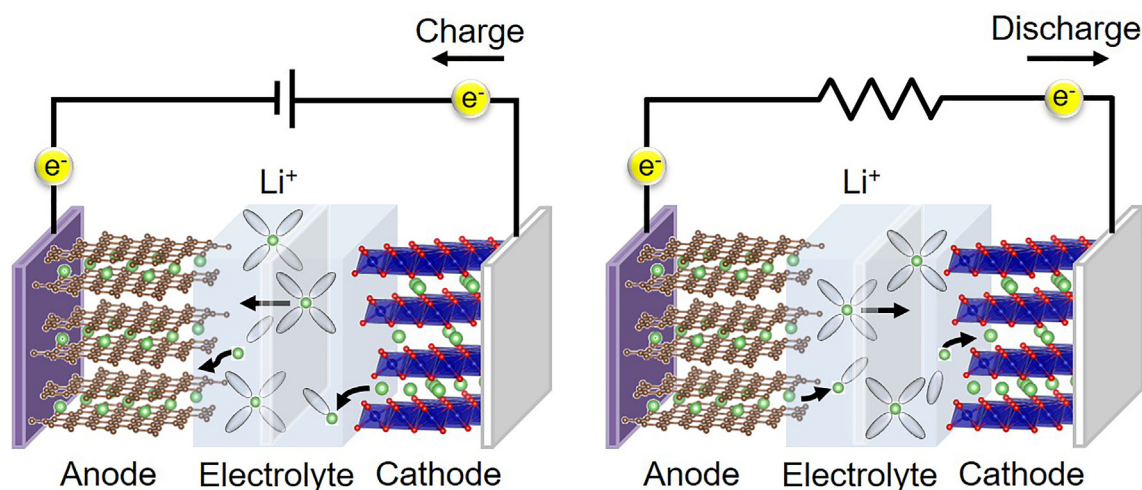


**FIG. 1.** Schematics of a lithium-ion battery. The cathode is transition metal oxide, the anode is graphite, and the electrolyte is a liquid of lithium salt dissolved in organic solvent. During charge, lithium is deinserted from the cathode and transferred to the anode through electrolyte, and at the same time, electrons are transferred in the external circuit by using the energy of the external power supply. During discharging reaction, electrons move in the opposite direction to extract energy, and lithium is deinserted from the anode and moves to the cathode.

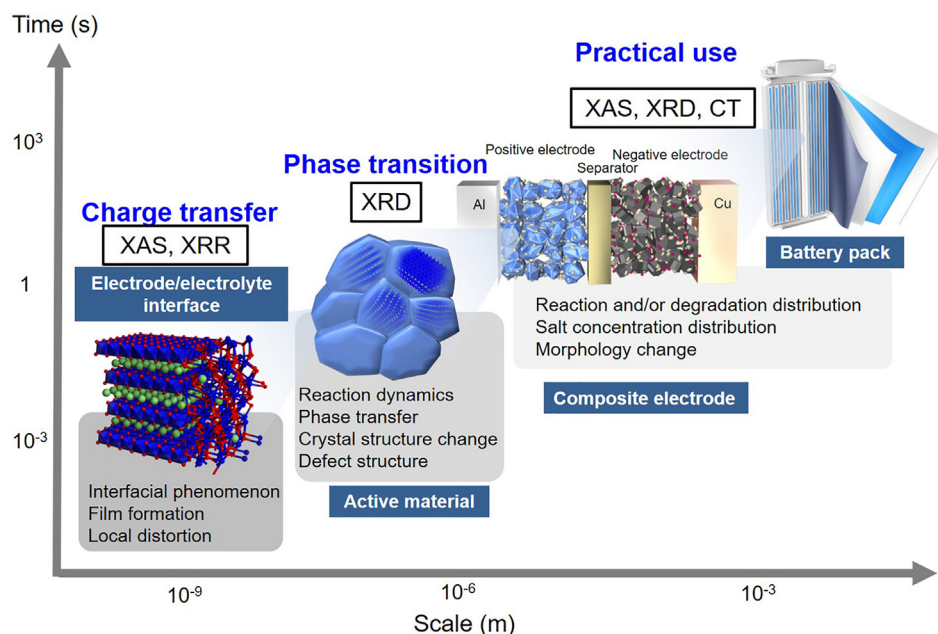


FIG. 2. Schematic diagram showing the spatial and temporal scales of the reaction in a lithium-ion battery. The representative techniques to analyze the reaction are also provided.

(including an electrolyte). The size of the 18 650 cell is 18 mm in diameter and 65 mm in length.

The size of lithium-ion batteries is on the order of centimeters at the pack level, and the charge–discharge reaction proceeds on the minute scale. On the other hand, the reaction proceeds on the order of several nanometers at the electrode–electrolyte interface. The timescale of the reaction also varies from minutes to milliseconds. The charge–discharge reaction requires the reaction to proceed on all scales, and when the reaction rate is disturbed in a certain part, that part becomes a rate-limiting process. Therefore, depending on the respective reaction scales, understanding the characteristic physicochemical reaction and elucidating the governing factor are key points in improving performance. However, it is difficult to elucidate all of the above hierarchical structures because lithium-ion batteries are not easy to visualize in sealed structures without cell disassembly. Furthermore, when the charge–discharge reaction is cycled, the labyrinth of the reaction processes is repeated. Such a nonequilibrium reaction makes it more difficult to grasp the phenomenon. Previous analyses have used disassembled battery cells in conventional battery research. The application of an *in situ* measuring method without disassembly and an *operando* measuring method in the battery–operating state is required because the factor governing the reaction rate and the degradation mechanism cannot be clearly grasped. By utilizing the strong transmittance of synchrotron radiation x rays, which exhibit high temporal and spatial resolutions, the temporal and spatial hierarchical structure of lithium-ion batteries can be measured *in situ* as the battery reaction proceeds. In this review, we focus on elucidating the hierarchical reaction mechanism of lithium-ion batteries using synchrotron x-ray analysis and explain the reaction mechanisms that greatly affect performance in regard to their respective scales.

Many techniques use synchrotron radiation x rays to measure lithium-ion batteries.<sup>12</sup> Table I shows the list of synchrotron-based analysis techniques and their advantages. Typical methods covered in

this review are x-ray absorption spectroscopy (XAS) and x-ray absorption fine structure (XAFS) analysis. By irradiating materials with an x ray and measuring the absorbance of x rays and/or x rays and electrons emitted from materials, electronic and structural information on the inside of the substance can be obtained. For example, when a material is irradiated by changing the energy of monochromatic x rays, a steep x-ray absorption phenomenon called an absorption edge is observed at a specific energy corresponding to contained atoms. In this phenomenon, electrons at the core level are excited by x rays and are transferred to vacant orbitals and/or energy bands beyond the Fermi level. By analyzing this absorption edge, which is called the XAFS, information on the electronic state of the absorbing atom and the coordination structure around the absorbing atom can be obtained. In particular, the spectrum near the absorption edge is called the x-ray absorption near edge structure (XANES), whereas the spectrum showing oscillations due to interference is called the broad x-ray absorption fine structure (EXAFS), which, compared to the absorption edge, is observed in the high-energy region of approximately 1 keV. From the former, knowledge on the electronic state of the absorbed atom can be obtained, and from the latter, information on the coordination structure around the absorbed atom can be drawn.<sup>13</sup>

Other typical techniques are x-ray diffraction (XRD) and x-ray scattering methods. After interacting with atoms and molecules, x rays diffract and scatter. The diffraction and scattering information provide clues about the structure of the material. Because x-ray diffraction and scattering methods are not limited by the energy of the absorption edge, it is possible to use high-energy x rays; for example, when using a high-energy x ray, such as 100 keV x rays, it is also possible to see the internal structure of a large-scale lithium-ion battery cell for automotive applications. Using imaging techniques detecting transmitted x rays to obtain information on the macroscopic structure of a cell has also recently become popular.<sup>14</sup>

**TABLE I.** List of synchrotron-based analysis technique with provided information, advantages and corresponding laboratory-based techniques.

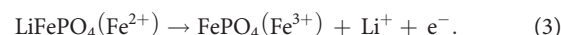
Synchrotron-based technique	Provided information	Advantage	Laboratory-based technique
X-ray absorption (XAS)	Electronic and local structure	No use in lab / Operando	Infrared spectroscopy / Raman scattering / Lab. XPS
X-ray photoelectron (XPS)	Electronic structure	High resolution / Quick measurement High energy	
Compton scattering	Electronic structure	No use in lab. / High energy	
X-ray diffraction (XRD)	Crystal structure	High resolution / Quick measurement	Lab XRD / Nuclear magnetic resonance
X-ray scattering	Chemical structure / Morphology	High resolution / Quick measurement	Lab x-ray scattering
X-ray reflectivity	Morphology	High resolution / Quick measurement	Lab x-ray reflectivity
X-ray microscopy	Morphology	Energy scan	Scanning electron microscopy
X-ray computed tomography (x-ray CT)	Morphology	Operando / High resolution	Transmission electron microscopy / Atomic force microscope / Lab. CT

## II. METHOD FOR OPERANDO X-RAY MEASUREMENT DURING CHARGE-DISCHARGE

This section explains the *operando* XAS setup using a laminated-type battery cell to obtain XAFS results during the operation of a lithium-ion battery. Figure 3(a) is an example of an Al laminate cell used in *operando* XAS at 6000 eV or higher, where the absorption of x rays by automorphic air is relatively low.<sup>15</sup> It is possible to apply a cell design similar to that used in the laboratory. To obtain high-quality data, it is considered that impurities in the components do not interfere with the acquisition of desired data. In some cases, the absorption of aluminum and copper current collectors becomes large, resulting in difficult measurements. The cell should be fixed with a jig, as shown in Fig. 3(b). The cell is placed between the ion chambers of the detector, and the electrochemical equipment is connected. *Operando* measurement becomes possible by simultaneously carrying out both charge-discharge and XAFS measurements. To precisely control the time scale, we should synchronize the x-ray optics system and electrochemical measurement system by a trigger signal.

Representative data from a laminate cell using LiFePO<sub>4</sub> as a cathode active material and Li metal as an anode is introduced. The Fe K-edge XAFS is continuously measured in the transmission mode during 1C charging, as shown in Fig. 3(c).<sup>16</sup> It takes 30 s to acquire one spectrum (in principle, the measurement technique speeds up the measurement time from milliseconds to picoseconds).<sup>17</sup> As the charge reaction proceeds, the absorption edge energy shifts to the higher energy side. In general, regarding the XANES results of a transition metal K-edge, an increased oxidation number results in a high energy shift.<sup>18</sup> This is because the decreased number of electrons decreases the level of the 1s orbital and the energy required for excitation increases. Therefore, K-edge XANES results can be used to indicate the valence state of the redox center. Edge shifting to high energy is observed because the charge reaction increases the amount of Fe<sup>3+</sup>-containing FePO<sub>4</sub>.<sup>19</sup> In addition, isosbestic points are found at approximately 7126 and 7155 eV. This means that the XANES spectra can be represented by two elements. By using the XANES spectra of LiFePO<sub>4</sub> and FePO<sub>4</sub>, the XANES spectrum of the charging process can be reproduced by the addition of both, which indicates the two-phase reaction in this charge reaction, and the ratio of the two phases can be calculated. The ratio of the two phases obtained in Fig. 3(d) is shown.

The value (plotted) calculated from the XANES results agrees with the two-phase ratio (dotted line) estimated from the charge capacity. This indicates that the movement of electrons is derived from the current, as shown in Eq. (3), and the valence change of Fe in the active material corresponds to a 1:1 ratio based on Faraday's law, showing that the reaction of both proceeds immediately on the second scale.<sup>16,19</sup>



Many groups have reported performing similar types of experiments using LiFePO<sub>4</sub> to obtain the two-phase ratio.<sup>20–22</sup> In some cases, the XANES results do not coincide with the two-phase ratio estimated from the charge-discharge capacity. Thus, the valence change in the active material may be delayed with respect to the current. However, due to the reaction inhomogeneity of the cell itself, there is also a possibility of a phenomenon occurring due to a delay in the reaction of the x-ray irradiated region. In recent years, many analyses have been conducted to investigate the inhomogeneous reaction in battery cells, particularly in LiFePO<sub>4</sub>.<sup>23,24</sup> In carrying out *operando* measurements, it is necessary to interpret the measurement results considering the possibility that such an inhomogeneous reaction occurs. *In situ* XANES of LiFePO<sub>4</sub> during chemical delithiation also indicates the quick response for electronic structure change.<sup>22</sup> The above-mentioned *operando* XAS technique is easy to perform if only x rays are transmitted. Similarly, if x-ray diffraction from the sample is detected, *operando* x-ray diffraction measurements are also conducted. *Operando* cells have been reported for battery research,<sup>20</sup> and the use of this method for analyzing electronic, local, and crystallographic structures during the charge-discharge process is becoming a convenient tool.

In the case of the 3d transition-metal oxides, the charge neutral condition after insertion and de-insertion of lithium ions seems to be maintained by the redox reaction of the transition metal. Actual electron transfer is contributed by the hybridized 3d orbital of the transition metal and 2p orbital of oxygen.<sup>25</sup> To realize more redox reactions, XANES of the transition-metal L-edge and oxygen K-edge, which can directly show these electronic structures near the Fermi level, have been discussed.<sup>26</sup>

We introduce one typical active material, LiNiO<sub>2</sub>. When the charge reaction proceeds, the Ni K-edge XANES is shifted toward high

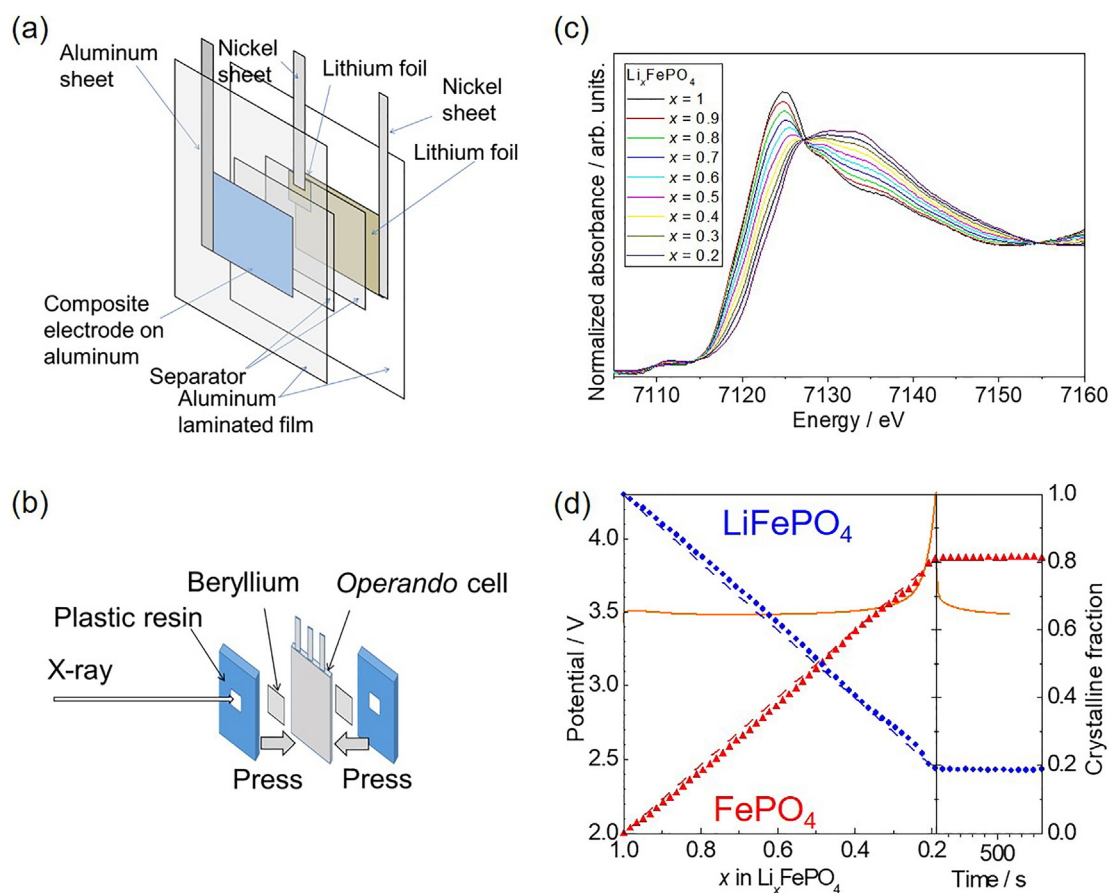


**FIG. 3.** Cells and representative data of *operando* x-ray absorption spectroscopy. (a) Cell configuration of an aluminum laminate cell for *operando* x-ray measurements. The same area of the  $\text{LiFePO}_4$  composite electrode and lithium counter electrode is utilized. If necessary, the lithium reference electrode can be placed between the two separators. These components are sealed by an aluminum-laminated film. (b) During *operando* x-ray measurements, the cell is fixed by using two beryllium sheets to equally press the electrode. X rays can pass through the beryllium window. Reprinted with permission from Orikasa *et al.*, *J. Electrochem. Soc.* **160**, A3061–A3065 (2013). Copyright 2013 IOP Publishing.<sup>15</sup> (c) Fe K-edge *operando* XANES spectrum during 1C charging and (d) the two-phase ratio of  $\text{LiFePO}_4$  and  $\text{FePO}_4$  from XANES (plotted) and current (dashed line). The charging reaction of  $\text{LiFePO}_4$  involves the oxidation reaction of iron. Since it is a two-phase reaction, the component ratios can be calculated by using the spectra of  $\text{LiFePO}_4$  and  $\text{FePO}_4$ . Reprinted with permission from Orikasa *et al.*, *Chem. Mater.* **25**, 1032–1039 (2013). Copyright 2013 American Chemical Society.<sup>16</sup>

energy, as shown in Fig. 4(a).<sup>27</sup> This is similar to  $\text{LiFePO}_4$  discussed above and is described in terms of Ni oxidation. However, this phenomenon is due to the change in the 1s orbital, and there is little information about the electron transfer in the outermost shell. XANES spectra of Ni L- and O K-edges are shown in Figs. 4(b) and 4(c), although the data are measured in *ex situ* conditions after charging.<sup>28</sup> While the Ni L-edge spectrum is unchanged at the early stage of charging, the change in the peak intensity at the O K-edge is large. The peak at 533 eV originating from the hybridization of Ni 3d and O 2p orbitals is reduced, and the peak at 528 eV originating from hole formation in O 2p orbitals is greatly increased. The results indicate that the redox reaction of nickel (change in the oxidation number of Ni) alters the electronic structure change of the hybridized orbital of nickel and oxygen to maintain charge-neutral conditions.

Recently, cathode materials with a high capacity using anion redox have been devised, and interesting charge–discharge properties have been reported in which only valence changes of transition metals cannot be explained.<sup>29–33</sup> It is important to clarify the electronic

structure changes of active materials, especially the electronic structure change of anions such as oxide ions, for the material design of next-generation high-capacity cathode materials.<sup>34,35</sup> Oishi *et al.* performed an electronic structure analysis of  $\text{Li}_2\text{MnO}_3$  and Li-excess layer oxides using XANES in the soft x-ray range, showing that an oxide ion contributes to charge compensation at high potential.<sup>36–38</sup> Yabuuchi *et al.* used the O K-edge XANES to investigate the “superoxide states” of cathode materials  $\text{Li}_{1.3}\text{Nb}_{0.3}\text{Mn}_{0.4}\text{O}_2$  and  $\text{Li}_{1.2}\text{Ti}_{0.4}\text{Mn}_{0.4}\text{O}_2$ , which differ from conventional materials in their charge process.<sup>33,39</sup> These XAS measurements were performed using samples after cell disassembly and washing without air exposure. The redox reaction of oxide ions occurs mainly on the high potential side during the charge–discharge process in a nonequilibrium state. Therefore, *operando* measurements performed under actual cell-operating conditions while irradiating x rays are useful for elucidating the reaction mechanisms.

Compared to the hard x-ray region measurable in the atmosphere, in the soft x-ray region of 3000 eV or less, the measurement environment is largely constrained, and it is difficult to directly apply

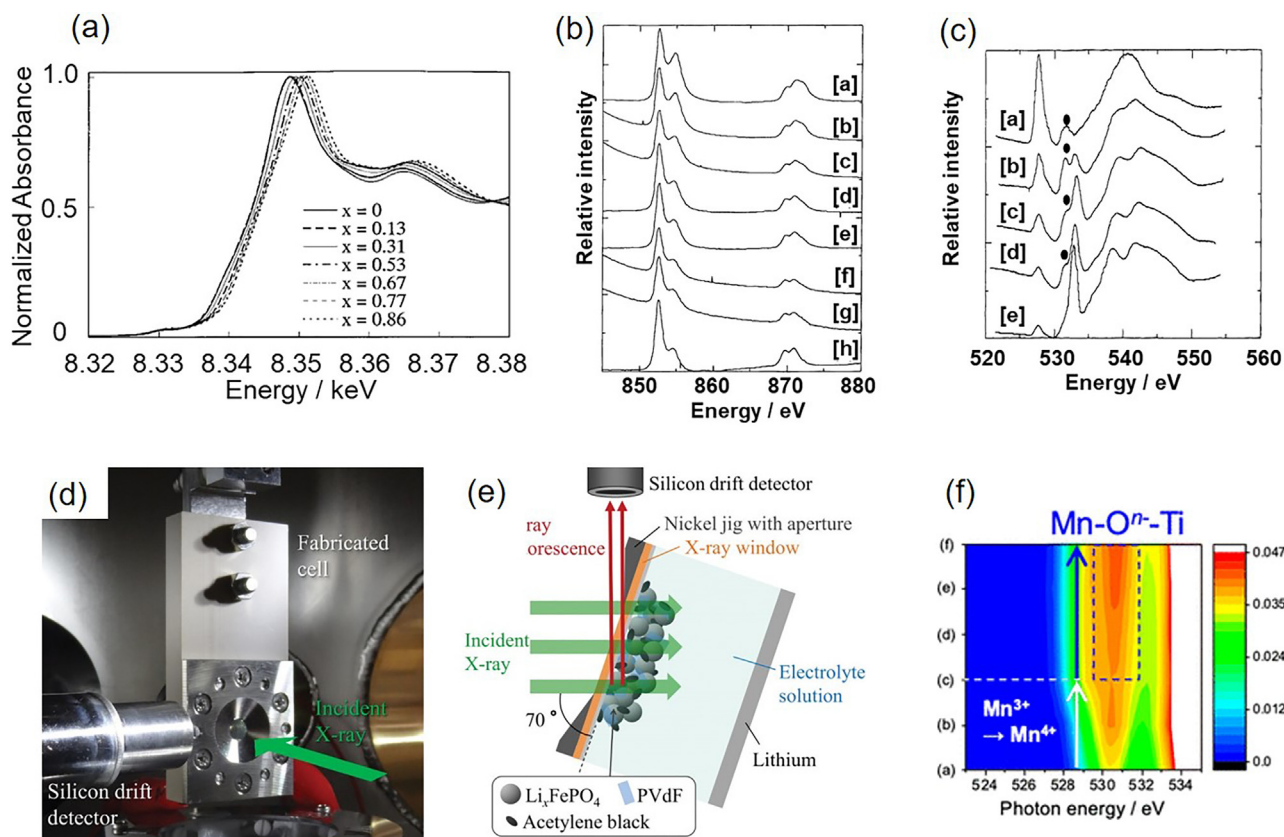


**FIG. 4.** X-ray absorption spectroscopic data studying charge compensation mechanism of lithium-ion battery cathodes. (a) Ni K-edge XANES spectra of  $\text{Li}_{1-x}\text{NiO}_2$ . As the composition of Li decreases in  $\text{Li}_{1-x}\text{NiO}_2$ , nickel is oxidized and the Ni K-edge absorption shifts to the high energy side. Reprinted with permission from Nakai *et al.*, *J. Solid State Chem.* **140**, 145–148 (1998). Copyright 1998 Elsevier.<sup>27</sup> (b) Ni L-edge XANES spectra of  $\text{Li}_x\text{NiO}_2$ , where  $x =$  (a) 0.8, (b) 0.6, (c) 0.5, (d) 0.4, (e) 0.3, (f) 0.2, (g) 0.1, and (h) 0. (c) O K-edge XANES spectra of  $\text{Li}_x\text{NiO}_2$ , where  $x =$  (a) 0.8, (b) 0.5, (c) 0.4, (d) 0.2, (e) 0. The peak at approximately 532 eV ( $\bullet$ ) is attributed to oxygen in the substrate. Ni L-edge reflecting Ni 3d orbitals shows a small change with respect to Li composition, while the O K-edge originating from O 2p orbitals shows a large increase or decrease in the peak. This indicates that the O 2p orbitals also contribute to the redox reaction associated with charging and discharging. Reprinted with permission from Uchimoto *et al.*, *J. Power Sources* **97–98**, 326–327 (2001). Copyright 2001 Elsevier.<sup>28</sup> Experimental setup for *operando* XAS measurement (d) in the high-vacuum sample chamber and (e) schematic top view. A window through which soft x rays are transmitted is attached to a sealed cell that can be operated in a vacuum chamber, and x rays are incident from the collector side to detect fluorescent x rays. Reprinted with permission from Nakanishi *et al.*, *Rev. Sci. Instrum.* **85**, 084103 (2014). Copyright 2014 American Institute of Publishing.<sup>40</sup> (f) *Operando* O K-edge XANES spectra of  $\text{Li}_{1.2}\text{Ti}_{0.4}\text{Mn}_{0.4}\text{O}_2$ . The peak at 530.7 eV is increased by charging. The *operando* soft x-ray absorption spectroscopy can clarify the contribution of anion redox by charging reaction. Reprinted with permission from Yamamoto *et al.*, *Chem. Mater.* **32**, 139–147 (2020). Copyright 2020 American Chemical Society.<sup>41</sup>

the cell as described above. In particular, no liquid electrolyte is available for measurement in a vacuum chamber. For this reason, a unique cell structure has been proposed in which cell components are separated between a vacuum and an atmospheric environment by using a window material through which x rays penetrate.<sup>40</sup> As shown in Figs. 4(d) and 4(e), the electrode-coated window and the electrolyte are placed in a sealable cell, which is brought into a vacuum chamber and irradiated with x rays through the window to detect fluorescence x rays. Using a SiN window enables the measurement of the O K-edge XANES spectrum of the electrode material during the charge-discharge reaction.

O K-edge XANES spectra of  $\text{Li}_{1.2-x}\text{Ti}_{0.4}\text{Mn}_{0.4}\text{O}_2$  during the initial charge process are shown in Fig. 4(f).<sup>41</sup> The pre-edge peak shifted toward lower energy in the initial stage of charging ( $x < 0.38$ ), after which a new peak appeared at 530.7 eV ( $x > 0.38$ ). Because Mn L-edge

XANES spectra show no change during the middle and later stages of charging ( $x > 0.38$ ), the change in the O K-edge XANES is attributed to the rehybridization of the 3d-2p orbitals of the Mn-O bond with the oxidation of Mn ( $x < 0.38$ ), and the change after  $x = 0.38$  is attributed to the charge compensation with oxide ions. The electronic structure between the transition metal and oxygen is a key point for the charge-compensation mechanism, and material design using oxygen redox is required while suppressing the release of oxygen gas.<sup>41</sup>

Although the electronic structure of active materials can be measured by photoelectron spectroscopy, *operando* measurement is difficult because it is a surface analysis performed under vacuum. The x-ray Compton scattering method measures the energy distribution that decreases when x-ray photons are scattered by electrons in a sample, reflecting the electron momentum of the sample and thus giving information on the electronic state.<sup>42</sup> Figure 5 shows the Compton



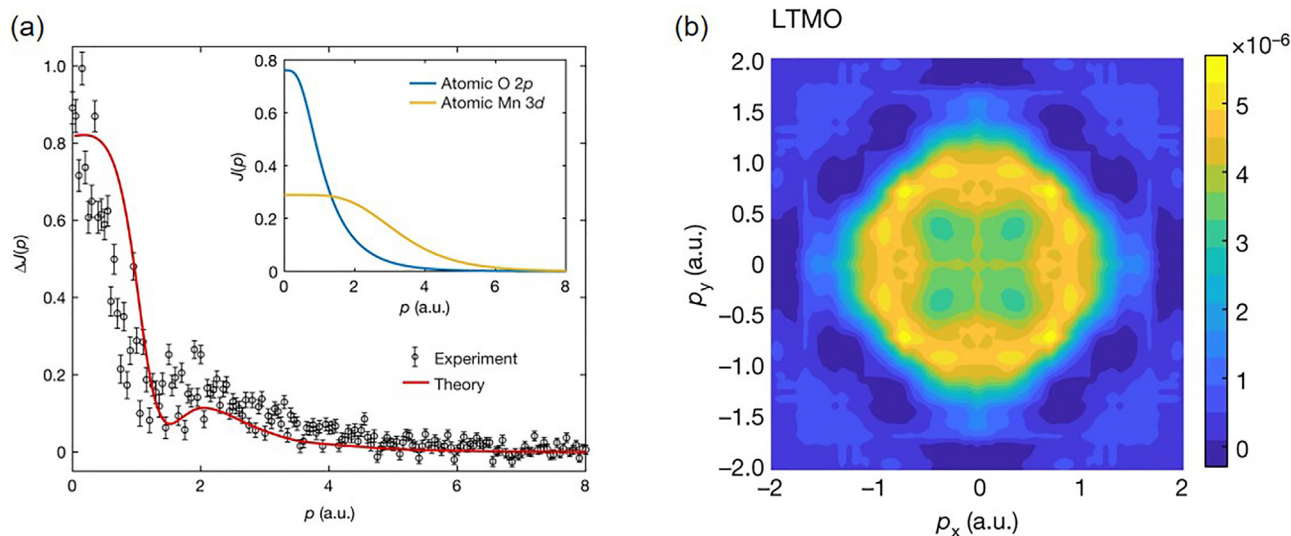


**FIG. 5.** Detection of charge compensation using oxygen 2p orbital by x-ray Compton scattering. (a) Compton profile difference corresponding to the difference in profiles of  $\text{Li}_x\text{Ti}_{0.4}\text{Mn}_{0.4}\text{O}_2$  (LTMO) for lithium concentrations ( $x$ ) of 0.8 and 0.4. (b) Map of the anionic redox orbitals in LTMO with concentrations between  $x = 0.8$  and  $x = 0.4$ . These figures show that when the lithium concentration of LTMO is changed, the change in Compton profile mainly originates from the oxygen 2p orbital, and indicate the dominant contribution of the anion redox. Reprinted with permission from Hafiz *et al.*, *Nature* **594**, 213–216 (2021). Copyright 2021 Springer Nature.<sup>43</sup>

scattering result of delithiated  $\text{Li}_{1.2-x}\text{Ti}_{0.4}\text{Mn}_{0.4}\text{O}_2$  and compares it with the first-principles computations, which reveal the charge-compensation contribution. The shape of Compton scattering is similar to that of oxygen 2p, revealing the dominant contribution of the oxygen orbital.<sup>43</sup> The use of high-energy x rays is advantageous for the *operando* measurement of lithium-ion batteries.<sup>44</sup>

### III. ELECTRODE-ELECTROLYTE INTERFACE

The origin of the overall reaction for lithium-ion batteries is charge transfer at the electrode–electrolyte interface. At the interface, due to the difference between the potential of the electrode and electrolyte, an electric double layer with a potential gradient is formed on the electrolyte side.<sup>45</sup> This electric double layer serves as a reaction field, where the migration and desolvation of ions proceed, followed by the change in the crystal structure of active materials.<sup>45</sup> On the other hand, even on the electrode side, a complex space charge layer is formed due to the potential difference.<sup>46</sup> In addition, the solid electrolyte interphase (SEI) produced by the decomposition of electrolytes further complicates the situation.<sup>47,48</sup> Analysis of the electrode–electrolyte interface is important in the development of lithium-ion batteries. Although AC impedance by electrochemistry is a simple and powerful tool to analyze phenomena at the electrode–electrolyte interface,<sup>49</sup> it is a numerical analysis of current and potential information and lacks information on the physicochemical structure at the interface. Therefore, the development of a technique that can directly observe the electrode–electrolyte interface is desired.

To clarify the interfacial phenomena, many studies on the surface of active materials have been carried out via *ex situ* methods. Regarding electrode active materials, surface effects on their charge–discharge properties can be analyzed using nanoparticles smaller than 20 nm.<sup>50–53</sup> For  $\text{LiCoO}_2$ , excess Li ions exist in the form of  $\text{Li}_{1+\delta}\text{Co}^{\text{II}}_{\delta}\text{Co}^{\text{III}}_{1-\delta}\text{O}_2$  at the surface along the  $c$ -direction of the  $\text{LiCoO}_2$  nanoparticles.

Compared with the bulk  $\text{LiCoO}_2$ , the  $\text{Li}_{1+\delta}\text{Co}^{\text{II}}_{\delta}\text{Co}^{\text{III}}_{1-\delta}\text{O}_2$  layer at the surface shows variations in its charge–discharge properties and electronic structure. Such a unique surface state includes electronic spin state transitions<sup>54</sup> and surface reactivity to an electrolyte.<sup>55–57</sup> Many investigations on the SEI of graphite anodes<sup>58–60</sup> and the cathode–electrolyte interface (CEI)<sup>61–64</sup> have provided a picture of the surface film, where solvent decomposition forms organic products and salt decomposition forms inorganic products. These *ex situ* studies are useful to consider the interfacial phenomena but have not been used to observe the real interface under battery-operating conditions where potential bending between the electrode and electrolyte occurs. Hence, to clarify the interfacial phenomena, it is essential to directly investigate the interface by *operando* measurements.

As a technique for *operando* observation of the electrode–electrolyte interface, total reflection fluorescence XAS is a powerful tool. The total reflection fluorescence XAS method is a technique for detecting fluorescence x rays emitted from a sample surface when the incident x rays totally reflect on the sample surface.<sup>65</sup> In the Co K-edge XANES energy range for the measurement of  $\text{LiCoO}_2$ , the detection depth is approximately 2–5 nm in the vicinity of the total reflection critical angle. When comparing the Co K-edge XANES spectra of the bulk (standard thin-film incident measurement) and surface (measured at an angle below the critical angle of total reflection) of  $\text{LiCoO}_2$  thin films in contact with an electrolyte using an *operando* cell [Figs. 6(a) and 6(b)], the surface spectrum reflecting the information near the electrode–electrolyte interface is greatly changed, even though the spectrum of the bulk is hardly changed by contact with the electrolyte solution.<sup>66</sup>

By contacting the electrolyte, Co ions in  $\text{LiCoO}_2$  near the interface are reduced. The electronic structure of Co obtained from the XANES spectrum of the surface  $\text{LiCoO}_2$  is irreversibly changed, unlike the spectrum of the bulk at charge potentials of 3.2, 3.8, 4.0, and 4.2 V

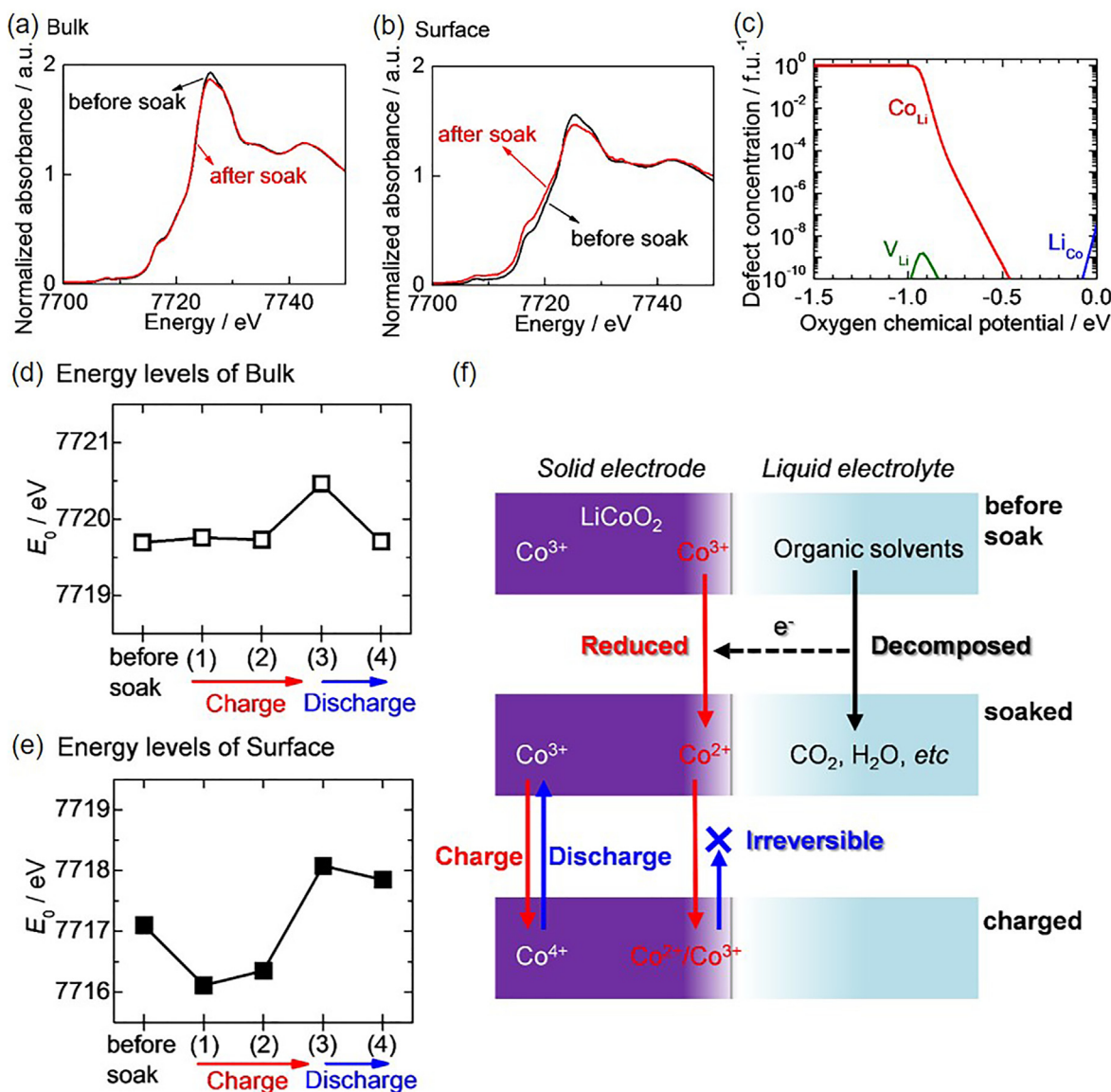


**FIG. 6.** Co K-edge XANES spectra of (a) bulk  $\text{LiCoO}_2$  and (b) surface  $\text{LiCoO}_2$  before and after electrolyte soaking. (c) Defect formation in  $\text{LiCoO}_2$  as a function of oxygen chemical potential calculated by density functional theory (DFT). [(d) and (e)] Absorption edge energy of the Co K-edge XANES spectra of the  $\text{LiCoO}_2$  film measured (1): after soaking, (2): at 3.8 V, (3) at 4.2 V, and (4) after discharging to 3.8 V. (f) Schematic illustration of the proposed initial degradation reaction at the electrode–electrolyte interface. Reprinted with permission from Takamatsu *et al.*, *Angew. Chem. Int. Ed.* **51** 11597–11601 (2012). Copyright 2012 Wiley-VCH.<sup>66</sup>

and discharge potentials of 4.0 and 3.8 V [Figs. 6(d) and 6(e)]. This indicates that the irreversible behavior proceeds from the vicinity of the electrode–electrolyte interface, even though the bulk  $\text{LiCoO}_2$  shows fully reversible charge–discharge. As shown in Fig. 6(f), the initial degradation caused by contacting the electrolyte increases during charge and discharge and expands from the interface to the bulk. This phenomenon is an example of a direct indication that a stable electrode–electrolyte interface is an important factor for the cycling life of lithium-ion batteries.<sup>66</sup>

The observed phenomena at electrode–electrolyte interfaces are supported using theoretical studies.<sup>67</sup> When the defect structures in the

oxidation and reduction states of  $\text{LiCoO}_2$  are calculated by first-principles calculations, in the reduction state, divalent CoO more likely forms due to the introduction of Li defects at Li sites [Fig. 6(c)].<sup>66</sup> Because the cathode in contact with the electrolyte is closer to the reduced state, a reduced CoO-like structure is formed at the interface. Thermodynamically, this reduced phase should diffuse into the bulk. However, in actual lithium-ion battery operation,  $\text{LiCoO}_2$  demonstrates long-term stability because the above-mentioned reduction reaction is kinetically slow when operating at approximately room temperature.

Synchrotron x-ray reflectometry (XRR) and XRD also provide knowledge of the reaction at the electrode–electrolyte interface of

lithium-ion battery systems. *Operando* XRR using an epitaxial film of  $\text{LiCoO}_2$  indicates that a CEI layer forms on the surface of  $\text{LiCoO}_2$  after soaking in an electrolyte and that the surface roughness of the intercalation (110) plane increases with an applied voltage, while no significant changes in surface morphology are observed for the nonactive (003) intercalation plane during the pristine stage of the

charge–discharge process.<sup>68–70</sup> Such surface phenomena and crystal plane dependency are also detected in  $\text{LiMn}_2\text{O}_4$  epitaxial thin films, as shown in Fig. 7(a).<sup>71</sup> Neutron reflectometry can also be applied, which shows that the surface of  $\text{LiFePO}_4$  is stable during the first charge–discharge process.<sup>72</sup> *Operando* XRR and NR have been applied to investigate the structure of an electrical double layer in an ionic

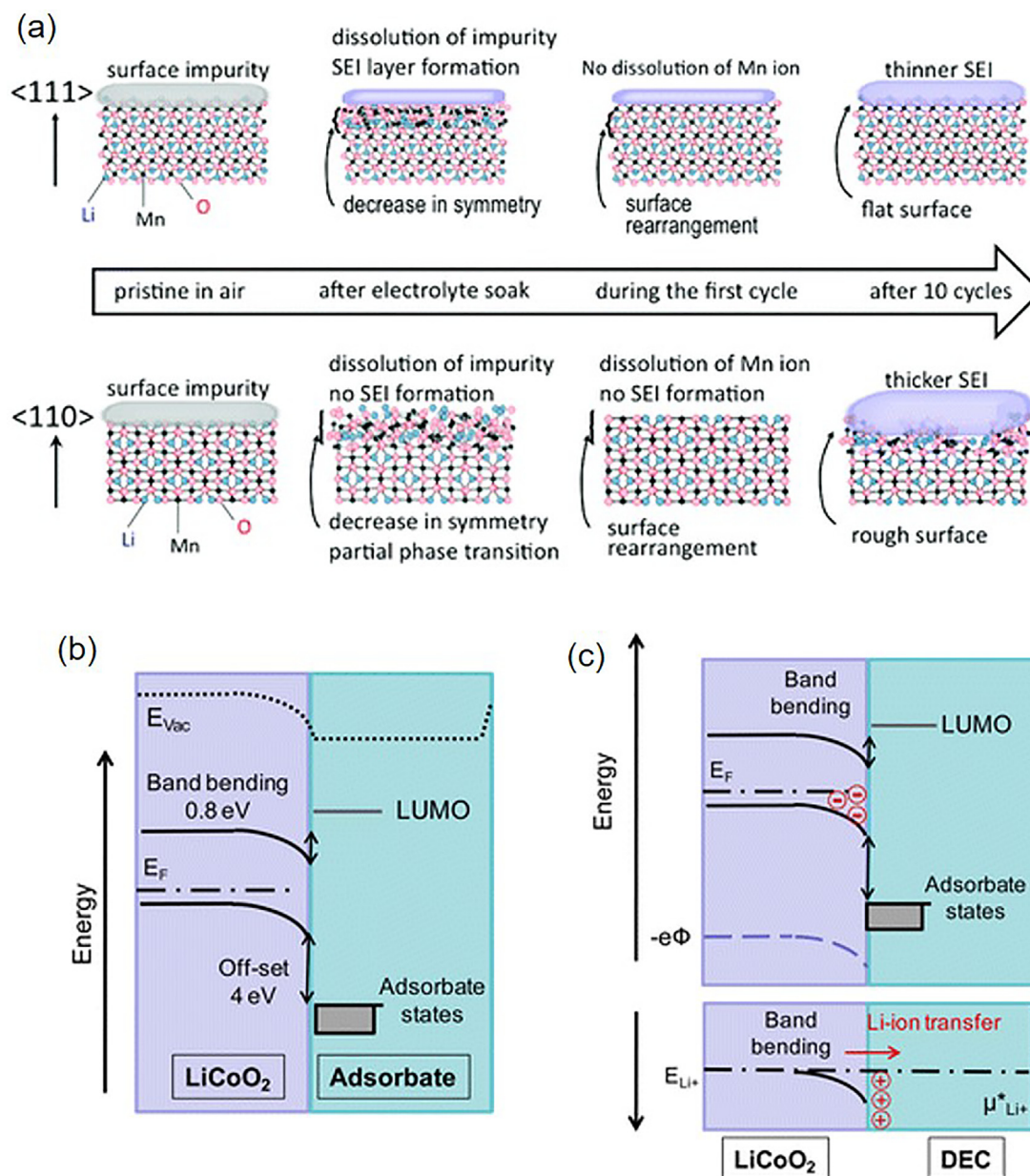


**FIG. 7.** Proposed interphase behavior between cathode and electrolyte. (a) Schematic illustration of surface change for the (111) and (110) crystal planes of  $\text{LiMn}_2\text{O}_4$  observed in *in situ* XRD and XRR measurements and *ex situ* TEM observations. Surface films are formed on  $\text{LiMn}_2\text{O}_4$  by immersion in electrolyte, and the reconstruction of  $\text{LiMn}_2\text{O}_4$  surface proceeds in the first charge–discharge reaction. These situations differ depending on the crystal plane. Reprinted with permission from Hirayama *et al.*, J. Am. Chem. Soc. **132**, 15268–15276 (2010). Copyright 2010 American Chemical Society.<sup>71</sup> Schematic illustration of (b) electron energy level and (c) Li ion energy level of the  $\text{LiCoO}_2$ –DEC interface after exposure. At the interface where  $\text{LiCoO}_2$  and electrolyte come into contact, band bending of  $\text{LiCoO}_2$  occurs, which may have an effect on the interfacial reaction. Reprinted with permission from Becker *et al.*, J. Phys. Chem. C **118**, 962–967 (2014). Copyright 2014 American Chemical Society.<sup>80</sup>

liquid system.<sup>73–77</sup> *Operando* surface x-ray diffraction (*in situ* SXRD) reveals that structural changes on the surface of  $\text{LiNi}_{0.8}\text{CoO}_2$  epitaxial films are different from those in the bulk.<sup>78</sup> Contact with the electrolyte causes abrupt deformation of the surface crystal lattice, followed by restructuring upon applying a cell voltage.<sup>71,78</sup>

The origin of interfacial phenomena is band bending, which has been mostly analyzed by x-ray photoelectron spectroscopy.<sup>79</sup> In the interfacial structure between a  $\text{LiCoO}_2$  thin film and diethyl carbonate (DEC),<sup>80</sup>  $\text{LiCoO}_2$  behaves like a semiconducting electrode and exhibits band bending. The band bending is attributed to the transfer of lithium ions from the electrode to the adsorbed phase, which is driven by the difference between the lithium-ion chemical potentials of the electrode and adsorbed layer [Figs. 7(b) and 7(c)]. The valence band of  $\text{LiCoO}_2$  shifts to a higher binding energy after electrolyte contact, and the shift is associated with the formation of a CEI layer on the surface of  $\text{LiCoO}_2$ .<sup>81</sup>

Regarding the electrolyte side, sum frequency generation vibrational spectroscopy reveals two adsorption modes of propylene carbonate molecules with oppositely oriented geometries on the  $\text{LiCoO}_2$  surface.<sup>82</sup> Ethylene carbonate (EC) molecules are preferentially adsorbed on the  $\text{LiCoO}_2$  surface compared to linear carbonates, such as diethyl carbonate (DEC) and dimethyl carbonate (DMC). Moreover, the molecular density of the adsorbed EC on  $\text{LiCoO}_2$  is almost 20 times higher than that of DMC in 0.5 M  $\text{LiClO}_4/\text{EC}:\text{DEC}$  (1:1 v/v%), which is far from that in the bulk solution.<sup>83</sup>

The above-mentioned surface phenomena are one of the factors causing degradation in cathodes. To improve the cycling life, the effects of a surface coating and electrolyte additives have been widely reported.<sup>84–86</sup> The oxide coating prevents direct contact between the active material of a cathode and an electrolyte solution, thereby suppressing the dissolution of  $\text{Co}^{4+}$  from a  $\text{Li}_x\text{CoO}_2$  cathode into an electrolyte solution.<sup>87</sup> The coating stabilizes the defective crystal structure by inserting the solid solution of  $\text{Mg}^{2+}$  in  $\text{MgO}$  into the  $\text{Li}_2\text{O}$  layer of  $\text{LiCoO}_2$ .<sup>88</sup> According to the *operando* total reflection fluorescence XANES analysis of the model interface with a  $\text{MgO}$  surface coating on a  $\text{LiCoO}_2$  thin film electrode, the interfacial layer formed by contact with the electrolyte solution observed with bare  $\text{LiCoO}_2$  does not form at the interface of  $\text{MgO}$ -coated  $\text{LiCoO}_2$ .<sup>89,90</sup> To observe the local structure change at the  $\text{LiCoO}_2$  surface, depth-resolved XAS was carried out, showing that the formation of a solid–solution layer stabilizes the  $\text{LiCoO}_2$  surface.<sup>89</sup>  $\text{Mg}$  ions diffuse into  $\text{LiCoO}_2$ , and  $\text{Co}$  ions are reduced to balance the charge. When  $\text{Mg}^{2+}$  occupies a Li site,  $\text{Li}_{1-\delta}\text{Mg}_\delta\text{Co(II)}_\delta\text{Co(III)}_{1-\delta}\text{O}_2$  is formed, and  $\text{Co(II)}$  is increased based on the amount of  $\text{Mg}^{2+}$  in the substituted solid solution. This solid–solution phase has lithium-ion conductivity and acts as pillars. The crystal structure of the interface is stable, even after lithium is removed at a high potential, thereby contributing to the improvement in charge–discharge characteristics. It has been confirmed that initial surface reduction is suppressed by the  $\text{ZrO}_2$  coating<sup>91</sup> and vinylene carbonate additive in the same manner.<sup>92</sup> In addition, it has been observed that reduction by immersion in an electrolyte solution does not occur in  $\text{LiFePO}_4$  (Ref. 93) or the high-potential spinel  $\text{LiNi}_{0.5}\text{Mn}_{1.5}\text{O}_4$ .<sup>94</sup> These stabilization mechanisms are shown in Fig. 8. Moreover, regarding the study of aqueous electrolytes, the contribution of the interface is important, and the mechanism described above is utilized to design the stable interface.<sup>95</sup> The analysis of such electrode–electrolyte interfaces has been applied to the solid–solid interfaces of all solid-state batteries,<sup>96</sup> and this research will be accelerated further in the future.

In all-solid-state batteries, the phenomena of the electrode–electrolyte interphase are assumed to be different. Takada *et al.* found that a large resistance existed at the solid-state junction between the electrolyte and electrode.<sup>97,98</sup> They stated that the resistance was attributed to the presence of space-charge layers at the solid-state junction interface. For example, when the interface between  $\text{LiCoO}_2$  cathode and sulfide solid electrolyte is prepared, a heterointerface in which a large space charge layer is formed on the electrolyte side. When solid-state interfaces with different chemical potentials for lithium ions are formed, the lithium ions will migrate to the lower  $\text{LiCoO}_2$  of their potentials. At this time, a large space-charge layer region is formed on the electrolyte side, causing a concentration gradient of lithium ions. On the electrolyte side, the material composition changes from a decrease in lithium concentration, resulting in a deviation from an optimum composition that gives a maximum ionic conductivity. The electrode/electrolyte interface as a large interfacial resistance component is a factor that prevents charge transfer reaction. When an oxide is introduced as a buffer layer, a space-charge layer is formed between solid electrolytes having no electron conduction, but the solid electrolyte does not develop enough to be deficient in lithium ions. In other words, it acts as a buffer layer against the formation of the space-charge layer developed by adding this oxide solid electrolyte layer, so that  $\text{LiCoO}_2$  and the sulfide solid electrolyte can be connected without a high-resistance component. Based on this concept, active materials coated by  $\text{LiNbO}_3$  are widely used in all-solid-state batteries using sulfide solid electrolytes.<sup>99,100</sup> While the high resistance at the interface is interpreted as the above effect without formation of decomposed product, the first-principles calculation shows that the narrow potential window of the solid electrolyte leads to the formation of a high-resistance layer at the interface of the solid electrode/solid electrolyte.<sup>101,102</sup> Sakuda *et al.* observed the reactant layers formed at the interface of  $\text{LiCoO}_2/\text{Li}_2\text{S}-\text{P}_2\text{S}_5$  after charging.<sup>103</sup> In addition, the introduction of  $\text{Li}_2\text{SiO}_3$  and  $\text{Li}_3\text{PO}_4$  buffer layers suppresses the formation of interface formation layers and reduces the interfacial resistance.<sup>103,104</sup>

#### IV. CRYSTAL AND ELECTRONIC STRUCTURE CHANGES OF ELECTRODE ACTIVE MATERIALS

The reaction at the electrode–electrolyte interface is followed by lithium-ion insertion and de-insertion from electrode active materials. Under the operating conditions of lithium-ion batteries, the crystal structure change of electrode active materials proceeds due to continuous ion diffusion; in particular, at high-rate charge and discharge, there is a possibility that the phase change behavior is greatly different from the crystal structure in the equilibrium state. Conventionally, the analysis of the crystal and electronic structure of active materials has been performed in the equilibrium state, but information on structural changes in the nonequilibrium state has not been obtained. This section introduces the crystal structure change in the nonequilibrium state of electrode active materials and the origin of the fast charge–discharge reaction.

One of the representative active materials is  $\text{LiFePO}_4$ ,<sup>105</sup> which exhibits high-rate capability and high safety.<sup>106–109</sup>  $\text{LiFePO}_4$  is separated into a Li-rich phase (LFP phase) and Li-poor phase (FP phase) in the charge–discharge reaction,<sup>110</sup> and the total Li content changes by changing only the ratio of the two phases. Various models have been proposed for the phase transition mechanism of the LFP

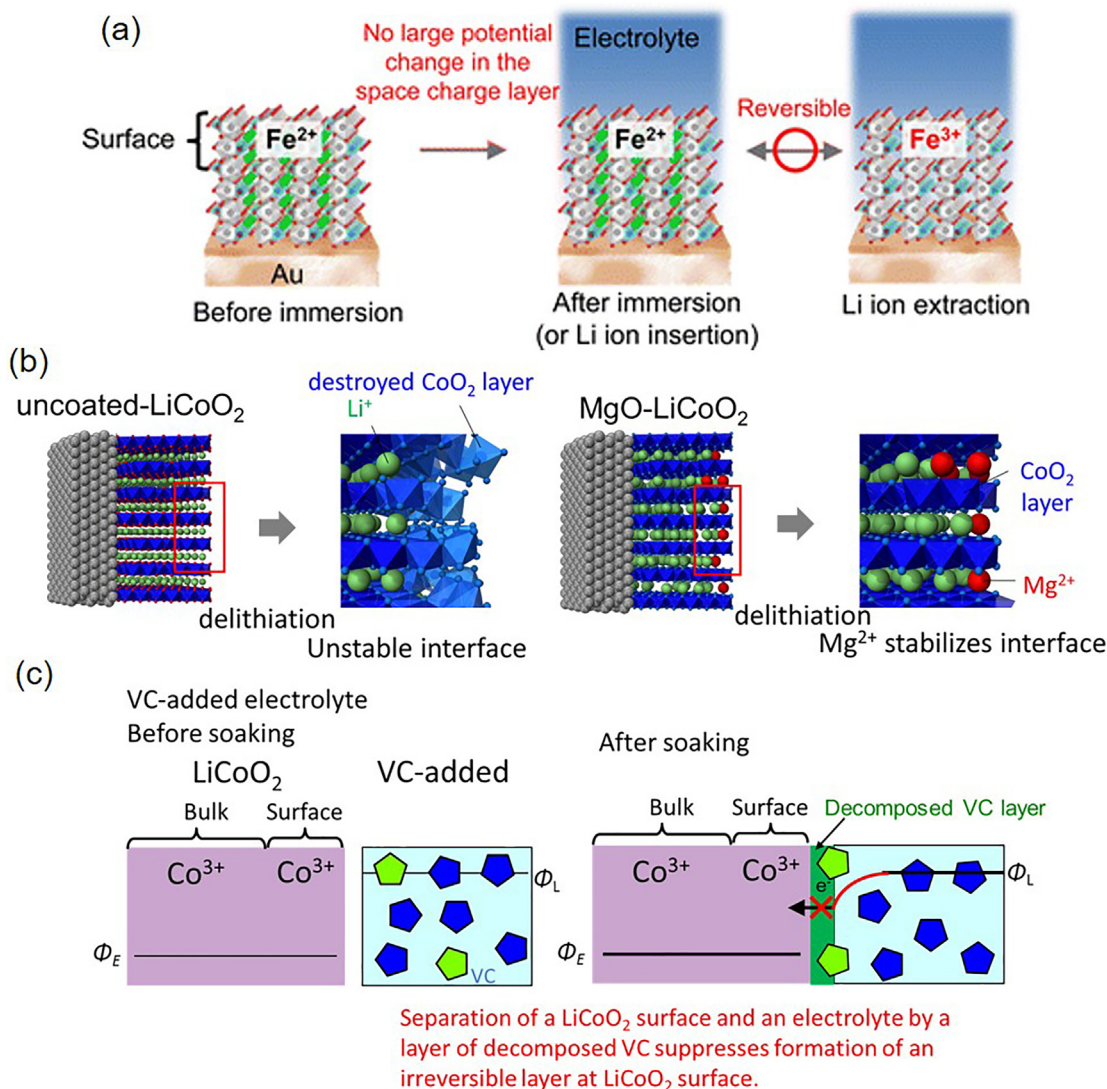


**FIG. 8.** Mechanism of improving interphase stability using active materials, surface coating, and additive. (a) Schematic illustration of the surface structure of  $\text{LiFePO}_4$  during lithium-ion extraction. Due to the high stability of  $\text{LiFePO}_4$ , no space charge layer is formed and reversible lithium-ion insertion/deinsertion proceeds. Reprinted with permission from Yamamoto *et al.*, *J. Phys. Chem. C* **118**, 9538–9543 (2014). Copyright 2014 American Chemical Society.<sup>93</sup> (b) Schematic illustration of the surface structure of uncoated  $\text{LiCoO}_2$  and  $\text{MgO-LiCoO}_2$  during lithium-ion extraction. In the case of  $\text{LiCoO}_2$  without surface coating, lithium extraction destabilizes the surface, leading to structural degradation, while  $\text{MgO}$  coating stabilizes the surface with  $\text{Mg}$  ions acting as pillars. Reprinted with permission from Oriksa *et al.*, *Adv. Mater. Interfaces* **1**, 1400195 (2014). Copyright 2014 Wiley-VCH.<sup>89</sup> (c) Schematic illustration of the electronic structure change by electrolyte additive at the  $\text{LiCoO}_2$ -electrolyte interface.  $\phi$  shows the electrochemical potentials of electron in the electrode and electrolyte. The green pentagons represent vinylen carbonate (VC) additive. The additives present in the electrolyte decompose on the  $\text{LiCoO}_2$  surface to form a film layer. This film avoids direct contact between  $\text{LiCoO}_2$  and the electrolyte and reduces the drastically potential change that occurs on the  $\text{LiCoO}_2$  surface. Reprinted with permission from Takamatsu *et al.*, *J. Phys. Chem. C* **119**, 9791–9797 (2015). Copyright 2015 American Chemical Society.<sup>92</sup> These suppress the formation of the reduced electronic structure at the electrode/electrolyte interface as shown in (c).

phase/FP phase when the two phases coexist. When  $\text{LiFePO}_4$  was first reported as a cathode, Padhi *et al.* proposed a shrinking core model in which the shell formation occurred on the surface of parent crystals and phase boundaries grew inside the grains while Li insertion proceeded isotropically, as shown in Fig. 9(a).<sup>105</sup> Srinivasan and Newman succeeded in explaining the electrochemical profile based on the shrinking core model.<sup>111</sup> This model was developed by considering

the change in Li diffusivity by coherency stress and charge depth at the matching interface.<sup>112,113</sup>

The shrinking core model was widely supported at the beginning of the report, but one-dimensional  $\text{Li}^+$  diffusion in  $\text{LiFePO}_4$  made the model questionable.<sup>117,118</sup> In addition, when nucleation occurs on the surface of a particle, the boundary area of the two phases becomes large, which increases the strain energy; therefore, the shrinking core

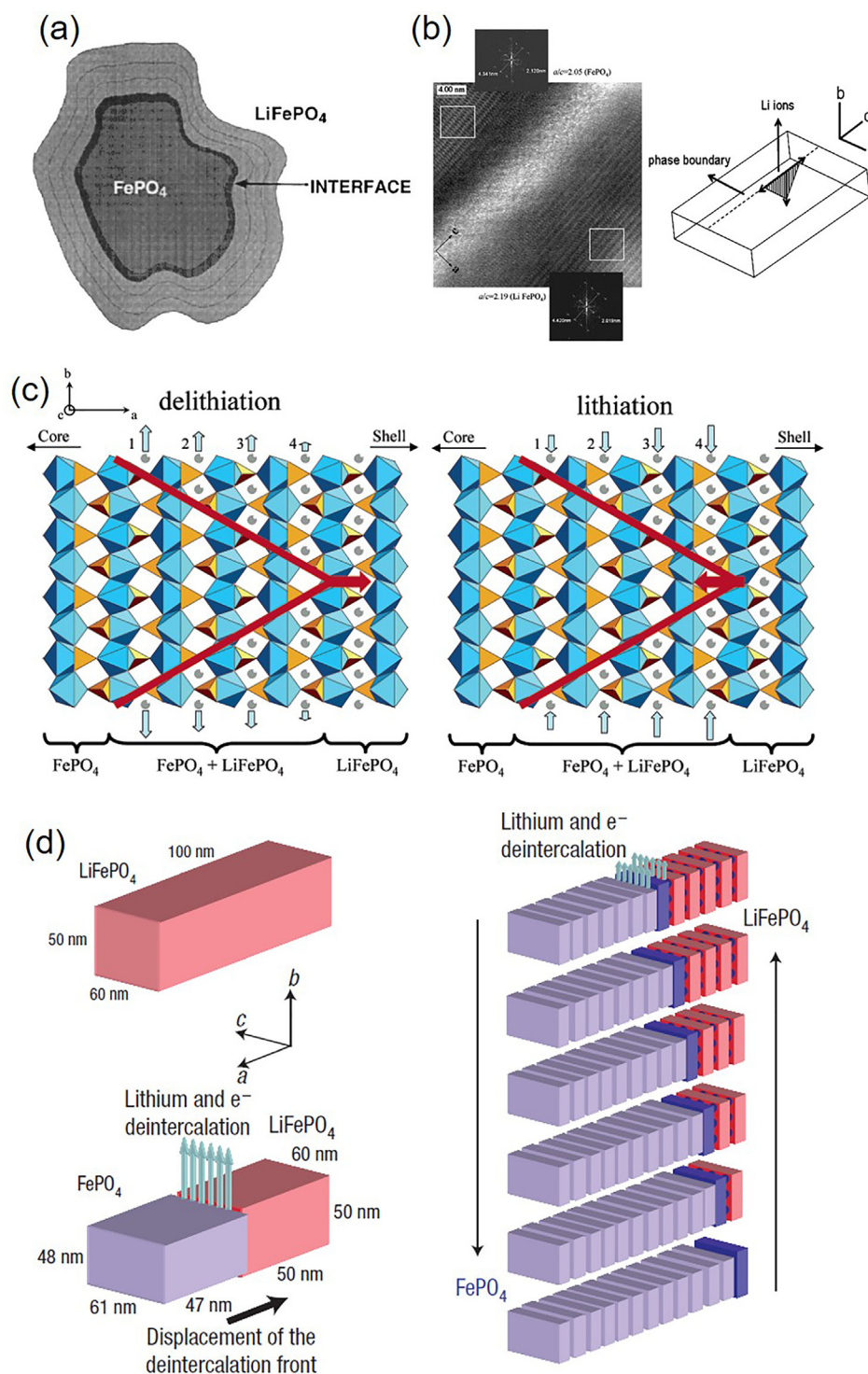


**FIG. 9.** Proposed phase transition mechanism between  $\text{LiFePO}_4$  and  $\text{FePO}_4$ . (a) Schematic image showing the shrinking core model. Reprinted with permission from Padhi *et al.*, *J. Electrochem. Soc.* **144**, 1188–1194 (1997). Copyright 1997 IOP Publishing.<sup>105</sup> (b) Phase boundary aligned along the b-c plane and schematic image of the anisotropic phase transition. Reprinted with permission from Chen *et al.*, *Electrochem. Solid State Lett.* **9**, A295–A298 (2006). Copyright 2006 IOP Publishing.<sup>114</sup> (c) Schematic image of the interfacial region between the  $\text{Li}_{1-x}\text{FePO}_4$  and  $\text{Li}_y\text{FePO}_4$  phases. Reprinted with permission from Laffont *et al.*, *Chem. Mater.* **18**, 5520–5529 (2006). Copyright 2006 American Chemical Society.<sup>115</sup> (d) Schematic image of the "domino-cascade" model. Reprinted with permission from Delmas *et al.*, *Nat. Mater.* **7**, 665–671 (2008). Copyright 2008 Springer Nature.<sup>116</sup>

model is currently unaccepted. Thus, anisotropic reaction models, which turn away from the shrinking core model, have been proposed. Chen *et al.* obtained TEM images of  $\text{LiFePO}_4$  with chemical delithiation from the b-axis and found that the LFP and FP phases in the same crystallite were separated by the b-c plane.<sup>114</sup> Although the phase boundary region was disordered without any crystallinity, it was not completely amorphized, and it was assumed that the two phases coexisted while having a composition gradient. Chen proposed a new anisotropic model in which the phase boundary moved along the a-axis, while Li diffused along the b-axis from the phase boundary of the two phases, as shown in Fig. 9(b). Laffont *et al.* measured  $\text{Li}_x\text{FePO}_4$  with a particle size of approximately 150 nm by electron energy-loss spectrometry (EELS), and the FP phase tended to form at the center of the grain, while the LFP phase tended to form at the edge of the grain.<sup>115</sup> Since the volume decreases and becomes unstable due to the stress received from the grain boundary when the FP phase, with a smaller unit cell volume, grows at the grain end, it is considered that the stress caused by the volume shrinkage in nucleus growth can be alleviated when the FP phase grows inside.<sup>119</sup> These results suggest that the phase boundaries of the two phases are not solid solutions but are clearly phase separated and that the phase boundaries anisotropically migrate in the presence of the FP phase at the center, as shown in Fig. 9(c). Delmas *et al.* obtained the XRD patterns of partially delithiated  $\text{LiFePO}_4$  with a particle size of approximately 100 nm and found that there was no trend in the change in peak width of the diffraction peaks, indicating no change in the crystallite size.<sup>116</sup> Furthermore, from the TEM observations, a single phase of either the LFP phase or FP phase was observed in the individual grains. These results suggest that the nuclear growth rate is overwhelmingly faster than the nucleation rate. Thus, the phase boundary rapidly moves, and the whole crystal undergoes a phase transition once nucleation occurs, which is called the domino-cascade model, as shown in Fig. 9(d).

Although phase boundary models have attracted attention as promising reaction models, other models continue to be proposed. Meethong *et al.* performed *ex situ* XRD and analyzed the Rietveld results of  $\text{LiFePO}_4$  with particle sizes of 113 and 32 nm.<sup>120</sup> The two phases almost ideally coexist in  $\text{LiFePO}_4$  with a relatively large 113 nm grain size. On the other hand, 32 nm- $\text{LiFePO}_4$  with a relatively small grain size shows that the two-phase morphological fraction deviates from the ideal line. This deviation is hypothesized to occur due to the formation of an amorphous phase, that is, not detected by XRD, in addition to the LFP and FP phases. The distortion energy increases because the ratio of the phase boundary increases, thereby increasing the possibility that an amorphous phase forms to suppress the increase in strain energy.<sup>121</sup>

The first-principles calculation proposes that the strain energy of phase separation is large, which suppresses nucleation of the new phase.<sup>122</sup> The energies for 245 combinations of Li/vacancies and electrons/holes show that  $\text{Li}^+$  becomes energetically stable when aligned in the a-c plane in each composition [Fig. 10(a)]. This is because the distance between Li sites is the shortest in the b-axis direction. If the intercalation and extraction of  $\text{Li}^+$  proceeds in such a manner, the phase transition does not occur, and the charge-discharge process can proceed as a single-phase reaction.

On the other hand, the calculation using a phase-field model shows that nucleation-growth-type decomposition or spinodal decomposition occurs when the current density is small in large grains, while

a solid-solution reaction occurs in whole grains when the current density is larger than a certain value in nanoparticles [Fig. 10(b)].<sup>123</sup> Linear stability analysis results in a pseudo-solid-solution reaction above the dashed line in the figure, namely, in the region of high current density, and phase separation in the region of low current density, which is below the dashed line. In the real reaction, the pseudo-solid-solution reaction region is supposed to spread from the kinetic problem. Therefore, the pseudo-solid-solution reaction takes place in the water-colored region above the dotted line based on the mathematical simulation, while phase separation takes place only when the current density is small.

Some reports show that the spinodal decomposition occurs rather than the nucleation-growth and phase separation because nucleation becomes difficult due to a large interfacial energy barrier.<sup>124–126</sup> Phase field simulation is applied assuming that the  $\text{Li}^+$  diffusion rate in  $\text{LiFePO}_4$  is not too slow,<sup>117</sup> which proposes that nucleation-growth and phase separation proceed if the two-phase distortions are not considered, but the spinodal decomposition occurs without nucleation considering the distortion. The possibility of nucleation remains due to the relaxation of the strain energy at the surface, but the nucleation-growth-type phase separation and spinodal decomposition also proceed in parallel. The proposed models provide added knowledge of the phase transition mechanism of the LFP/FP phases in two-phase reactions. However, the LFP-FP phase transition behavior of a Li-ion battery during the charge-discharge reaction is unclear. The reason for this is that most of the models cited thus far infer a nonequilibrium state from the measurement of the equilibrium state or from theoretical calculations. It is also important to know how the phase changes in the actual charge-discharge reaction to guide the design of electrode materials.

As already described in Fig. 3, the value calculated from the XANES results (plotted) and the value from the amount of current (dotted line) show good agreement during the charge reaction of LFP. Due to the corresponding current value and charge transfer, the charge transfer and oxidation of Fe occur instantly when lithium is removed. *In situ* XANES of  $\text{LiFePO}_4$  during chemical delithiation also indicates the quick response for electronic structure change.<sup>22</sup> On the other hand, the change in the crystalline phase does not correspond to the charge transfer amount. Figure 11 shows the *operando* XRD patterns obtained during 1C charging of LFP for various particle sizes and voltage profiles.<sup>16</sup> The peak at approximately  $19.15^\circ$  corresponds to the (211) and (020) planes of the LFP phase, the peak at approximately  $19.5^\circ$  corresponds to the (211) plane of the FP phase, and the peak at approximately  $19.85^\circ$  corresponds to the (020) plane of the FP phase. As the charge reaction proceeds, the peak of the LFP phase decreases, and the peak of the FP phase increases; thus, the two-phase reaction proceeds. However, a shift in the peak is observed, especially at 60 nm for the LFP phase, as shown in Fig. 11(a). This indicates that the lattice constant of the two phases, that is, the Li content, changes. The lattice constants and the width at half maximum are discussed on the basis of the change in peak position and peak width calculated from this measurement result.

The lattice constant change during the 1C charging reaction is shown in Fig. 12(a).<sup>16</sup> In this experiment, to eliminate the effect of the solid-solution phase, pretreatment is performed for charging just before the voltage plateau. In the LFP phase, a change in the lattice constant is seen at 60 nm for LFP. On the other hand, no lattice

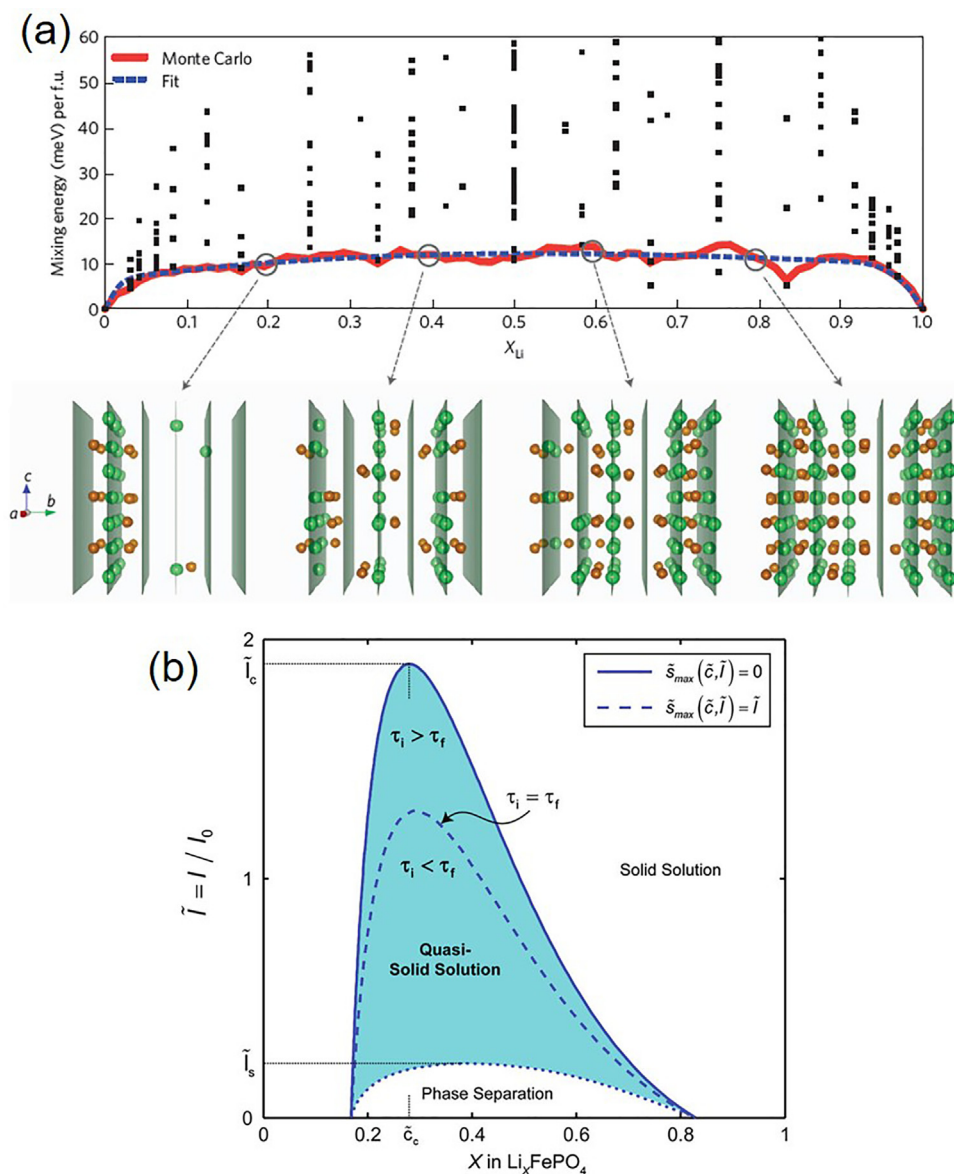


FIG. 10. (a) Mixing energy and corresponding atomic configurations of the single-phase  $\text{Li}_x\text{FePO}_4$ .  $\text{Li}^+$  and  $\text{Fe}^{2+}$  ions are shown in green and brown, respectively. Reprinted with permission from Malik *et al.*, *Nat. Mater.* **10**, 587–590 (2011). Copyright 2011 Springer Nature.<sup>122</sup> (b) Dependence of the two-phase reaction region on the applied current. Reprinted with permission from Bai *et al.*, *Nano Lett.* **11**, 4890–4896 (2011). Copyright 2011 American Chemical Society.<sup>123</sup>

constant change is observed at 150 and 1000 nm, confirming the difference according to the particle size. In contrast, the diffraction peak of the FP phase first appears at a composition of approximately  $x=0.9$ , which is larger than the lattice constant in the equilibrium state, and then, the decrease in the lattice constant value is observed as the reaction proceeds. In particular, the lattice constant change in the initial stage of FP-phase formation is large. A large decrease in this lattice constant is found to have the same tendency for all particle sizes.

As shown in Fig. 12(b), the half-width changes of LFP during the 1C-charging reaction tend to increase greatly, especially at 60 nm. In the FP phase, a decrease in the half width is seen in all samples. The tendency of these changes agrees with the lattice constant, gradually relaxing to the value of the equilibrium state as the half width

decreases. The change in the lattice constant is considered to reflect the change in the amount of Li in the two phases. The change in the half width also involves the distortion of the crystals, but the change in crystal size is mainly reflected.

The lattice parameter changes at the initial stage of new-phase formation; that is, the Li content change can be explained from the Gibbs energy diagram of the two-phase system shown in Fig. 12(c). In the reaction of the  $\text{LiFePO}_4/\text{FePO}_4$  system, the solid-solution reaction proceeds because the single-phase state is stable in the compositions of  $1-1-\alpha$  and  $\beta$  to 0. In the  $1-\alpha$  to  $\beta$  compositions, the two-phase reaction occurs by phase separation because the two-phase state is stable.<sup>110</sup> In the charge reaction (delithiation process), the phase transition begins at  $x=1-\alpha$  in the equilibrium state, and the



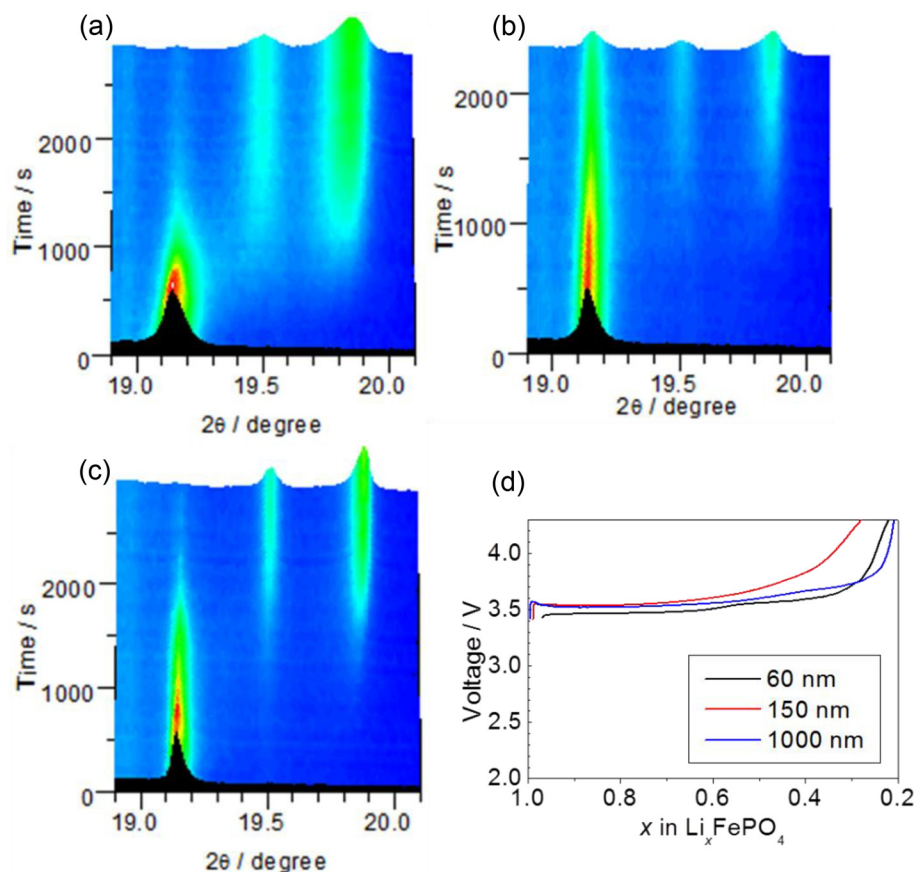


**FIG. 11.** Time-resolved XRD pattern of LFP during 1C charging [particle sizes of (a) 60 nm, (b) 150 nm, and (c) 1000 nm] and (d) charge profile during the time-resolved XRD measurement. Reprinted with permission from Oriksa *et al.*, *Chem. Mater.* **25**, 1032–1039 (2013). Copyright 2013 American Chemical Society.<sup>16</sup>

subsequent reaction proceeds in the two-phase state of the LFP phase with the  $1-\alpha$  composition and the FP phase with the  $\beta$  composition. However, the actual reaction may start the transition of the phase with the  $1-\alpha'$  composition, which is beyond the stable composition because the nucleation of the FP phase does not occur instantaneously but is delayed. In that case, if it is the  $\beta'$  composition, the free energy curve of the LFP phase crosses the tangent of the free energy curve of the LFP phase, and the free energy curve of the FP phase crosses into the  $1-\alpha'$  composition, thereby generating a gain in energy for the FP phase. After the FP phase formation, the composition is considered to lead to a thermodynamically stable  $\beta$  composition. This is also the reason for the largest Li composition change occurring during the formation of the new phase. In the nonequilibrium state, the kinetic compositional deviation occurs, resulting in a delay in reaching a stable composition. This deviation tendency of the Li composition agrees with the experimental results.<sup>16</sup>

The phase behavior during charging from the above results is shown in Fig. 12(d). The results observed in previous *ex situ* measurements are a process in which no biphasic compositional changes are seen, as shown at the top of the figure. On the other hand, in the non-equilibrium state, the phase transition follows a process, as shown at the bottom. First, the FP phase forms in the grains of the LFP phase.

In the initial stage of formation, the FP phase has more Li content than the thermodynamically stable composition. As the charge process progresses, the Li composition approaches the final stable composition. Such a reaction takes place in multiple grains, and the reaction proceeds. When the charge process is stopped in the middle of the reaction, relaxation occurs so that the phase boundary is eliminated because the phase boundary becomes unstable due to the interfacial energy fraction remaining in the single grain. Therefore, *ex situ* determination captures the condition of the phase at that time.

LiFePO<sub>4</sub> exhibits superior high-rate charge–discharge capabilities.<sup>106</sup> If the charge–discharge reaction of LiFePO<sub>4</sub> is a simple two-phase reaction, as originally said, it is unexpected that it has high-rate capabilities over a solid–solution reaction system electrode, despite the need to undergo nucleation, which becomes energetically unfavorable in the phase transition process; this is one of the properties of LiFePO<sub>4</sub> that has not yet been elucidated. Previous modeling<sup>123,127</sup> has reported that LiFePO<sub>4</sub> charging/discharging progresses as a single-phase response when the overvoltage is high. These models indicate that the nucleation of the new phase is difficult due to the large mismatch between the new phase and parent phase at the time of new-phase formation. However, the phase transition behavior is studied only from the calculation, and direct observation by the experiment has not been

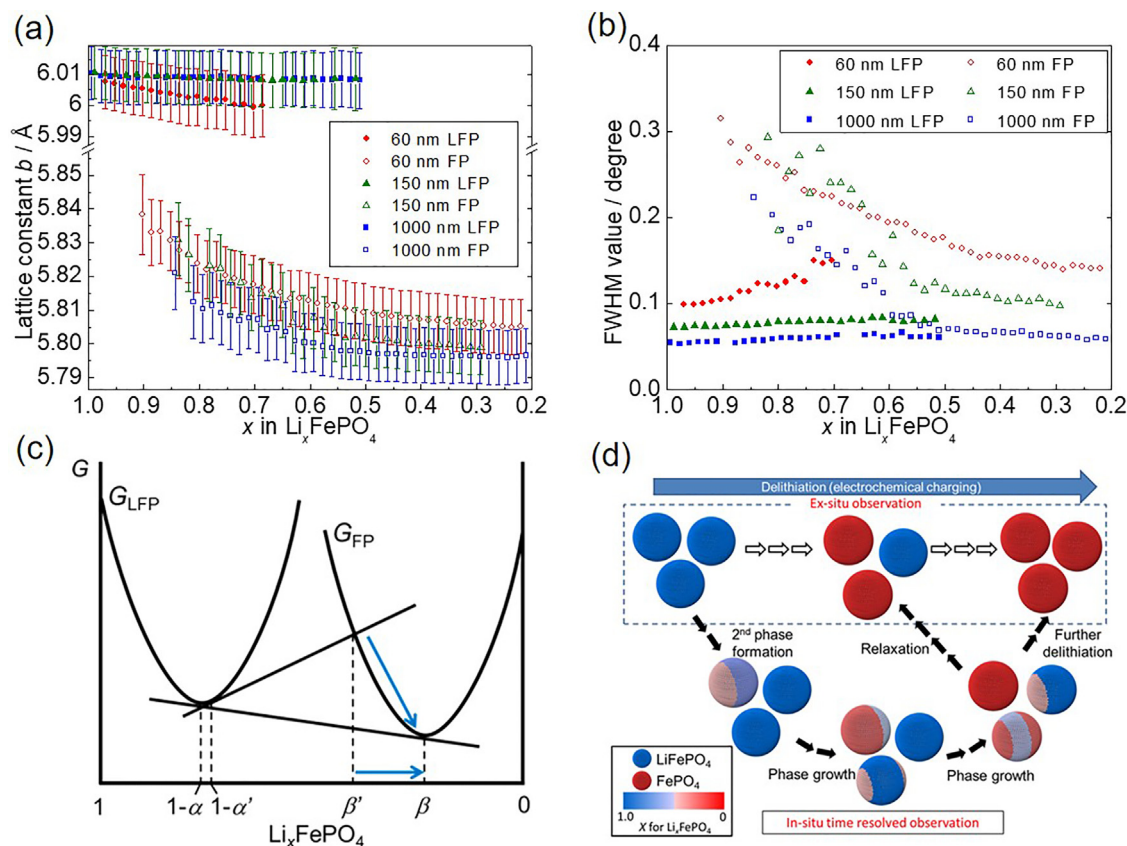


**FIG. 12.** Structural parameter change from *operando* XRD of  $\text{LiFePO}_4$  and phase transition mechanism. (a) Lattice constant change and (b) change in the half-width value calculated from the *operando* XRD patterns shown in Fig. 11. (c) Relation between the Gibbs energy curve and the phase change in  $\text{LiFePO}_4\text{-FePO}_4$ . (d) Phase change model of  $\text{LiFePO}_4$  to  $\text{FePO}_4$ . Reprinted with permission from Orikasa *et al.*, Chem. Mater. **25**, 1032–1039 (2013). Copyright 2013 American Chemical Society.<sup>16</sup>

performed. High-brightness synchrotron radiation x rays have recently been used to enable *operando* XRD during high-speed charging and discharging.

*Operando* XRD patterns during 10C charging–discharging and in the subsequent open-circuit state are shown in Fig. 13(a).<sup>128</sup> The two-phase changes during charging and discharging, as in the 1C case, are confirmed, but in this figure, the two-phase peaks and different new-phase peaks appear between the peaks of the LFP and FP phases as a phenomenon unique to high-rate charging and discharging. These new phase peaks do not appear in the first charge process but appear in the discharge process. As the discharge process progresses, a new phase at approximately  $19.35^\circ$  grows, and the phase remains, even when switching to the charge process. Since the new phase disappears in the relaxation process after the completion of the charge–discharge reaction, the new phase is not a thermodynamically stable phase but a metastable phase (hereinafter referred to as an  $\text{L}_x\text{FP}$  phase) that can be generated kinetically in a nonequilibrium state. It is known that the  $\text{L}_{0.7}\text{CoPO}_4$  phase appears in addition to the  $\text{LiCoPO}_4$  and  $\text{CoPO}_4$  phases in the charging/discharging process of a  $\text{LiCoPO}_4$  system. However, the  $\text{L}_{0.7}\text{CoPO}_4$  phase can even be confirmed in the steady state since it is stable.<sup>129</sup> There have been no previous reports on the

occurrence of a metastable phase in the  $\text{LiFePO}_4$  system. Since this report, many phase change behavior analyses of  $\text{LiFePO}_4$  by time-resolved measurements have been carried out, as shown in Figs. 13(b) and 13(c), and the results have proven electrochemically induced intermediate phase formation during the charging–discharging of  $\text{LiFePO}_4$ .<sup>130–132</sup> The formation of the  $\text{L}_x\text{FP}$  phase is rate-dependent, and the diffraction peaks in  $\text{L}_x\text{FP}$  can be clearly identified as the charge rates increase. The  $\text{L}_x\text{FP}$  peaks are not found in the XRD pattern when relaxed for more than 24 h in the same composition. The above results prove that the  $\text{L}_x\text{FP}$  phase preferentially grows when the charge–discharge rate is fast, and it is a metastable phase that cannot be observed under equilibrium conditions.

The disappearance of the  $\text{L}_x\text{FP}$  phase can be suppressed by decreasing the temperature of the cell, where the lattice constants of  $\text{L}_x\text{FP}$  are found to be  $a = 10.207 \text{ \AA}$ ,  $b = 5.943 \text{ \AA}$ , and  $c = 4.724 \text{ \AA}$ .<sup>133</sup> The  $\text{L}_x\text{FP}$  phase adopts lattice constants that are between those of the LFP and FP phases. The lattice constants of the  $\text{L}_x\text{FP}$  phases are close to those of the solid–solution phase  $\text{Li}_x\text{FePO}_4$  ( $x = 0.6$  to  $0.75$ ), which is reported to be a consequence of high-temperature XRD.<sup>134,135</sup> Therefore, the solid–solution phase  $\text{Li}_x\text{FePO}_4$  ( $x = 0.6$  to  $0.75$ ), which is stable at high temperatures, forms even under

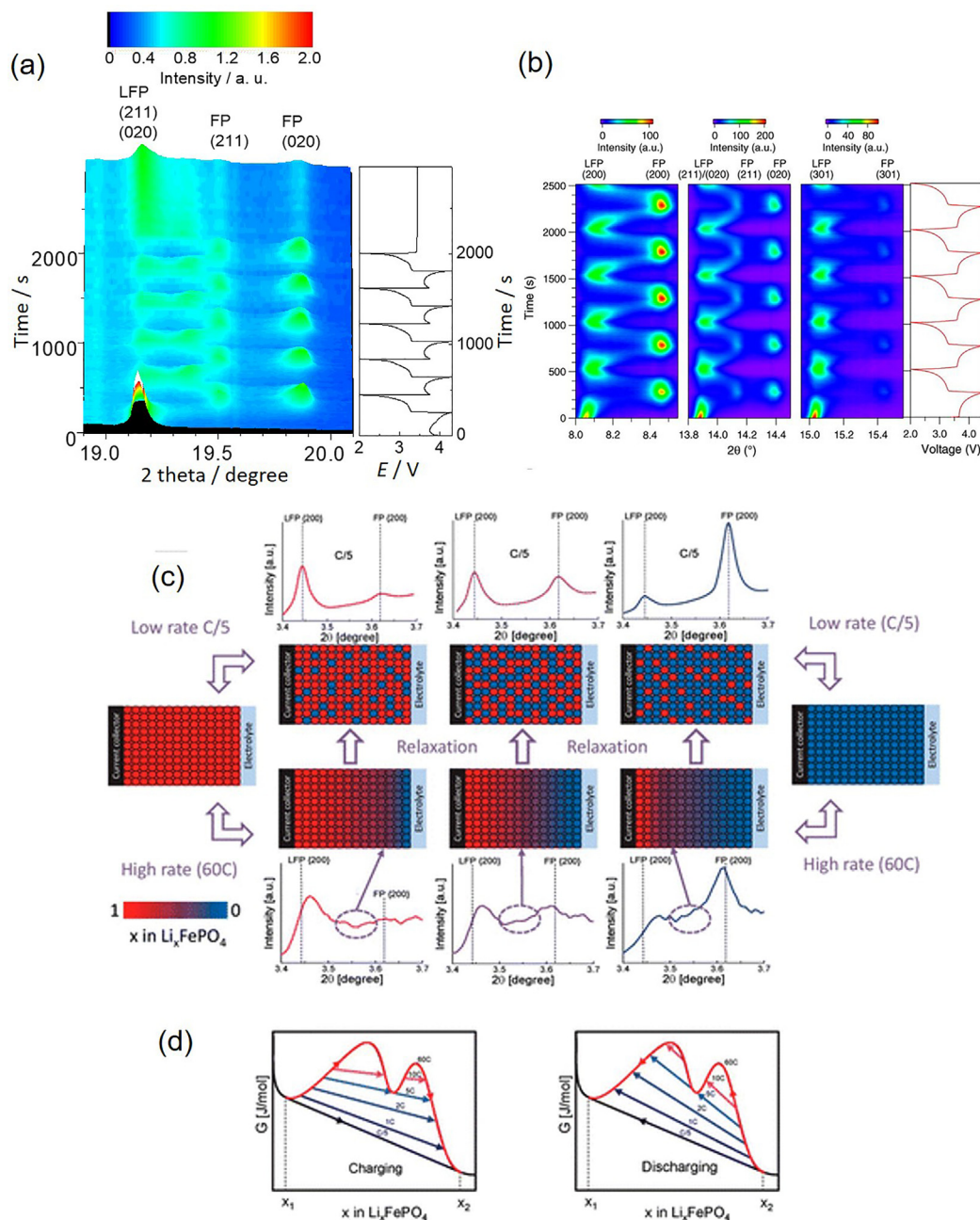


**FIG. 13.** Examples of the observed metastable intermediate phase under phase transition between  $\text{LiFePO}_4$  and  $\text{FePO}_4$ . (a) Detection of the intermediate  $\text{L}_x\text{FP}$  phase by *operando* XRD patterns and charge-discharge curves during charge-discharge cycling at a rate of 10C. Reprinted with permission from Oriasa *et al.*, *J. Am. Chem. Soc.* **135**, 5497–5500 (2013). Copyright 2013 American Chemical Society.<sup>128</sup> (b) Solid solution behavior observed in time-resolved XRD during charge-discharge cycling at a rate of 10C. Reprinted with permission from Liu *et al.*, *Science* **344**, 1252817 (2014). Copyright 2014 The American Association for the Advancement of Science.<sup>130</sup> (c) Model for the phase change behavior in  $\text{LiFePO}_4$  at various rates and upon relaxation. The overpotential at high-rate results in a potential gradient that forms the intermediate phase. Reprinted with permission from Zhang *et al.*, *Nano Lett.* **14**, 2279–2285 (2014). Copyright 2014 American Chemical Society.<sup>132</sup>

nonequilibrium conditions during the electrochemical process at room temperature. A detailed analysis of the  $\text{Li}_{2/3}\text{FePO}_4$  crystal structure was performed by x-ray and neutron diffraction<sup>136</sup> and DFT calculations.<sup>137</sup>

The presence of the  $\text{L}_x\text{FP}$  phase brings significant benefits to the phase transition of  $\text{LFP}/\text{FP}$ . Since the lattice-parameter gap in the two phases of  $\text{LFP}/\text{FP}$  can be as large as 3.6% for the b-axis and 1.8% for the c-axis, the interfacial energy associated with nucleation becomes

large. Therefore, a direct transition from  $\text{FePO}_4$  to  $\text{LiFePO}_4$  does not cause a large current to flow, and the presence of a metastable  $\text{Li}_x\text{FePO}_4$  phase is significant. The lattice mismatch between  $\text{FePO}_4$  and  $\text{Li}_x\text{FePO}_4$  is 2.5% on the b-axis and 0.66% on the c-axis, which is less than that of  $\text{LiFePO}_4$ , making  $\text{Li}_x\text{FePO}_4$  phase kernel generation more likely. In addition, the conductivity of the metastable  $\text{Li}_x\text{FePO}_4$  phase was enhanced by two orders of magnitude.<sup>138</sup>  $\text{LiFePO}_4$ , in which nucleation is rate limiting, shows superior high-rate charge–discharge properties in that the response progresses without delay by nucleation through the intermediate  $\text{Li}_x\text{FePO}_4$  phase.

To detect nonequilibrium behavior in a more particle-by-particle manner, Wagemaker *et al.* dynamically analyzed diffraction spots of  $\text{LiFePO}_4$  during charging–discharging.<sup>139,140</sup> The appearance of a diffuse interface can be confirmed, even at the grain level during high-rate charging–discharging, as shown in Figs. 14(a) and 14(b).<sup>140</sup> Deviations from the equilibrium state upon lithium-ion (de)insertion are detected not only in  $\text{LiFePO}_4$  but also in  $\text{LiNi}_{0.5}\text{Mn}_{1.5}\text{O}_4$  exhibiting a two-phase reaction.<sup>141</sup> The metastable phase, which is assigned to the diffuse interface, dominates in the charge–discharge reaction at high rates. For the layer-structured  $\text{LiNi}_{0.33}\text{Co}_{0.33}\text{Mn}_{0.33}\text{O}_2$ , nonequilibrium behavior in the phase transition from the H1 to H2 phase observed around  $\text{Li}_{0.65}\text{Ni}_{0.33}\text{Co}_{0.33}\text{Mn}_{0.33}\text{O}_2$  was also observed.<sup>142</sup>

The experimental high-rate XRD results of  $\text{LiFePO}_4$  show that the formation of the metastable phase is irreversible.<sup>142</sup> From the phase-field theory of chemical kinetics in  $\text{LiFePO}_4$ , the flux-to-composition relation is asymmetric, and the flux shows a maximum at approximately 0.25.<sup>123</sup> This asymmetry leads to a more heterogeneous compositional change per domain within the particle during Li deinsertion, as shown in Figs. 14(c) and 14(d).<sup>143</sup> Therefore, the distribution of the metastable phase composition inevitably spreads and is broadened in *operando* XRD in which a large amount of particle information is averaged. Alternatively, the irreversible phase change behavior in Li insertion can be explained by the long life of the metastable phase because the region where the flux decreases overlaps the region of the metastable phase at the time of Li insertion. In *operando* XRD conducted at 230 °C where the metastable phase is more stabilized, the lattice-constant change of the metastable phase is observed only at the time of Li deinsertion, as shown in Figs. 14(e) and 14(f).<sup>144</sup> Since  $\text{LiFePO}_4$  exhibits one-dimensional lithium diffusion, the stability of the metastable phase varies with surface diffusion.<sup>96</sup> In a state where Li diffusion on the crystal surface is sufficient, as in the low-rate condition, Li tends to insert into the thermodynamically stable sites, and two-phase separation occurs. However, under high rates, which require sufficiently fast lithium insertion, the formation of metastable phases is accelerated by bulk diffusion of Li into more than one heterogeneous site.

We introduce a case aiming at further high-rate charge–discharge by using the effect of the intermediate phase and  $\text{LiFe}_{0.95}\text{Zr}_{0.05}\text{P}_{0.9}\text{Si}_{0.1}\text{O}_4$  with a small lattice volume difference between the two phases,<sup>145</sup> which has been reported to improve the cycle properties.<sup>146</sup> From the rate capability tests of  $\text{LiFe}_{0.95}\text{Zr}_{0.05}\text{P}_{0.9}\text{Si}_{0.1}\text{O}_4$  and undoped  $\text{LiFePO}_4$ , although both materials exhibit almost the same capacity at the low rate ( $\sim 1\text{C}$ ), a difference is observed at the high rate ( $10\text{C}\sim$ ).  $\text{LiFe}_{0.95}\text{Zr}_{0.05}\text{P}_{0.9}\text{Si}_{0.1}\text{O}_4$  shows a larger charge–discharge capacity at high rate, showing an improved rate capability. In the charge–discharge reaction at 10C, a large difference appears in the behavior of

the intermediate phase ( $\text{L}_x\text{FP}$  phase). In undoped  $\text{LiFePO}_4$ , the  $\text{L}_x\text{FP}$  phase appeared only at the end of discharging and existed in a three-phase state including the two-phase state with the LFP phase and the FP phase. The Li compositions of the metastable intermediate phases of  $\text{LiFe}_{0.95}\text{Zr}_{0.05}\text{P}_{0.9}\text{Si}_{0.1}\text{O}_4$  ranged from  $x = 0.63$  to 0.86, and the large solid solution of the  $\text{L}_x\text{FP}$  phase reduced the strain at the interface of the two phases and enabled fast charging and discharging by realizing a smooth phase transition reaction. The suppression of lattice strain contributes to the stabilization of metastable phases to realize smooth phase transition reactions, which is a key parameter for high-rate capability.

*Operando* XRD is also useful to analyze the complicate phase transition phenomena of graphite anodes. Graphite with lithium ions inserted has a stage structure, but the intermediate states have not been analyzed in detail. *Operando* XRD has shown the existence of superlattice structures such as  $\text{LiC}_{288}$ ,  $\text{LiC}_{144}$ , and  $\text{LiC}_{72}$ .<sup>147</sup> The intermediate state observed at high-rate charge–discharge has also been found in the  $\text{Li}_4\text{Ti}_5\text{O}_{12}$  spinel structure of anode. *Operando* electron energy loss spectroscopy measurements at Li K-edge and first-principles calculations proofed the formation of the intermediate phase and fast lithium-ion conduction at high rates.<sup>148</sup>

## V. REACTION INHOMOGENEITY WITHIN A COMPOSITE ELECTRODE

Although charge–discharge reaction proceeds by a lithium-ion insertion/de-insertion in an electrode active material, in reality, the filling ratio of a composite electrode in which active materials are mixed in three dimensions can be increased to increase the reaction current. A composite electrode is composed of an active material for storing lithium ions, carbon for forming an electron conductive path, and a binder for bonding them. X-ray computed tomography (CT) and scanning electron microscopy (SEM) studies visualize their morphological structure [Figs. 15(a) and 15(b)],<sup>149</sup> which is an extremely complicated structure in which an electrolyte occupies the voids to create an ionic conductive path, as shown in Fig. 15(c).<sup>150</sup>

There are multiple reaction processes during the battery reaction of a composite electrode, and an internal resistance component exists in each. The following are the main internal resistance components.

- ① Electronic resistances
  - (a) Connection resistance between the current collector and lead wire
  - (b) Metal resistance in the current collector
  - (c) Contact resistance between the electrode and current collector
  - (d) Electronic resistance in the composite electrode
- ② Ionic resistances
  - (e) Ionic conduction resistance in the electrolyte
  - (f) Ionic conduction resistance in composite electrodes
  - (g) Charge transfer resistance
  - (h) Ion diffusion in solid active materials

The voltage that can be extracted from a battery is the value obtained by subtracting the activation and diffusion overpotentials and the Ohmic loss from the equilibrium potential. Since the Ohmic loss can be expressed by the internal resistance time current, to extract a large amount of energy from a battery, it is necessary to reduce the

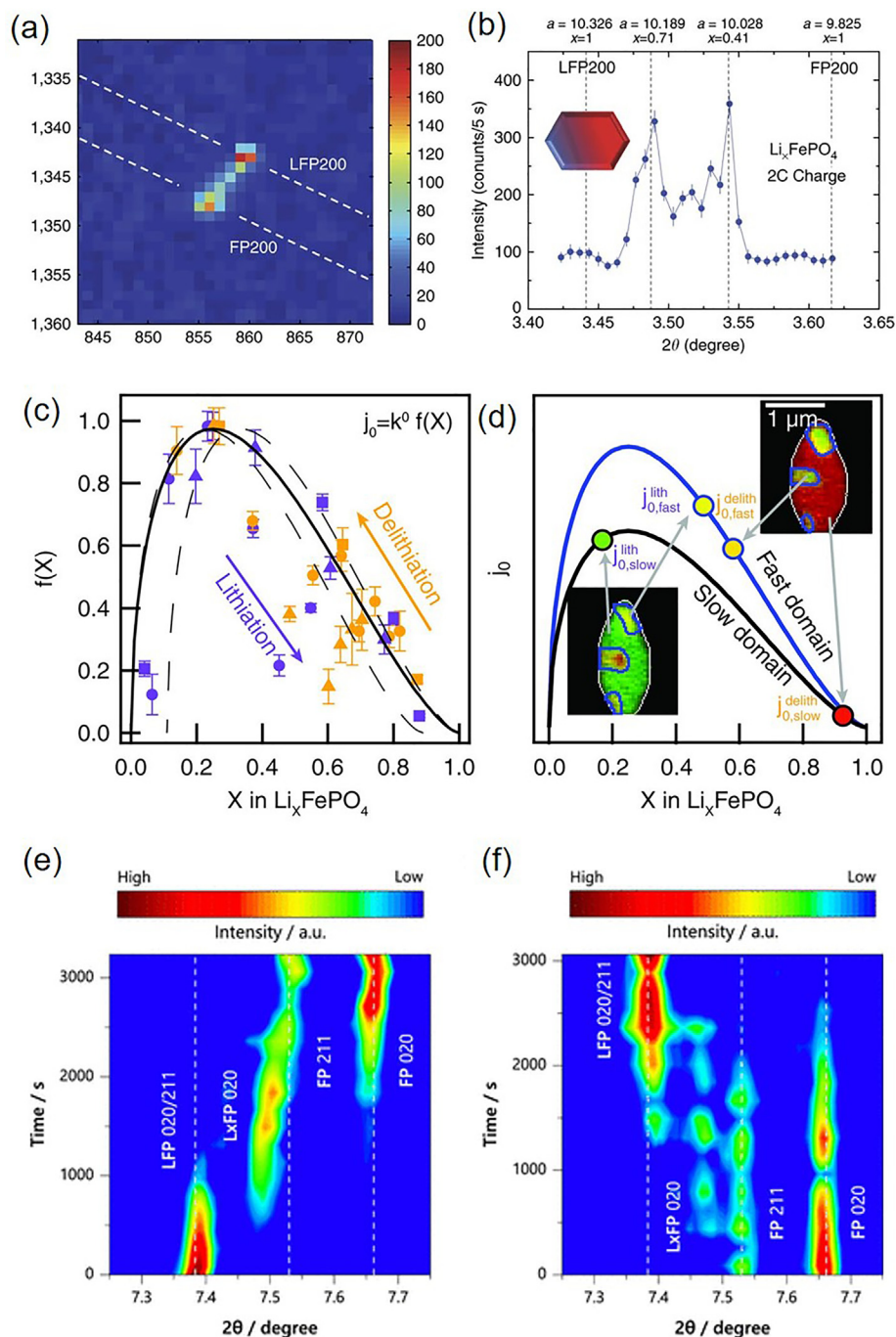


**FIG. 14.** Recently reported phase transition mechanism on  $\text{LiFePO}_4$ . (a) x-ray diffraction spot from (200) reflection during 2C charging showing the coexistence of the LFP and FP phases within a single particle. The dashed lines correspond to the powder diffraction rings for the (200) reflections of the LFP and FP phases. (b) Corresponding intensity from line scan as a function of the scattering angle  $2\theta$ . The maximum intensity is observed corresponding to  $x=0.71$  for the LFP phase and  $x=0.42$  for the FP phase. Reprinted with permission from Zhang *et al.*, Nat. Commun. **6**, 8333 (2015). Copyright 2015 Authors, licensed under a Creative Commons Attribution (CC BY) license.<sup>140</sup> (c) Estimated exchange current density ( $j_0$ ) as a function of  $x$  in  $\text{Li}_x\text{FePO}_4$ , showing asymmetric curve with the Li composition  $x$ . Reprinted with permission from Lim *et al.*, Science **353**, 566–571 (2016). Copyright 2016 The American Association for the Advancement of Science.<sup>143</sup> (d) Schematic illustration of asymmetric behavior on lithiation and delithiation in  $\text{LiFePO}_4$ . Because the maximum  $j_0$  is observed at  $x \approx 0.25$ , the difference between  $j_0$  in the fast and slow domains is small during lithiation. Reprinted with permission from Lim *et al.*, Science **353**, 566–571 (2016). Copyright 2016 The American Association for the Advancement of Science.<sup>143</sup> (e) Operando XRD patterns of  $\text{LiFePO}_4$  during (e) delithiation and (f) lithiation at  $230^\circ\text{C}$ . Reprinted with permission from Yoshinari *et al.*, Chem. Mater. **31**, 7160–7166 (2019). Copyright 2019 American Chemical Society.<sup>144</sup>

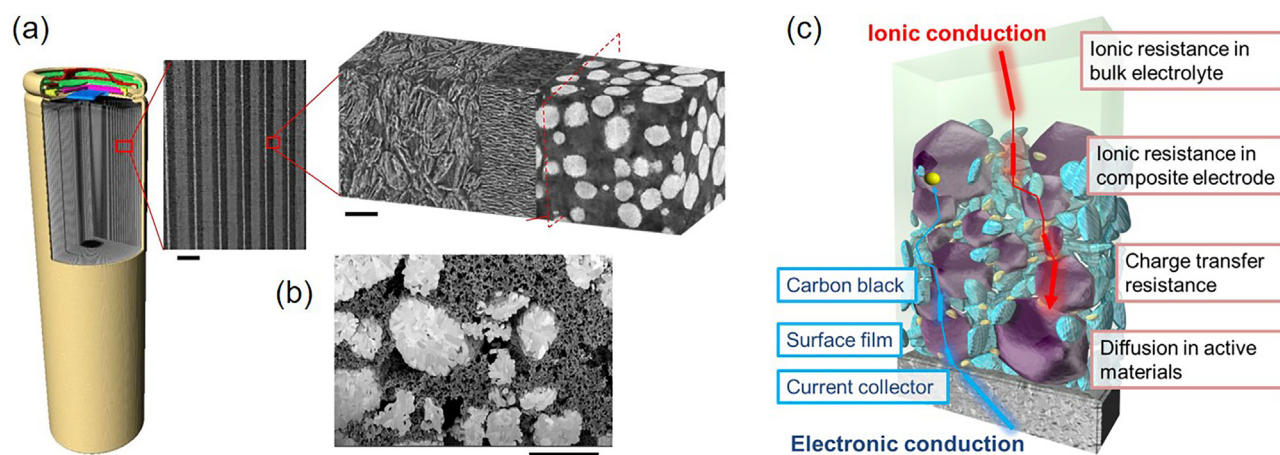


**FIG. 15.** Structure of composite electrodes in lithium-ion batteries. (a) Reconstructed image of cylindrical battery measured by x-ray CT; magnified slice showing the periodic layered structure of the graphite anode, polyolefin separator, and NMC cathode (from left to right). The scale bars represent 10 mm, 240  $\mu\text{m}$ , and 10  $\mu\text{m}$  from left to right. (b) SEM image showing the carbon-binder domain morphology alongside the secondary cathode particles with a scale bar of 10  $\mu\text{m}$ . Reprinted with permission from Lu *et al.*, Nat. Commun. 11, 2079 (2020). Licensed under a Creative Commons Attribution (CC BY) license.<sup>149</sup> (c) Schematic illustration of a composite electrode in lithium-ion batteries. Ionic and electronic currents are supplied from the electrolyte and current collector sides, respectively, which have different types of resistances. Reprinted with permission from Orikasa *et al.*, Sci. Rep. 6, 26382 (2016). Copyright 2016 Authors, licensed under a Creative Commons Attribution (CC BY) license.<sup>150</sup>

internal resistance as much as possible. Since the electronic conductivity of a metal is high and the lead wire and current collector are welded, the resistance components of (a) and (b) are usually not a problem. It is difficult to control (e) and (h) because they are intrinsic values of a substance based on the crystal structure, diffusion paths of ions, valences of cations, etc. Although rigorous design and synthesis of a crystal structure are required, a relatively simple improvement method is to reduce the particle size and shorten the diffusion distance. The charge transfer resistance can be reduced by increasing the electrode surface area by decreasing the particle size. The contact resistance is not negligible because it makes a passive film with an insulating property of approximately 30 nm on the surface of aluminum, which is used as a cathode current collector. In practice, since the electrode is pressed when preparing a composite electrode, defects form in the coating on the aluminum current collector foil by the carbon of the conductive auxiliary agent, which is also conductive; thus, it has not become a large problem in practical use.<sup>151</sup> Thus, electronic resistance in composite electrodes is generally considered not a major problem. To obtain as large a volume energy density as possible, the composite electrode is pressed together at the time of preparation. This is because, at this time, the adhesion of the conductive auxiliary agent and the active material is increased to form a good electron conduction path. Therefore, to fabricate a high-power battery, decreasing the ion conduction resistance in the composite electrode becomes important. Using the tortuosity–porosity correlation by Thorat *et al.*,<sup>152</sup> the effective ionic conductivity of 1 M LiPF<sub>6</sub> in EC:EMC (3:7) in a composite electrode with a void ratio of 50% was calculated to be approximately 1.77 mS cm<sup>-1</sup>, which is 1/5 the bulk conductivity of 9.21 mS cm<sup>-1</sup>. Fongy *et al.* estimated that by evaluating the electrochemical properties using a composite electrode with varying porosity, the ionic and electronic conductivities of the composite electrode change depending on the three-dimensional structure of the composite electrode, which affects the rate capability of the cell.<sup>153,154</sup>

Improving the effective ionic conductivity of a composite electrode in addition to improving the bulk conductivity is required to provide a high-rate capability, which includes increasing the porosity of the electrode, reducing the thickness of the electrode, and controlling the morphology of the composite electrode. It has been empirically recognized that the preparation conditions of a composite electrode greatly affect the charge–discharge characteristics.<sup>155,156</sup> Thus, the optimum electrode structure has been developed by trial and error to tune the performance. However, to improve the charge–discharge characteristics to nearly the theoretical performance, it is necessary to understand the governing factor and to achieve a composite electrode design that causes an ideal reaction.

The reaction distribution has a strong relationship with the charge–discharge characteristics of the composite electrodes. In a composite electrode, the effective resistance is varied at the point of a composite electrode, and the electrode reaction does not proceed uniformly. If such a reaction distribution is caused, Joule heat is preferentially generated due to the concentration of current in a specific region, which affects safety. Since the reaction tends to further proceed in the region where heat is generated, only a specific region is charged and discharged, thereby accelerating the degradation of the active material. In large-scale lithium-ion batteries used in electric vehicles, the reaction distribution problem becomes remarkable because charging and discharging are carried out at a large current.

The reaction distribution phenomena are categorized into two types. The first is the reaction heterogeneity of the active material in the electrode thickness direction. In a composite electrode, electrons are supplied from the current collector side, and ions are supplied from the separator side. At each point in the in-plane direction, the resistance component encountered by electrons and ions is different. The inside of the composite electrode has a complicated conduction path, and the effective potential at each reaction point is heterogeneously distributed. It is predicted that the reaction distribution is

caused by the heterogeneity of the ion conduction resistance and electron conduction resistance in a composite electrode.<sup>157–159</sup> The second is the concentration distribution of the electrolyte. In an electrolyte used in a lithium-ion battery, the transfer number of lithium ions in an electrolyte is small, approximately 0.4.<sup>160</sup> Therefore, during high-rate charging and discharging, salt concentration gradient forms in the electrolyte. In addition, the electrolyte is immersed in nanometer- or micrometer-scale voids in the composite electrode, which disturbs the

relaxation of the salt concentration gradient toward the original concentration. When the concentration of the electrolyte changes, its ionic conductivity changes,<sup>161</sup> which causes reaction heterogeneity in the composite electrode.

General electrochemical measurements provide information on the entire composite electrode, so it is not possible to directly measure the local reaction sites inside the electrode or the heterogeneity of the resistance. Therefore, simulating the phenomenon inside the electrode

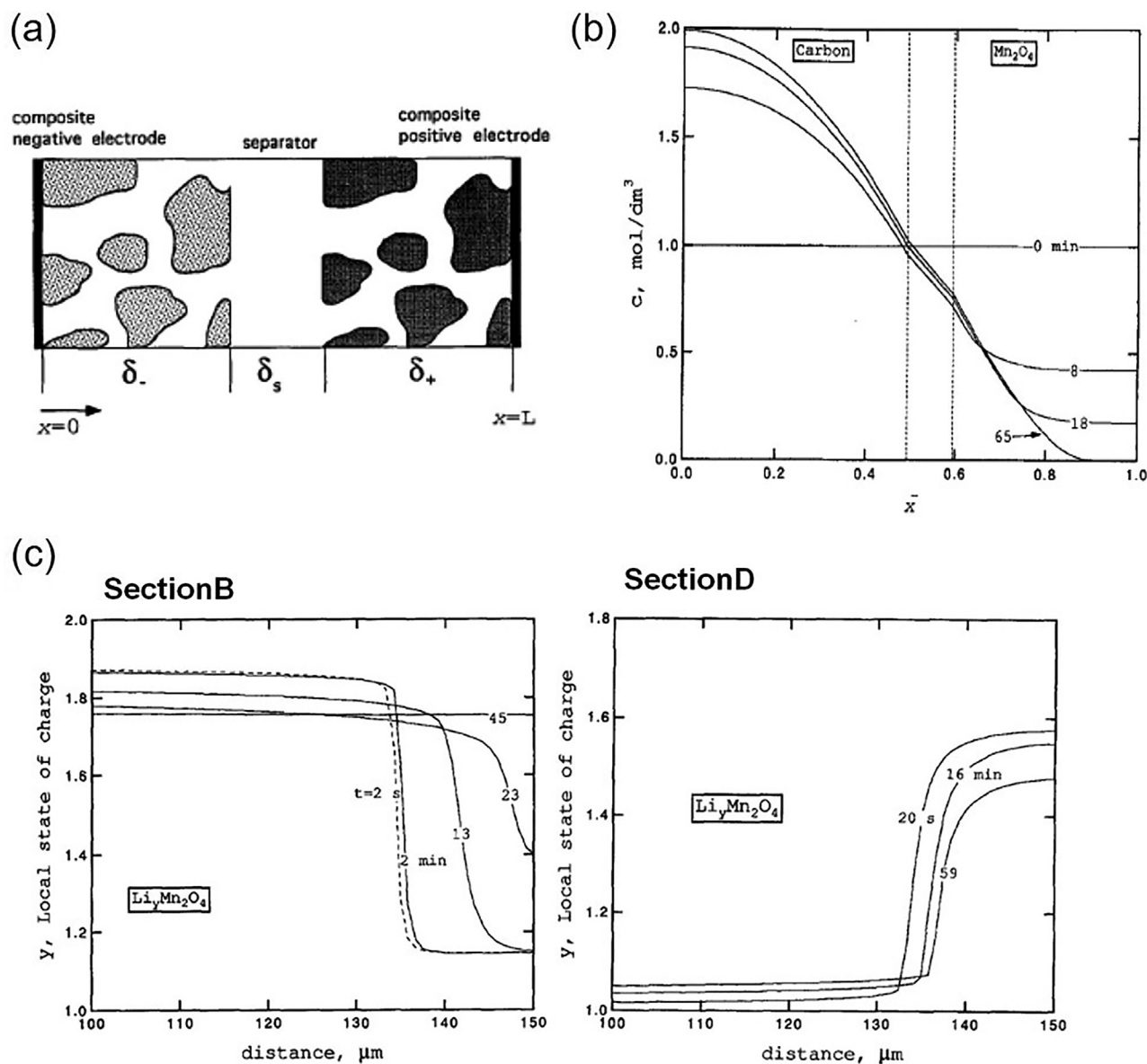


**FIG. 16.** Simulation results of lithium-ion concentration change in electrode and electrolyte. (a) Coordinates of a cell consisting of a composite anode, composite cathode, and separator.<sup>157</sup> (b) Concentration profiles across the cell during galvanostatic discharging at  $i = 4.0 \text{ mA cm}^{-2}$ . The separator region is marked by dashed lines. Reprinted with permission from Fuller *et al.*, *J. Electrochem. Soc.* **141**, 1–10 (1994). Copyright 1994 IOP Publishing.<sup>162</sup> (c) Local state of charge (SOC) across the cathode. The distance was measured from the anode–separator interface. The left and right curves correspond to sections B and D, respectively. Reprinted with permission from Fuller *et al.*, *J. Electrochem. Soc.* **141**, 982–990 (1994). Copyright 1994 IOP Publishing.<sup>163</sup>

by a mathematical technique was carried out. Newman *et al.* described one-dimensional locus quantities that do not distinguish electrolyte and solid phases, as shown in Fig. 16(a).<sup>157</sup> Simulations were conducted using a composite electrode with a carbon anode and  $\text{LiMn}_2\text{O}_4$  cathode.<sup>162</sup> As the current value increases, a large voltage drop occurs at the end of discharging. The calculated electrolyte concentration of the system discharged at  $4.0 \text{ mA cm}^{-2}$  is shown in Fig. 16(b). The electrolyte concentration is doubled near the current collector of the anode at the end stage of discharging, and the electrolyte concentration is almost 0 near the current collector of the cathode. Such a concentration distribution causes a large polarization at the end of discharging, decreasing in battery performance.

The reaction–distribution relaxation phenomena were also calculated using a composite electrode consisting of a  $\text{LiMn}_2\text{O}_4$  cathode and a Li anode, as shown in Fig. 16(c).<sup>163</sup> First,  $\text{Li}_{1.2}\text{Mn}_2\text{O}_4$  was discharged to  $\text{Li}_{1.8}\text{Mn}_2\text{O}_4$ , and the cell was kept for 1 h (labeled B). Next, the cell was charged to  $\text{Li}_{1.2}\text{Mn}_2\text{O}_4$  and kept under this condition for 1 h (labeled D). The time dependency of the state of charge (SOC) distribution at B and D indicates that the electrode reaction proceeds preferentially from the electrode surface at both B and D immediately after charging and discharging, which is deemed due to ionic conduction in the composite electrode being a rate-limiting process of the cell reaction. However, the SOC distribution at B is completely relaxed after 45 min, while the SOC distribution at D remains heterogeneous, even after 59 min. This phenomenon can be explained by the composition–open circuit voltage (OCV) curve of manganese spinel. For the composition at B, the composition–OCV curves have a slope, so the different SOC around this composition have different electrochemical potentials.

Lithium ions can migrate due to the difference between the potentials within this electrode, and the SOC distribution is relaxed. On the other hand, for the composition at D, the composition–OCV curve has no slope, so the potential does not change, even if the SOC is different. In this case, there is no driving force for lithium ions to migrate.

Attempts have been made to fabricate a galvanic cell and to measure the current and potential distributions. Ng *et al.*<sup>158</sup> and Hess *et al.*<sup>159,164</sup> measured current and potential distributions by inserting electronic and ionic conductors into a composite electrode. Mitsuda and Takemura also measured the potential profiles of a cathode surface by placing a large number of reference electrodes.<sup>165</sup> A direct observation technique has been reported in which the in-plane profiles of graphite and  $\text{LiFePO}_4$  have been measured using the change in the color of active materials depending on their composition.<sup>166,167</sup>

X ray-based measurements are a powerful tool to prove such a reaction distribution. J. Liu *et al.* used synchrotron radiation x rays focused on a  $2 \times 5 \mu\text{m}^2$  region and analyzed the in-plane reaction distribution of the  $\text{LiFePO}_4$  cathode by measuring the diffraction pattern at each specific position [Figs. 17(a)–17(d)].<sup>23</sup> The SOC for each specific position was estimated from the ratio of peak intensities exhibited by the two compositions. They reported that when charged at a low rate, the reaction proceeded uniformly, but when charged at a high rate, the electrode surface reacted preferentially. Reaction distribution measurements using Raman spectroscopy have also been reported.<sup>168,169</sup> Nanda *et al.* used Raman spectroscopy with position resolution achieved using a  $1\text{-}\mu\text{m}$ -diameter laser to measure the response profile along the outer plane of the cathode [Fig. 17(e)].

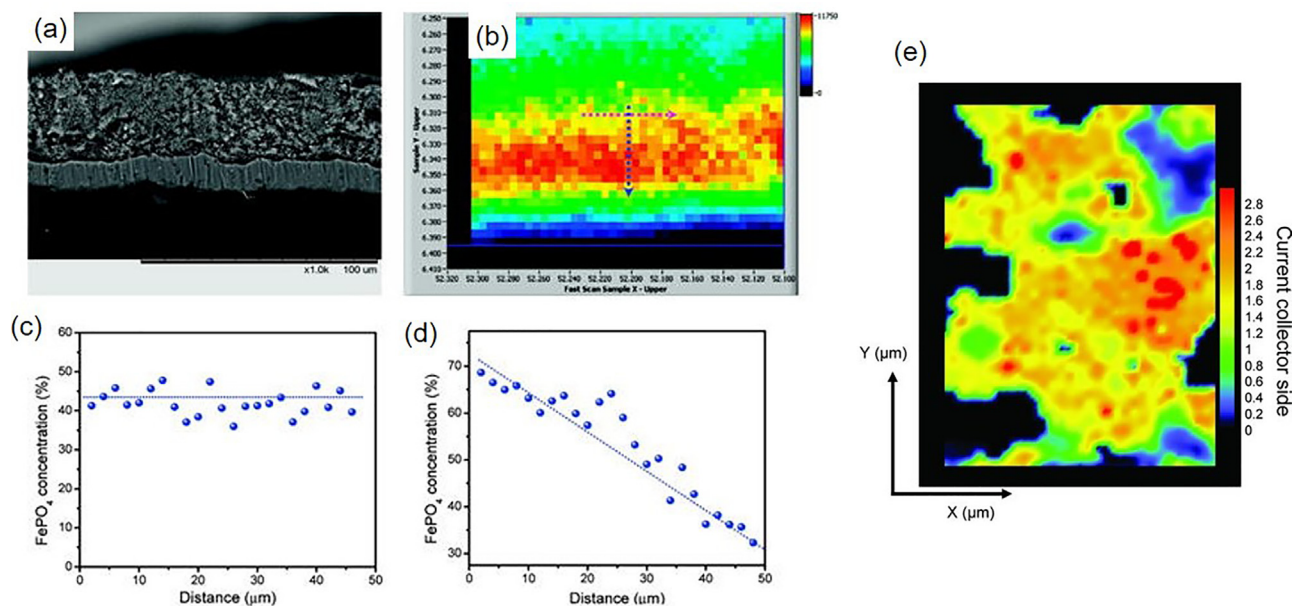


**FIG. 17.** Observed reaction distribution phenomena in composite electrode of lithium-ion batteries. (a) SEM image of the cross section  $\text{LiFePO}_4$  electrode for micro-XRD. (b) Fe fluorescence intensity map of the cross section of  $\text{LiFePO}_4$  electrode. The approximate vertical locations of the line scans are superimposed.  $\text{FePO}_4$  phase ratio as a function of the electrode depth along the vertical direction of 50% SOC charged  $\text{Li}_{0.5}\text{FePO}_4$  at (c)  $20 \text{ mA g}^{-1}$  and (d)  $3 \text{ A g}^{-1}$ . Reprinted with permission from Liu *et al.*, *J. Phys. Chem. Lett.* **1**, 2120–2123 (2010). Copyright 2010 American Chemical Society.<sup>23</sup> (e) SOC mapping from Raman spectra of the degraded NCA electrode along the edge. Reprinted with permission from Nanda *et al.*, *Adv. Funct. Mater.* **21** 3282–3290 (2011). Copyright 2011 Wiley-VCH.<sup>168</sup>



A direct observation of the reaction distribution is not easy because it relaxes over time, causing it to diverge from the mathematical simulation prediction. The origin of the relaxation behavior of the reaction heterogeneity phenomenon of active materials is introduced by comparing  $\text{LiCoO}_2$ , which has a gradient in the composition–potential curve, and  $\text{LiFePO}_4$ , which has a plateau region over a wide composition. With the optics available at the synchrotron radiation beamline, x rays can be focused on a less than  $1\text{-}\mu\text{m}$ -square region to estimate the difference in reactivity progression at multiple locations of a composite electrode.<sup>170</sup> The charged states of  $\text{LiCoO}_2$  and  $\text{LiFePO}_4$  at the current collector side and the inner part can be compared on the basis of XANES results.<sup>171</sup> To verify the relaxation behavior of the reaction distribution, the electrodes after charging were prepared as a sample that was immediately disassembled after charging and a sample that was disassembled after being held for 15 h in an open circuit state after charging. Immediately after charging both the  $\text{LiCoO}_2$  and  $\text{LiFePO}_4$  electrodes, the absorption edge energy of the center portion is located on the higher energy side rather than near the current collector [Figs. 18(a) and 18(b)]. This result indicates that the electrode active material near the current collector is in a low charged state. The

relaxation behavior of the reaction distribution observed immediately after charging varies greatly depending on the active material. In the XANES spectra of  $\text{LiCoO}_2$ , the spectra from two different points match, which shows the disappearance of the reaction distribution [Fig. 18(c)]. On the other hand, in the  $\text{LiFePO}_4$  electrode shown in Fig. 18(d), the reaction distribution observed immediately after charging is retained, even after 15 h under the open circuit condition.

While the composition–potential curve of  $\text{LiCoO}_2$  shows a gradual potential gradient, as shown at the top of Fig. 19(a), that of  $\text{LiFePO}_4$ , shown in Fig. 19(b), has a wide plateau region. When a reaction distribution occurs in an electrode, active materials with different compositions are present in the composite electrode. In  $\text{LiCoO}_2$  electrodes, the composition distribution of the active material causes a potential gradient. Lithium ions migrate through the electrolyte toward eliminating this potential gradient, and the reaction distribution in the  $\text{LiCoO}_2$  electrode disappears. On the other hand, in the  $\text{LiFePO}_4$  electrode, since the potential is constant over a wide region, there is no potential gradient, even if the reaction distribution occurs in the same electrode. Therefore, there is no driving force for lithium ions to move and the reaction distribution remains. The relaxation

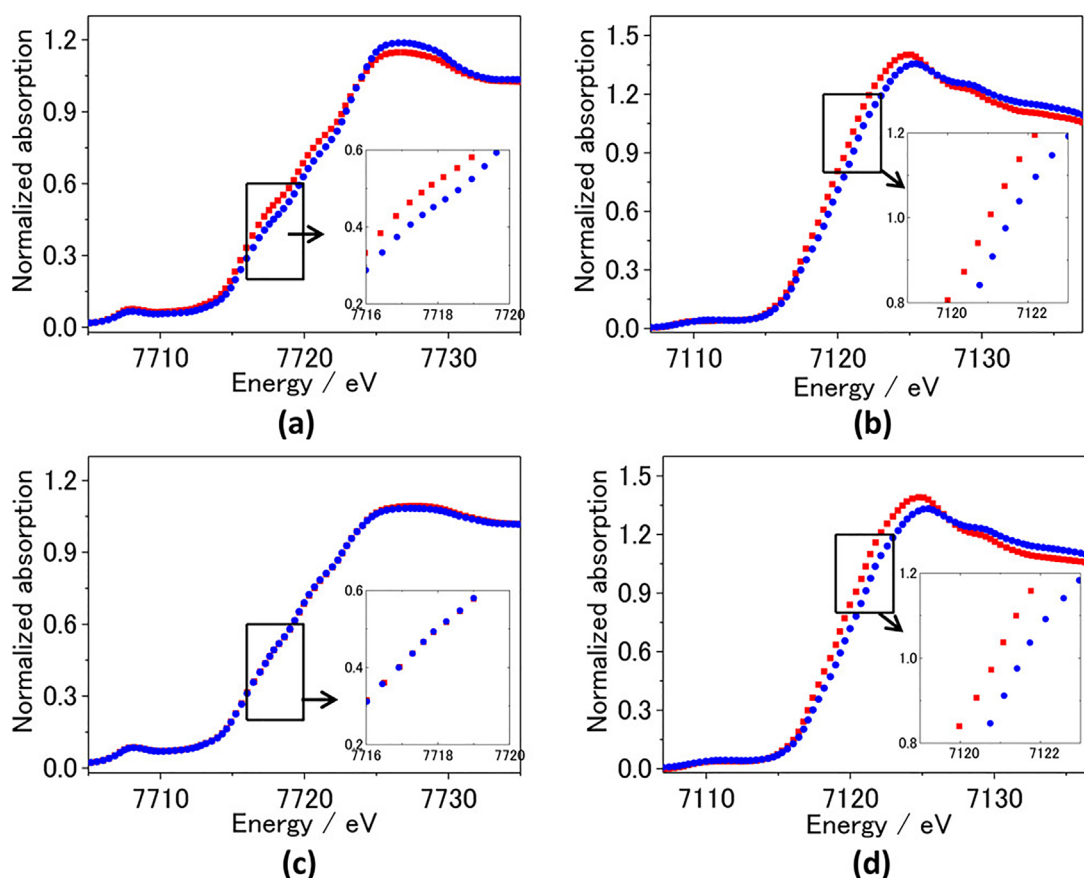


**FIG. 18.** Co and Fe K-edge XANES for each location of charged  $\text{LiCoO}_2$  [(a) and (c)] and  $\text{LiFePO}_4$  [(b) and (d)] at 1C. Blue corresponds to the center of the electrode, and red corresponds to the current collector side. [(a) and (b)] Cell immediately dismantled after charging and [(c) and (d)] the cell dismantled after 15 h. Reprinted with permission from Tanida *et al.*, *J. Phys. Chem. C* **120**, 4739–4743 (2016). Copyright 2016 American Chemical Society.<sup>171</sup>

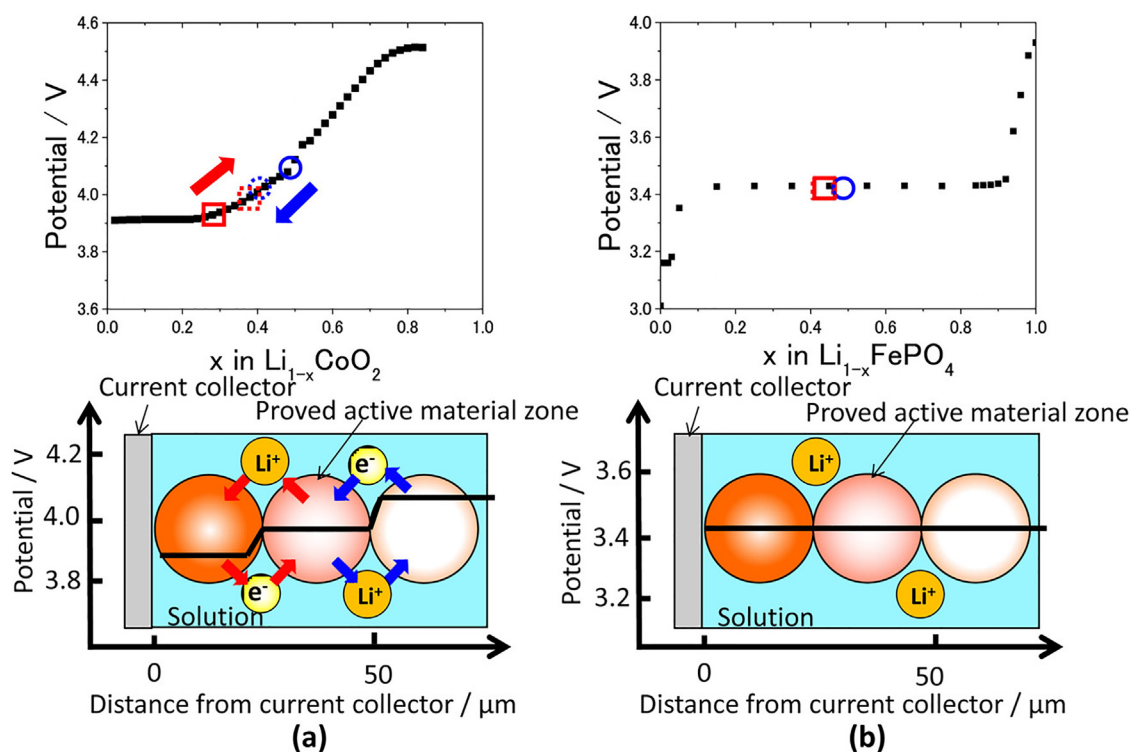


**FIG. 19.** (Top) Composition–potential curves of active materials and (bottom) schematic representation showing the potential of the active material and its relaxation behavior when the reaction distribution occurs: (a)  $\text{LiCoO}_2$  and (b)  $\text{LiFePO}_4$ . Reprinted with permission from Tanida *et al.*, *J. Phys. Chem. C* **120**, 4739–4743 (2016). Copyright 2016 American Chemical Society.<sup>171</sup>

behavior of the reaction distribution is shown experimentally to be a phenomenon based on the diffusion of lithium ions, and this driving force is not a concentration gradient but a chemical potential gradient.

Regarding the relaxation phenomenon of the reaction distribution, it is important to grasp the time order. Although reaction distribution analysis in the in-plane direction by *operando* measurement becomes important, it has been challenging to detect the reaction progress of the active material in the in-plane direction without disassembling the battery. High-energy confocal XRD can be used to obtain a diffraction pattern of specific points in composite electrodes [Fig. 20(a)]. Depth-resolved charge–discharge states and subsequent reaction heterogeneity in an open circuit state have been reported.<sup>172</sup> Since the position of the diffraction peak corresponds to the state of charge, the reactive heterogeneous state can be estimated in  $\text{LiNi}_{0.33}\text{Mn}_{0.33}\text{Co}_{0.33}\text{O}_2$ . Figure 20(b) plots the change in the diffraction peak angle for each location in the discharge reaction and subsequent open circuit state. During the discharge reaction, the site close to the separator reacts preferentially, and after the discharge reaction, the overall discharge state is observed to be similar. This time order is approximately 30 min, showing that the heterogeneous reaction state of the active material is relatively easy to relax within an hour. In a high-rate charge–discharge reaction, the reaction heterogeneity phenomenon occurs continuously without relaxation, which has a large influence on its performance.

As mentioned above, the electrode morphology impacts the charge–discharge characteristics. Figure 21(a) shows a 10C discharge curve of  $\text{LiFePO}_4$  with different void ratios. The equilibrium potential of  $\text{LiFePO}_4$  is approximately 3.45 V for most compositions. The higher the porosity is, the smaller the discharge potential is. This indicates that there is Ohmic loss due to reduced contact, and two possible factors are considered. One factor is the electron resistance in the composite electrode. The contact between particles is insufficient for composite electrodes with high porosity. Therefore, a good electron conduction path is not formed, the effective electron conduction resistance in the compound electrode becomes large, and it is considered to exhibit a large Ohmic loss. The other factor is the contact resistance between the current collector and composite electrode. It is also conceivable that contact between the current collector and composite electrode is insufficient, and a large contact resistance is generated. In the case of the electrode having low porosity, a large voltage drop is observed at the end of discharging, and the capacity decreases. This is because the effective ionic conductivity in the composite electrode is lower than that of the composite electrode with a high porosity. In the narrow and distorted vacancies, lithium-ion conduction is difficult, which causes a sharp voltage drop at the end of discharging a composite electrode with low porosity.

Two-dimensional XAS<sup>173</sup> provides clear imaging of reaction inhomogeneity in the in-plane direction, as shown in Fig. 21(b). In the mapping, the absorption edge energy corresponding to the discharged

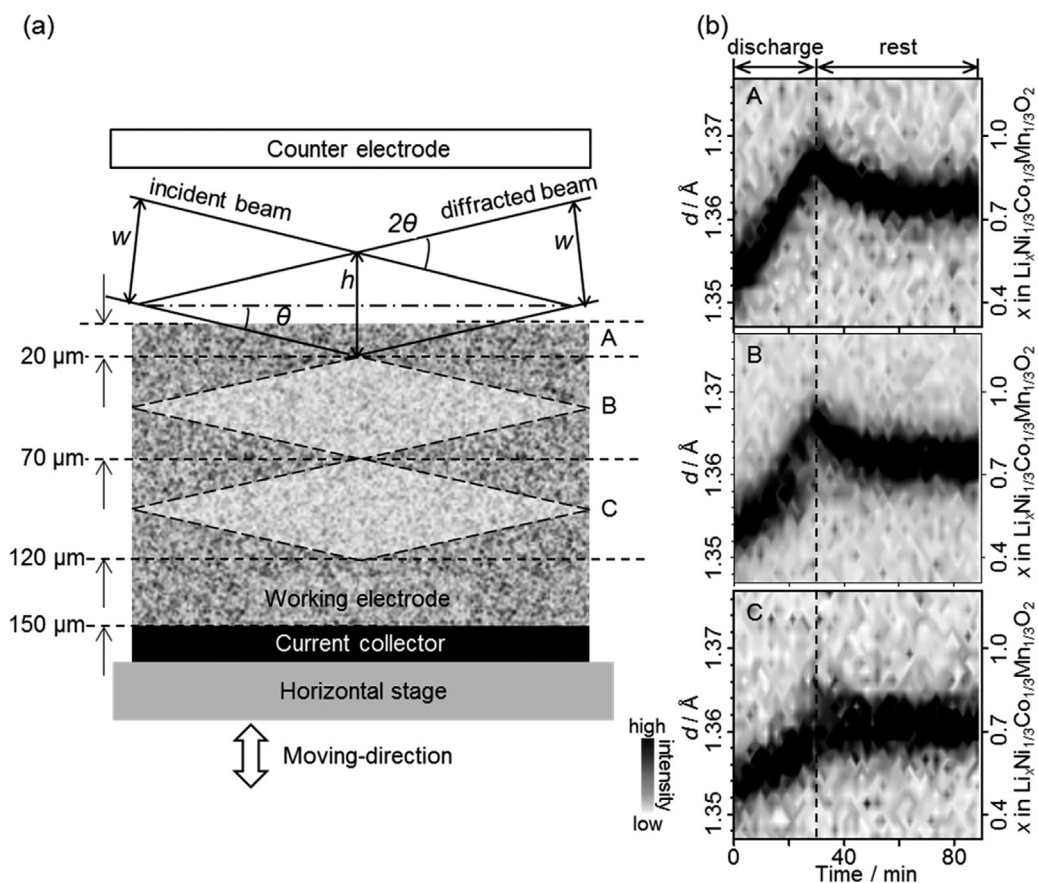


**FIG. 20.** Schematic illustration and analyzed data of confocal XRD during battery operation. (a) Measuring points of the *operando* confocal XRD method for measuring the response distribution in the thickness direction. (b) Changing behavior of the diffraction peak angle at each position measured when discharging  $\text{LiNi}_{0.33}\text{Mn}_{0.33}\text{Co}_{0.33}\text{O}_2$ . Reprinted with permission from Murayama *et al.*, *J. Phys. Chem. C* **118**, 20750–20755 (2014). Copyright 2014 American Chemical Society.<sup>172</sup>

state is described for each position, and the discharge depth is visualized in the in-plane direction. When the porosity of the composite electrode is 36% or 44%, the reaction proceeds preferentially on the separator side, and when the porosity is 48% or 56%, the reaction proceeds uniformly. Two-dimensional XAS imaging shows that the occurrence of the reaction distribution becomes remarkable as the electrode porosity decreases.

Since the reaction distribution is determined by the balance between the ionic conductivity and the electronic conductivity in the composite electrode, it is necessary to discuss both separately. However, the effective ionic and electronic conductivities of composite electrodes are difficult to separate and measure due to the contributions of their complex three-dimensional structures. The six-probe method proposed by Siroma *et al.* enables the measurement of ionic and electronic conductivities.<sup>174</sup> The effective electron conductivity in a composite electrode increases linearly (hundreds of  $\text{mS cm}^{-1}$ ) as the porosity decreases.<sup>150</sup> This is considered to be because the adhesion between the conductive agents is improved and the contact resistance is reduced. Thus, the electron conductivity in the composite electrode is high and does not become rate limiting. On the other hand, the effective ionic conductivity in the composite electrode is  $6 \text{ mS cm}^{-1}$

for the electrode with more than 50% porosity and two orders of magnitude smaller than that of the electronic conductivity [Fig. 21(c)]. The ionic conductivity sharply decreases at a porosity of 45% or less, which is different from the ionic conductivity calculated from the bulk conductivity. When the void is small, the apparent conduction path becomes long, which decreases the effective ionic conduction in the highly pressed composite electrodes.

In a composite electrode, ionic conduction is mostly the rate limiting, and the value decreases with decreasing porosity. This greatly changes the balance between the potentials of electrons and lithium ions, as shown in Fig. 21(d). This inhomogeneous potential distribution causes the reaction to be heterogeneous in the in-plane direction. When the porosity is small, the potential distribution of ions is large in the composite electrode, and the reaction proceeds preferentially in the vicinity of the electrode surface so that the active material on the current collector side does not react, which decreases the dischargeable capacity. By the neutron analysis using the 18 650 type all battery, it is observed that the phase change of graphite anode is rate-dependent. This is interpreted to be a result of reaction heterogeneity inside the composite electrode. In some cases, the formation of crystalline phases with slow lithium diffusion and thermodynamically unstable phase

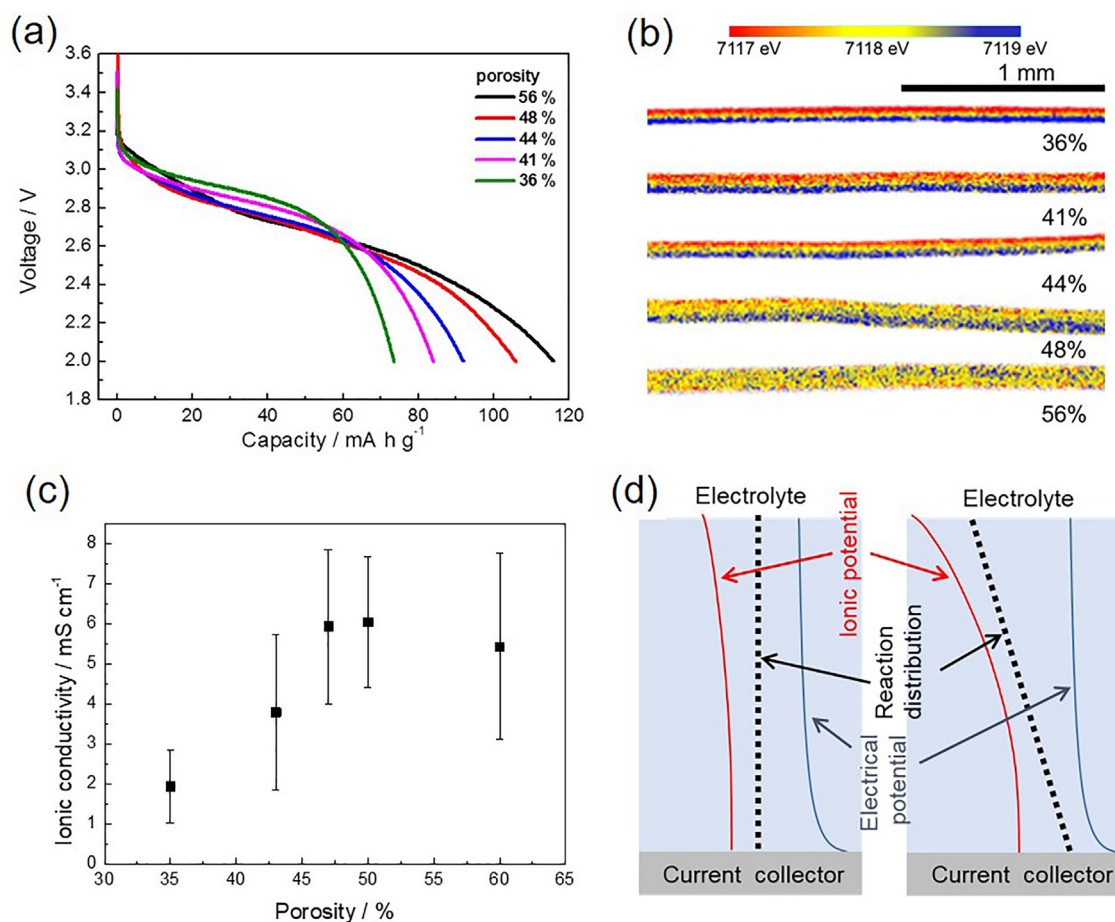


**FIG. 21.** Experimental results of reaction distribution and ionic conduction change in composite electrodes governing discharge capacity. (a) Discharge properties of LiFePO<sub>4</sub> electrodes with different porosities at a 10C rate. (b) Cross section of the two-dimensional mapping of absorption energy at the Fe K-edge of LiFePO<sub>4</sub> composite electrodes. The current collector is located on the bottom. (c) Effective ionic conductivities as a function of porosity in LiFePO<sub>4</sub> composite electrodes. (d) Ionic and electrical potential distribution for the high-porosity electrode and low-porosity electrode. Reprinted with permission from Orikasa *et al.*, *Sci. Rep.* **6**, 26382 (2016). Copyright 2016 Authors, licensed under a Creative Commons Attribution (CC BY) license.<sup>150</sup>

formation is detected.<sup>175</sup> The rate dependence of the concentration change in the depth direction of LiFePO<sub>4</sub> electrode has been measured by Neutron depth profile. At high rates, a preferential reaction on the electrolyte side is observed due to the rate-determined ionic conduction. On the other hand, at sufficiently slow rates, the effects of electron conduction and nucleation rate determination are predominant, and the preferential reaction sites are different.<sup>176</sup> In spatially resolved x-ray diffraction computed tomography, the reaction distribution can be visualized in three dimensions. 1.2-mm-thick LiFePO<sub>4</sub> composite electrode, even at a low rate of C/10, the reaction proceeds preferentially from the separator and current collector sides.<sup>177</sup>

In recent years, not only active materials but also electrolyte heterogeneity has been analyzed. For example, there have been reports on measuring the change in salt concentration during the charging and discharging reaction of a lithium-ion battery by NMR imaging (MRI)<sup>178,179</sup> and x-ray phase imaging.<sup>180</sup> Figure 22(a) is a result of measuring the concentration change of the electrolyte using a model

cell of the lithium electrode.<sup>178</sup> In a state where current flows, in an electrolyte with a thickness of 10 mm, there is a case where the salt concentration becomes 1.5 M or more or 0.5 M or less. Furthermore, it can be easily imagined that this change occurs even in a composite electrode, which has been directly detected by the fluorescence x-ray technique [Fig. 22(b)].<sup>181</sup> This is because in a composite electrode, the size of the vacancy is small, and the diffusion of ions slows. In the NMR measurements of a composite electrode in a capacitor, the diffusion coefficient of the composite electrode is estimated to be two orders smaller than the value of the bulk electrode.<sup>182</sup> Therefore, when the current density is large, the relaxation of the salt concentration distribution becomes slower than the time scale of the charge-discharge reaction, and the increase or decrease in the concentration of the electrolyte in the composite electrode may greatly affect its characteristics.<sup>183</sup>

The change in salt concentration greatly affects the charge-discharge characteristics because it brings about an increase and

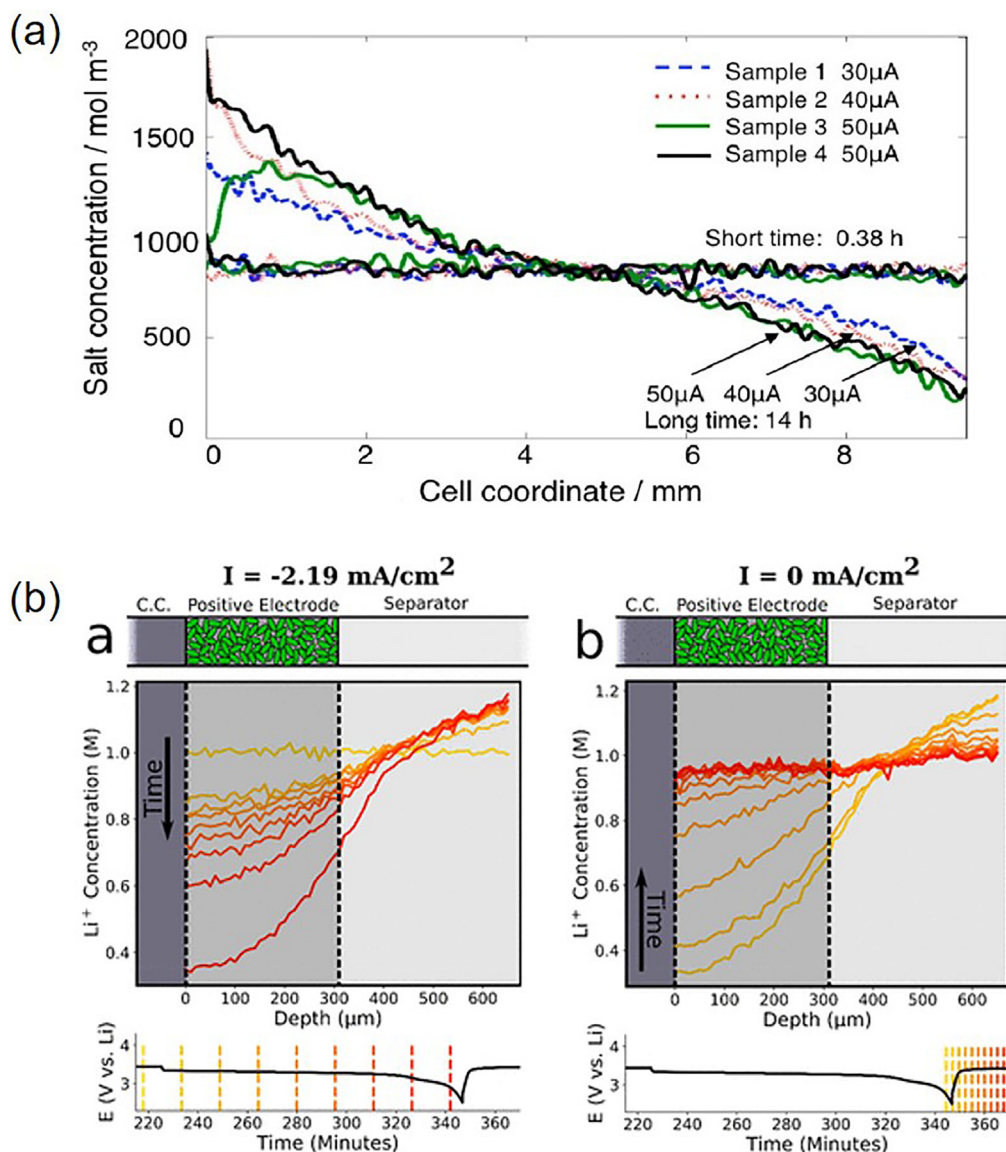


**FIG. 22.** Detection of lithium-ion concentration change in electrolyte during battery operation. (a) Change in the  $\text{LiPF}_6$  salt concentration between lithium electrodes, as measured using NMR. Reprinted with permission from Klett *et al.*, *J. Am. Chem. Soc.* **134**, 14654–14657 (2012). Copyright 2012 American Chemical Society.<sup>178</sup> (b)  $\text{Li}^+$  concentration profile in the cell while “a” discharging at a current of 0.4C and during “b” rest period. The schematic (top) displays the various cell components as a function of depth. The bottom inset shows the potential response as a function of time, where the vertical dashed lines indicate the time for the corresponding colored line in the gradient plot. Reprinted with permission from Dawkins *et al.*, *Anal. Chem.* **92**(16), 10908–10912 (2020). Copyright 2020 American Chemical Society.<sup>181</sup>

decrease in the conductivity of electrolytes. Studies using the previously described confocal XRD method to investigate the reaction distribution behavior of  $\text{LiNi}_{0.33}\text{Mn}_{0.33}\text{Co}_{0.33}\text{O}_2$  cathode with different salt concentrations show that the local increase or decrease in the number of lithium ions causes capacity degradation in the direction of decreasing conductivity.<sup>184</sup> Changes in salt concentration are assumed to have a significant impact on charge–discharge cycles, especially at high rates, due to the relatively slow relaxation process. By analyzing the reaction distribution during the charge–discharge cycling shown

in Fig. 23, even if the reaction distribution is eliminated by charging once, spreading of the reaction heterogeneity at the time of discharge during every cycle is observed.<sup>183</sup> *Operando* XRD in 20-micrometer steps using a half-cell with a 170- $\mu\text{m}$ -thick electrode of  $\text{LiNi}_{0.8}\text{Co}_{0.1}\text{Mn}_{0.1}\text{O}_2$  is reported. In this report, it is also clear that the reaction from the separator side is preferential and that the real SOC range in active materials changes with cycling.<sup>185</sup>

In recent years, all-solid-state rechargeable batteries have been increasingly studied as candidates for next-generation rechargeable

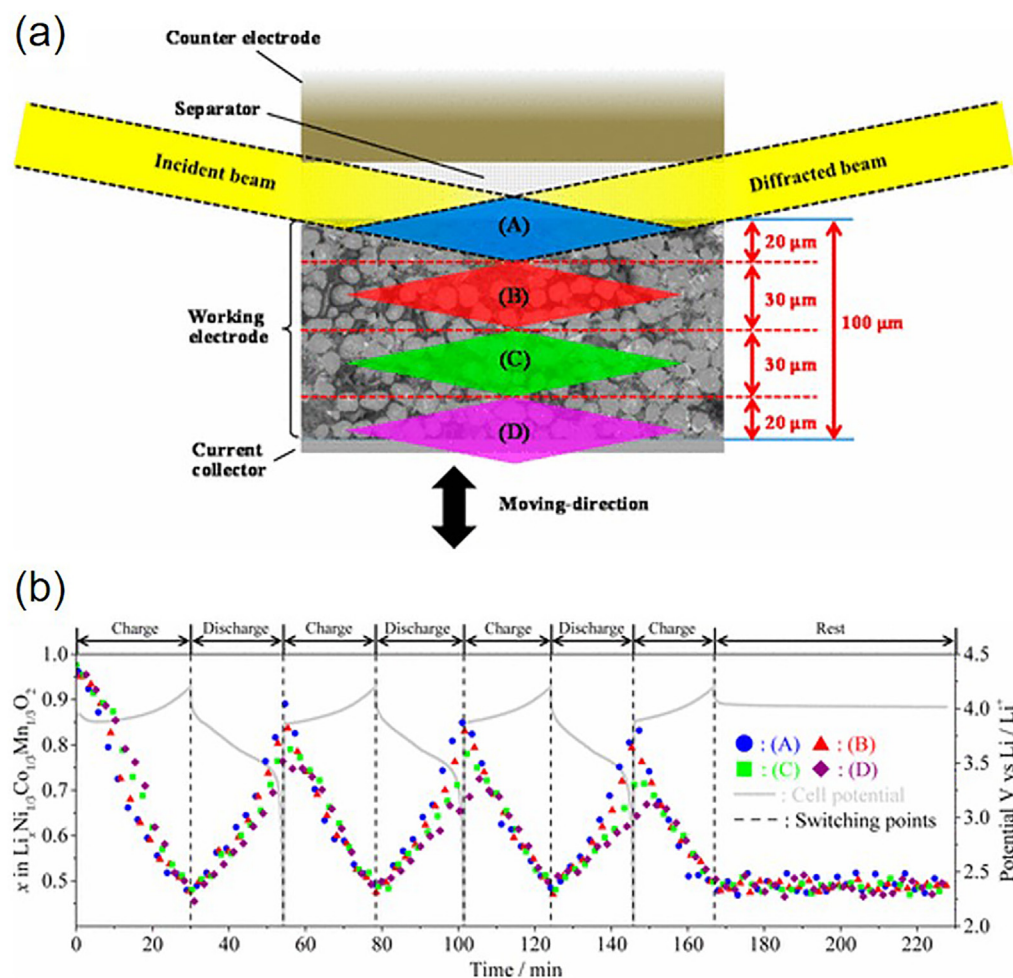


**FIG. 23.** Reaction distribution phenomena during battery cycling. (a) Schematic illustration of the cross-sectional composite electrode with a confocal point for *operando* energy-scanning confocal XRD measurements. (b)  $\text{Li}^+$  concentration profile in the  $\text{LiNi}_{0.33}\text{Mn}_{0.33}\text{Co}_{0.33}\text{O}_2$  composite electrode during charge–discharge cycling at 1C. The color points correspond to positions (A)–(D) at the cross section of the composite electrode shown in (a). The cell potential during the XRD measurements is provided in the gray plots. Reprinted with permission from Kitada *et al.*, *J. Phys. Chem. C* **121**, 6018–6023 (2017). Copyright 2017 American Chemical Society.<sup>183</sup>

batteries. In regard to practicality, it is important to verify whether all-solid-state rechargeable batteries differ from existing lithium-ion batteries in terms of generating a reaction distribution. In the case of all-solid-state rechargeable batteries, since the transfer rate of the carrier ions of the solid electrolyte is 1,<sup>186,187</sup> the salt concentration distribution is not caused in principle, which has been experimentally proven.<sup>188</sup> The absence of concentration heterogeneity in electrolytes, even during a high-rate charge–discharge reaction, could realize fast charging and discharging in a short time. Notably, a fast charge–discharge response has been reported,<sup>189</sup> and it is expected to be deployed in electric vehicles. Although the concentration of the solid electrolyte is constant, heterogeneous reactions are still observed, which is effectively due to low ionic conduction. Figure 24 shows a three-dimensional reaction state with the CT-x-ray absorption spectrum of an all-solid-state rechargeable battery.<sup>190</sup> The color change is heterogeneous when the charge reaction proceeds. Compared with

lithium-ion batteries, in all-solid-state batteries, other factors, such as the contact resistance of the solid interface, are needed to discuss the reaction heterogeneity.

## VI. SUMMARY

The charging–discharging of lithium-ion batteries consists of hierarchical and nonequivalent chemical reactions with a wide range of time and spatial scales, which contain physicochemical phenomena. We have reviewed the recently developed analytical techniques using synchrotron x rays and the reaction phenomena in regard to electrode–electrolyte interfaces as the starting point of the reaction, phase change behavior of active materials, and reaction distributions of composite electrodes. To improve the performance of lithium-ion batteries and to realize next-generation novel rechargeable batteries, the factor governing overall battery performance should be understood. Reaction analysis in terms of physicochemical phenomena will

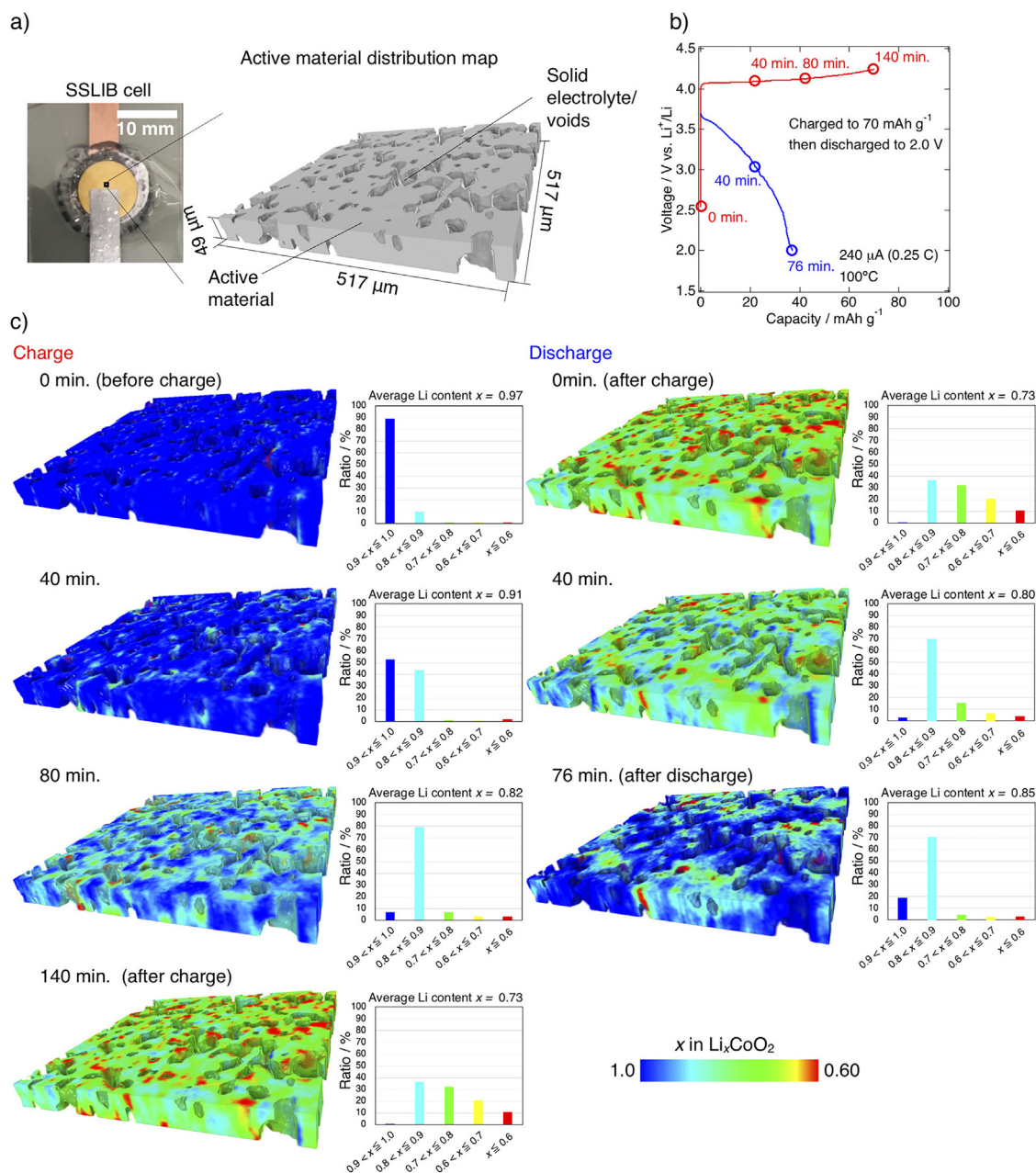


**FIG. 24.** Reaction distribution mapping of all-solid-state battery cathode. (a) Photograph of the used solid-state battery and the observed area of the CT-XANES measurements. (b) Charge–discharge profile of the cell. (c) 3D charging state maps during charging and discharging. The blue and red regions correspond to discharged and charged spots, respectively. The transparent regions indicate the solid electrolyte or voids. Reprinted with permission from Kimura *et al.*, *J. Phys. Chem. Lett.* **11**, 3629–3636 (2020). Copyright 2020 American Chemical Society.<sup>190</sup>

assist the enhancement of battery performance based on basic science without relying on trial and error.

## AUTHOR DECLARATIONS

### Conflict of Interest

The authors declare no conflict of interest.

## DATA AVAILABILITY

Data sharing is not applicable to this article as no new data were created or analyzed in this study.

## REFERENCES

- <sup>1</sup>D. Castelvetti and E. Stoye, *Nature* **574**, 308 (2019).

- <sup>2</sup>J. M. Tarascon and M. Armand, *Nature* **414**(6861), 359–367 (2001).
- <sup>3</sup>V. Etacheri, R. Marom, R. Elazari, G. Salitra, and D. Aurbach, *Energy Environ. Sci.* **4**(9), 3243–3262 (2011).
- <sup>4</sup>M. Winter, B. Barnett, and K. Xu, *Chem. Rev.* **118**(23), 11433–11456 (2018).
- <sup>5</sup>K. Mizushima, P. C. Jones, P. J. Wiseman, and J. B. Goodenough, *Mater. Res. Bull.* **15**(6), 783–789 (1980).
- <sup>6</sup>R. Yazami and P. Touzain, *J. Power Sources* **9**(3–4), 365–371 (1983).
- <sup>7</sup>P. G. Bruce and M. Y. Saidi, *J. Electroanal. Chem.* **322**(1), 93–105 (1992).
- <sup>8</sup>M. Nakayama, H. Ikuta, Y. Uchimoto, and M. Wakihara, *J. Phys. Chem. B* **107**(38), 10603–10607 (2003).
- <sup>9</sup>K. Dokko, N. Nakata, Y. Suzuki, and K. Kanamura, *J. Phys. Chem. C* **114**(18), 8646–8650 (2010).
- <sup>10</sup>K. Dokko, N. Nakata, and K. Kanamura, *J. Power Sources* **189**(1), 783–785 (2009).
- <sup>11</sup>B. A. Johnson and R. E. White, *J. Power Sources* **70**(1), 48–54 (1998).
- <sup>12</sup>P. Sedigh Rahimabadi, M. Khodaei, and K. R. Koswattage, *X-Ray Spectrom.* **49**(3), 348–373 (2020).
- <sup>13</sup>G. Bunker, *Introduction to XAFS: A Practical Guide to X-Ray Absorption Fine Structure Spectroscopy* (Cambridge University Press, Cambridge, 2010).
- <sup>14</sup>Y. Sakurai, K. Uesugi, and T. Ishikawa, *Synchrotron Radiat. News* **33**(6), 37–43 (2020).
- <sup>15</sup>Y. Orikasa, T. Maeda, Y. Koyama, T. Minato, H. Murayama, K. Fukuda, H. Tanida, H. Arai, E. Matsubara, Y. Uchimoto, and Z. Ogumi, *J. Electrochem. Soc.* **160**(5), A3061–A3065 (2013).
- <sup>16</sup>Y. Orikasa, T. Maeda, Y. Koyama, H. Murayama, K. Fukuda, H. Tanida, H. Arai, E. Matsubara, Y. Uchimoto, and Z. Ogumi, *Chem. Mater.* **25**(7), 1032–1039 (2013).
- <sup>17</sup>C. Bressler and M. Chergui, *Chem. Rev.* **104**(4), 1781–1812 (2004).
- <sup>18</sup>G. R. Shulman, Y. Yafet, P. Eisenberger, and W. E. Blumberg, *Proc. Natl. Acad. Sci. U.S.A.* **73**(5), 1384–1388 (1976).
- <sup>19</sup>A. Deb, U. Bergmann, S. P. Cramer, and E. J. Cairns, *Electrochim. Acta* **50**(25–26), 5200–5207 (2005).
- <sup>20</sup>J. B. Leriche, S. Hamet, J. Shu, M. Morcrette, C. Masquelier, G. Ouvrard, M. Zerrouki, P. Soudan, S. Belin, E. Elkaim, and F. Baudet, *J. Electrochem. Soc.* **157**(5), A606–A610 (2010).
- <sup>21</sup>X. J. Wang, C. Jaye, K. W. Nam, B. Zhang, H. Y. Chen, J. M. Bai, H. Li, X. J. Huang, D. A. Fischer, and X. Q. Yang, *J. Mater. Chem.* **21**(30), 11406–11411 (2011).
- <sup>22</sup>X. Q. Yu, Q. Wang, Y. N. Zhou, H. Li, X. Q. Yang, K. W. Nam, S. N. Ehrlich, S. Khalid, and Y. S. Meng, *Chem. Commun.* **48**(94), 11537–11539 (2012).
- <sup>23</sup>J. Liu, M. Kunz, K. Chen, N. Tamura, and T. J. Richardson, *J. Phys. Chem. Lett.* **1**(14), 2120–2123 (2010).
- <sup>24</sup>F. C. Strobridge, B. Orvananos, M. Croft, H.-C. Yu, R. Robert, H. Liu, Z. Zhong, T. Conolly, M. Drakopoulos, K. Thornton, and C. P. Grey, *Chem. Mater.* **27**(7), 2374–2386 (2015).
- <sup>25</sup>J. B. Goodenough and Y. Kim, *Chem. Mater.* **22**(3), 587–603 (2010).
- <sup>26</sup>P. Ghigna and E. Quartarone, *J. Phys. Energy* **3**(3), 032006 (2021).
- <sup>27</sup>I. Nakai, K. Takahashi, Y. Shiraishi, T. Nakagome, and F. Nishikawa, *J. Solid State Chem.* **140**(1), 145–148 (1998).
- <sup>28</sup>Y. Uchimoto, H. Sawada, and T. Yao, *J. Power Sources* **97–98**, 326–327 (2001).
- <sup>29</sup>M. M. Thackeray, S.-H. Kang, C. S. Johnson, J. T. Vaughey, R. Benedek, and S. A. Hackney, *J. Mater. Chem.* **17**(30), 3112–3125 (2007).
- <sup>30</sup>M. Sathiy, G. Rouse, K. Ramesha, C. P. Laisa, H. Vezin, M. T. Sougrati, M. L. Doublet, D. Foix, D. Gonbeau, W. Walker, A. S. Prakash, M. Ben Hassine, L. Dupont, and J. M. Tarascon, *Nat. Mater.* **12**(9), 827–835 (2013).
- <sup>31</sup>M. Sathiy, A. M. Abakumov, D. Foix, G. Rouse, K. Ramesha, M. Saubane, M. L. Doublet, H. Vezin, C. P. Laisa, A. S. Prakash, D. Gonbeau, G. VanTendeloo, and J. M. Tarascon, *Nat. Mater.* **14**(2), 230–238 (2015).
- <sup>32</sup>N. Yabuuchi, M. Takeuchi, S. Komaba, S. Ichikawa, T. Ozaki, and T. Inamasu, *Chem. Commun.* **52**(10), 2051–2054 (2016).
- <sup>33</sup>N. Yabuuchi, M. Nakayama, M. Takeuchi, S. Komaba, Y. Hashimoto, T. Mukai, H. Shiiba, K. Sato, Y. Kobayashi, A. Nakao, M. Yonemura, K. Yamanaka, K. Mitsuhashi, and T. Ohta, *Nat. Commun.* **7**, 13814 (2016).
- <sup>34</sup>K. Luo, M. R. Roberts, R. Hao, N. Guerrini, D. M. Pickup, Y.-S. Liu, K. Edström, J. Guo, A. V. Chadwick, L. C. Duda, and P. G. Bruce, *Nat. Chem.* **8**(7), 684–691 (2016).
- <sup>35</sup>D.-H. Seo, J. Lee, A. Urban, R. Malik, S. Kang, and G. Ceder, *Nat. Chem.* **8**(7), 692–697 (2016).
- <sup>36</sup>M. Oishi, T. Fujimoto, Y. Takanashi, Y. Orikasa, A. Kawamura, T. Ina, H. Yamashige, D. Takamatsu, K. Sato, H. Murayama, H. Tanida, H. Arai, H. Ishii, C. Yogi, I. Watanabe, T. Ohta, A. Mineshige, Y. Uchimoto, and Z. Ogumi, *J. Power Sources* **222**, 45–51 (2013).
- <sup>37</sup>M. Oishi, K. Yamanaka, I. Watanabe, K. Shimoda, T. Matsunaga, H. Arai, Y. Ukyo, Y. Uchimoto, Z. Ogumi, and T. Ohta, *J. Mater. Chem. A* **4**(23), 9293–9302 (2016).
- <sup>38</sup>M. Oishi, C. Yogi, I. Watanabe, T. Ohta, Y. Orikasa, Y. Uchimoto, and Z. Ogumi, *J. Power Sources* **276**, 89–94 (2015).
- <sup>39</sup>N. Yabuuchi, M. Takeuchi, M. Nakayama, H. Shiiba, M. Ogawa, K. Nakayama, T. Ohta, D. Endo, T. Ozaki, T. Inamasu, K. Sato, and S. Komaba, *Proc. Natl. Acad. Sci. U.S.A.* **112**(25), 7650–7655 (2015).
- <sup>40</sup>K. Nakanishi, D. Kato, H. Arai, H. Tanida, T. Mori, Y. Orikasa, Y. Uchimoto, T. Ohta, and Z. Ogumi, *Rev. Sci. Instrum.* **85**(8), 084103 (2014).
- <sup>41</sup>K. Yamamoto, Y. Zhou, N. Yabuuchi, K. Nakanishi, T. Yoshinari, T. Kobayashi, Y. Kobayashi, R. Yamamoto, A. Watanabe, Y. Orikasa, K. Tsuruta, J. Park, H. R. Byon, Y. Tamenori, T. Ohta, and Y. Uchimoto, *Chem. Mater.* **32**(1), 139–147 (2020).
- <sup>42</sup>K. Suzuki, B. Barbiellini, Y. Orikasa, N. Go, H. Sakurai, S. Kaprzyk, M. Itou, K. Yamamoto, Y. Uchimoto, Y. J. Wang, H. Hafiz, A. Bansil, and Y. Sakurai, *Phys. Rev. Lett.* **114**(8), 087401 (2015).
- <sup>43</sup>H. Hafiz, K. Suzuki, B. Barbiellini, N. Tsuji, N. Yabuuchi, K. Yamamoto, Y. Orikasa, Y. Uchimoto, Y. Sakurai, H. Sakurai, A. Bansil, and V. Viswanathan, *Nature* **594**(7862), 213–216 (2021).
- <sup>44</sup>M. Itou, Y. Orikasa, Y. Gogyo, K. Suzuki, H. Sakurai, Y. Uchimoto, and Y. Sakurai, *J. Synchrotron Radiat.* **22**(1), 161–164 (2015).
- <sup>45</sup>J. Newman, *Trans. Faraday Soc.* **61**, 2229–2237 (1965).
- <sup>46</sup>R. Hausbrand, M. Fingerle, T. Späth, and C. Guhl, *Thin Solid Films* **643**, 43–52 (2017).
- <sup>47</sup>M. Thomas, P. Bruce, and J. Goodenough, *Solid State Ionics* **17**(1), 13–19 (1985).
- <sup>48</sup>M. G. S. R. Thomas, P. G. Bruce, and J. B. Goodenough, *J. Electrochem. Soc.* **132**(7), 1521–1528 (1985).
- <sup>49</sup>M. Itagaki, N. Kobari, S. Yotsuda, K. Watanabe, S. Kinoshita, and M. Ue, *J. Power Sources* **148**, 78–84 (2005).
- <sup>50</sup>L. Simonelli, N. L. Saini, M. Moretti Sala, M. Okubo, I. Honma, T. Mizokawa, and G. Monaco, *Appl. Phys. Lett.* **103**(8), 083111 (2013).
- <sup>51</sup>L. Maugeri, L. Simonelli, A. Iadecola, B. Joseph, M. Okubo, I. Honma, H. Wadati, T. Mizokawa, and N. L. Saini, *J. Power Sources* **229**, 272–276 (2013).
- <sup>52</sup>M. Okubo, J. Kim, T. Kudo, H. Zhou, and I. Honma, *J. Phys. Chem. C* **113**(34), 15337–15342 (2009).
- <sup>53</sup>M. Okubo, E. Hosono, J. Kim, M. Enomoto, N. Kojima, T. Kudo, H. Zhou, and I. Honma, *J. Am. Chem. Soc.* **129**(23), 7444–7452 (2007).
- <sup>54</sup>D. Qian, Y. Hinuma, H. Chen, L.-S. Du, K. J. Carroll, G. Ceder, C. P. Grey, and Y. S. Meng, *J. Am. Chem. Soc.* **134**(14), 6096–6099 (2012).
- <sup>55</sup>N. Andreu, I. Baraille, H. Martinez, R. Dedryvère, M. Loudet, and D. Gonbeau, *J. Phys. Chem. C* **116**(38), 20332–20341 (2012).
- <sup>56</sup>L. Dahéron, R. Dedryvère, H. Martinez, D. Flahaut, M. Ménétrier, C. Delmas, and D. Gonbeau, *Chem. Mater.* **21**(23), 5607–5616 (2009).
- <sup>57</sup>R. Dedryvère, M. Maccario, L. Croguennec, F. Le Cras, C. Delmas, and D. Gonbeau, *Chem. Mater.* **20**(22), 7164–7170 (2008).
- <sup>58</sup>P. Verma, P. Maire, and P. Novák, *Electrochim. Acta* **55**(22), 6332–6341 (2010).
- <sup>59</sup>D. Aurbach, B. Markovsky, G. Salitra, E. Markevich, Y. Talyossef, M. Koltypin, L. Nazar, B. Ellis, and D. Kovacheva, *J. Power Sources* **165**(2), 491–499 (2007).
- <sup>60</sup>K. Edström, T. Gustafsson, and J. O. Thomas, *Electrochim. Acta* **50**(2), 397–403 (2004).
- <sup>61</sup>G. Cherkashinin, M. Motzko, N. Schulz, T. Späth, and W. Jaegermann, *Chem. Mater.* **27**(8), 2875–2887 (2015).
- <sup>62</sup>T. Eriksson, A. M. Andersson, C. Gejke, T. Gustafsson, and J. O. Thomas, *Langmuir* **18**(9), 3609–3619 (2002).
- <sup>63</sup>Y.-C. Lu, A. N. Mansour, N. Yabuuchi, and Y. Shao-Horn, *Chem. Mater.* **21**(19), 4408–4424 (2009).
- <sup>64</sup>N. Yabuuchi, K. Yoshii, S.-T. Myung, I. Nakai, and S. Komaba, *J. Am. Chem. Soc.* **133**(12), 4404–4419 (2011).
- <sup>65</sup>G. Martens and P. Rabe, *Phys. Status Solidi A* **58**(2), 415–424 (1980).



- <sup>66</sup>D. Takamatsu, Y. Koyama, Y. Orikasa, S. Mori, T. Nakatsutsumi, T. Hirano, H. Tanida, H. Arai, Y. Uchimoto, and Z. Ogumi, *Angew. Chem. Int. Ed.* **51**(46), 11597–11601 (2012).
- <sup>67</sup>Y. Koyama, H. Arai, I. Tanaka, Y. Uchimoto, and Z. Ogumi, *Chem. Mater.* **24**(20), 3886–3894 (2012).
- <sup>68</sup>M. Hirayama, N. Sonoyama, M. Ito, M. Minoura, D. Mori, A. Yamada, K. Tamura, J. I. Mizuki, and R. Kanno, *J. Electrochem. Soc.* **154**(11), A1065 (2007).
- <sup>69</sup>M. Hirayama, N. Sonoyama, T. Abe, M. Minoura, M. Ito, D. Mori, A. Yamada, R. Kanno, T. Terashima, M. Takano, K. Tamura, and J. I. Mizuki, *J. Power Sources* **168**(2), 493–500 (2007).
- <sup>70</sup>M. Hirayama, K. Sakamoto, T. Hiraide, D. Mori, A. Yamada, R. Kanno, N. Sonoyama, K. Tamura, and J. I. Mizuki, *Electrochim. Acta* **53**(2), 871–881 (2007).
- <sup>71</sup>M. Hirayama, H. Ido, K. Kim, W. Cho, K. Tamura, J. I. Mizuki, and R. Kanno, *J. Am. Chem. Soc.* **132**(43), 15268–15276 (2010).
- <sup>72</sup>M. Hirayama, M. Yonemura, K. Suzuki, N. Torikai, H. Smith, E. Watkinsand, J. Majewski, and R. Kanno, *Electrochemistry* **78**(5), 413–415 (2010).
- <sup>73</sup>A. Uysal, H. Zhou, G. Feng, S. S. Lee, S. Li, P. Fenter, P. T. Cummings, P. F. Fulvio, S. Dai, J. K. McDonough, and Y. Gogotsi, *J. Phys. Chem. C* **118**(1), 569–574 (2014).
- <sup>74</sup>R. Yamamoto, H. Morisaki, O. Sakata, H. Shimotani, H. Yuan, Y. Iwasa, T. Kimura, and Y. Wakabayashi, *Appl. Phys. Lett.* **101**(5), 053122 (2012).
- <sup>75</sup>Y. Lauw, M. D. Horne, T. Rodopoulos, V. Lockett, B. Akgun, W. A. Hamilton, and A. R. J. Nelson, *Langmuir* **28**(19), 7374–7381 (2012).
- <sup>76</sup>M. Mezger, S. Schramm, H. Schröder, H. Reichert, M. Deutsch, E. J. D. Souza, J. S. Okasinski, B. M. Ocko, V. Honkimäki, and H. Dosch, *J. Chem. Phys.* **131**(9), 094701 (2009).
- <sup>77</sup>M. Mezger, H. Schröder, H. Reichert, S. Schramm, J. S. Okasinski, S. Schöder, V. Honkimäki, M. Deutsch, B. M. Ocko, J. Ralston, M. Rohwerder, M. Stratmann, and H. Dosch, *Science* **322**(5900), 424 (2008).
- <sup>78</sup>K. Sakamoto, M. Hirayama, N. Sonoyama, D. Mori, A. Yamada, K. Tamura, J. I. Mizuki, and R. Kanno, *Chem. Mater.* **21**(13), 2632–2640 (2009).
- <sup>79</sup>R. Hausbrand, *J. Chem. Phys.* **152**(18), 180902 (2020).
- <sup>80</sup>D. Becker, G. Cherkashinin, R. Hausbrand, and W. Jaegermann, *J. Phys. Chem. C* **118**(2), 962–967 (2014).
- <sup>81</sup>D. Ensling, G. Cherkashinin, S. Schmid, S. Bhuvanewari, A. Thissen, and W. Jaegermann, *Chem. Mater.* **26**(13), 3948–3956 (2014).
- <sup>82</sup>H. Liu, Y. Tong, N. Kuwata, M. Osawa, J. Kawamura, and S. Ye, *J. Phys. Chem. C* **113**(48), 20531–20534 (2009).
- <sup>83</sup>L. Yu, H. Liu, Y. Wang, N. Kuwata, M. Osawa, J. Kawamura, and S. Ye, *Angew. Chem. Int. Ed.* **52**(22), 5753–5756 (2013).
- <sup>84</sup>M. Mladenov, R. Stoyanova, E. Zhecheva, and S. Vassilev, *Electrochem. Commun.* **3**(8), 410–416 (2001).
- <sup>85</sup>L. J. Fu, H. Liu, C. Li, Y. P. Wu, E. Rahm, R. Holze, and H. Q. Wu, *Solid State Sci.* **8**(2), 113–128 (2006).
- <sup>86</sup>S. T. Myung, K. Amine, and Y. K. Sun, *J. Mater. Chem.* **20**(34), 7074–7095 (2010).
- <sup>87</sup>H. Liu, Y. P. Wu, E. Rahm, R. Holze, and H. Q. Wu, *J. Solid State Electrochem.* **8**(7), 450–466 (2004).
- <sup>88</sup>H. Zhao, L. Gao, W. Qiu, and X. Zhang, *J. Power Sources* **132**(1–2), 195–200 (2004).
- <sup>89</sup>Y. Orikasa, D. Takamatsu, K. Yamamoto, Y. Koyama, S. Mori, T. Masese, T. Mori, T. Minato, H. Tanida, T. Uruga, Z. Ogumi, and Y. Uchimoto, *Adv. Mater. Interfaces* **1**(9), 1400195 (2014).
- <sup>90</sup>K. Yamamoto, Y. Orikasa, D. Takamatsu, Y. Koyama, S. Mori, T. Masese, T. Mori, T. Minato, H. Tanida, T. Uruga, Z. Ogumi, and Y. Uchimoto, *Electrochemistry* **82**(10), 891–896 (2014).
- <sup>91</sup>D. Takamatsu, S. Mori, Y. Orikasa, T. Nakatsutsumi, Y. Koyama, H. Tanida, H. Arai, Y. Uchimoto, and Z. Ogumi, *J. Electrochem. Soc.* **160**(5), A3054–A3060 (2013).
- <sup>92</sup>D. Takamatsu, Y. Orikasa, S. Mori, T. Nakatsutsumi, K. Yamamoto, Y. Koyama, T. Minato, T. Hirano, H. Tanida, H. Arai, Y. Uchimoto, and Z. Ogumi, *J. Phys. Chem. C* **119**(18), 9791–9797 (2015).
- <sup>93</sup>K. Yamamoto, T. Minato, S. Mori, D. Takamatsu, Y. Orikasa, H. Tanida, K. Nakanishi, H. Murayama, T. Masese, T. Mori, H. Arai, Y. Koyama, Z. Ogumi, and Y. Uchimoto, *J. Phys. Chem. C* **118**(18), 9538–9543 (2014).
- <sup>94</sup>H. Kawaura, D. Takamatsu, S. Mori, Y. Orikasa, H. Sugaya, H. Murayama, K. Nakanishi, H. Tanida, Y. Koyama, H. Arai, Y. Uchimoto, and Z. Ogumi, *J. Power Sources* **245**, 816–821 (2014).
- <sup>95</sup>H. Oh, H. Yamagishi, T. Ohta, and H. R. Byon, *Mater. Chem. Front.* **5**, 3657–3663 (2021).
- <sup>96</sup>Y. Y. Li, H. R. Chen, K. Lim, H. D. Deng, J. Lim, D. Fraggadakis, P. M. Attia, S. C. Lee, N. Jin, J. Moskon, Z. X. Guan, W. E. Gent, J. Hong, Y. S. Yu, M. Gaberscek, M. S. Islam, M. Z. Bazant, and W. C. Chueh, *Nat. Mater.* **17**(10), 915–922 (2018).
- <sup>97</sup>N. Ohta, K. Takada, L. Zhang, R. Ma, M. Osada, and T. Sasaki, *Adv. Mater.* **18**(17), 2226–2229 (2006).
- <sup>98</sup>K. Takada, N. Ohta, L. Zhang, K. Fukuda, I. Sakaguchi, R. Ma, M. Osada, and T. Sasaki, *Solid State Ionics* **179**(27), 1333–1337 (2008).
- <sup>99</sup>N. Ohta, K. Takada, I. Sakaguchi, L. Zhang, R. Ma, K. Fukuda, M. Osada, and T. Sasaki, *Electrochem. Commun.* **9**(7), 1486–1490 (2007).
- <sup>100</sup>K. Takada, N. Ohta, L. Zhang, X. Xu, B. T. Hang, T. Ohnishi, M. Osada, and T. Sasaki, *Solid State Ionics* **225**, 594–597 (2012).
- <sup>101</sup>Y. Zhu, X. He, and Y. Mo, *ACS Appl. Mater. Interfaces* **7**(42), 23685–23693 (2015).
- <sup>102</sup>W. D. Richards, L. J. Miara, Y. Wang, J. C. Kim, and G. Ceder, *Chem. Mater.* **28**(1), 266–273 (2016).
- <sup>103</sup>A. Sakuda, A. Hayashi, and M. Tatsumisago, *Chem. Mater.* **22**(3), 949–956 (2010).
- <sup>104</sup>K. Chen, K. Yamamoto, Y. Orikasa, T. Uchiyama, Y. Ito, S. Yubuchi, A. Hayashi, M. Tatsumisago, K. Nitta, T. Uruga, and Y. Uchimoto, *Solid State Ionics* **327**, 150–156 (2018).
- <sup>105</sup>A. K. Padhi, K. S. Nanjundaswamy, and J. B. Goodenough, *J. Electrochem. Soc.* **144**(4), 1188–1194 (1997).
- <sup>106</sup>B. Kang and G. Ceder, *Nature* **458**(7235), 190–193 (2009).
- <sup>107</sup>S. Y. Chung, J. T. Bloking, and Y. M. Chiang, *Nat. Mater.* **1**(2), 123–128 (2002).
- <sup>108</sup>A. Yamada, S. C. Chung, and K. Hinokuma, *J. Electrochem. Soc.* **148**(3), A224–A229 (2001).
- <sup>109</sup>P. P. Prosvini, D. Zane, and M. Pasquali, *Electrochim. Acta* **46**(23), 3517–3523 (2001).
- <sup>110</sup>A. Yamada, H. Koizumi, S. I. Nishimura, N. Sonoyama, R. Kanno, M. Yonemura, T. Nakamura, and Y. Kobayashi, *Nat. Mater.* **5**(5), 357–360 (2006).
- <sup>111</sup>V. Srinivasan and J. Newman, *J. Electrochem. Soc.* **151**(10), A1517–A1529 (2004).
- <sup>112</sup>C. Wang, U. S. Kasavajjula, and P. E. Arce, *J. Phys. Chem.* **111**, 16656 (2007).
- <sup>113</sup>U. S. Kasavajjula, C. Wang, and P. E. Arce, *J. Electrochem. Soc.* **155**, A866 (2008).
- <sup>114</sup>D. Morgan, A. Van der Ven, and G. Ceder, *Electrochem. Solid-State Lett.* **7**(2), A30–A32 (2004).
- <sup>115</sup>M. S. Islam, D. J. Driscoll, C. A. J. Fisher, and P. R. Slater, *Chem. Mater.* **17**(2), 5085–5092 (2005).
- <sup>116</sup>G. Y. Chen, X. Y. Song, and T. J. Richardson, *Electrochem. Solid-State Lett.* **9**(6), A295–A298 (2006).
- <sup>117</sup>L. Laffont, C. Delacourt, P. Gibot, M. Y. Wu, P. Kooyman, C. Masquelier, and J. M. Tarascon, *Chem. Mater.* **18**(23), 5520–5529 (2006).
- <sup>118</sup>C. Delmas, M. Maccario, L. Croguennec, F. Le Cras, and F. Weill, *Nat. Mater.* **7**(8), 665–671 (2008).
- <sup>119</sup>P. P. Prosvini, *J. Electrochem. Soc.* **152**(10), A1925–A1929 (2005).
- <sup>120</sup>N. Meethong, Y. H. Kao, W. C. Carter, and Y. M. Chiang, *Chem. Mater.* **22**(3), 1088–1097 (2010).
- <sup>121</sup>M. Tang, H. Y. Huang, N. Meethong, Y. H. Kao, W. C. Carter, and Y. M. Chiang, *Chem. Mater.* **21**(8), 1557–1571 (2009).
- <sup>122</sup>R. Malik, F. Zhou, and G. Ceder, *Nat. Mater.* **10**(8), 587–590 (2011).
- <sup>123</sup>P. Bai, D. A. Cogswell, and M. Z. Bazant, *Nano Lett.* **11**(11), 4890–4896 (2011).
- <sup>124</sup>W. Dreyer, J. Jannik, C. Guhlke, R. Huth, J. Moskon, and M. Gaberscek, *Nat. Mater.* **9**(5), 448–453 (2010).
- <sup>125</sup>C. V. Ramana, A. Mauger, F. Gendron, C. M. Julien, and K. Zaghib, *J. Power Sources* **187**(2), 555–564 (2009).
- <sup>126</sup>T. Ichitsubo, K. Tokuda, S. Yagi, M. Kawamori, T. Kawaguchi, T. Doi, M. Oishi, and E. Matsubara, *J. Mater. Chem. A* **1**(7), 2567–2577 (2013).
- <sup>127</sup>Y. H. Kao, M. Tang, N. Meethong, J. M. Bai, W. C. Carter, and Y. M. Chiang, *Chem. Mater.* **22**(21), 5845–5855 (2010).
- <sup>128</sup>Y. Orikasa, T. Maeda, Y. Koyama, H. Murayama, K. Fukuda, H. Tanida, H. Arai, E. Matsubara, Y. Uchimoto, and Z. Ogumi, *J. Am. Chem. Soc.* **135**(15), 5497–5500 (2013).

- <sup>129</sup>N. N. Bramnik, K. Nikolowski, C. Baehtz, K. G. Bramnik, and H. Ehrenberg, *Chem. Mater.* **19**(4), 908–915 (2007).
- <sup>130</sup>H. Liu, F. C. Strobridge, O. J. Borkiewicz, K. M. Wiaderek, K. W. Chapman, P. J. Chupas, and C. P. Grey, *Science* **344**(6191), 1252817 (2014).
- <sup>131</sup>J. J. Wang, Y. C. K. Chen-Wiegart, and J. Wang, *Nat. Commun.* **5**, 4570 (2014).
- <sup>132</sup>X. Y. Zhang, M. van Hulzen, D. P. Singh, A. Brownrigg, J. P. Wright, N. H. van Dijk, and M. Wagemaker, *Nano Lett.* **14**(5), 2279–2285 (2014).
- <sup>133</sup>Y. Koyama, T. Uyama, Y. Orikasa, T. Naka, H. Komatsu, K. Shimoda, H. Murayama, K. Fukuda, H. Arai, E. Matsubara, Y. Uchimoto, and Z. Ogumi, *Chem. Mater.* **29**(7), 2855–2863 (2017).
- <sup>134</sup>G. Y. Chen, X. Y. Song, and T. J. Richardson, *J. Electrochem. Soc.* **154**(7), A627–A632 (2017).
- <sup>135</sup>C. Delacourt, P. Poizot, J. M. Tarascon, and C. Masquelier, *Nat. Mater.* **4**(3), 254–260 (2005).
- <sup>136</sup>S.-I. Nishimura, R. Natsui, and A. Yamada, *Angew. Chem. Int. Ed.* **54**(31), 8939–8942 (2015).
- <sup>137</sup>F. Boucher, J. Gaubicher, M. Cuisinier, D. Guyomard, and P. Moreau, *J. Am. Chem. Soc.* **136**(25), 9144–9157 (2014).
- <sup>138</sup>J. Lu, G. Oyama, S.-I. Nishimura, and A. Yamada, *Chem. Mater.* **28**(4), 1101–1106 (2016).
- <sup>139</sup>M. van Hulzen, F. G. B. Ooms, J. P. Wright, and M. Wagemaker, *Front. Energy Res.* **6**, 59 (2018).
- <sup>140</sup>X. Y. Zhang, M. van Hulzen, D. P. Singh, A. Brownrigg, J. P. Wright, N. H. van Dijk, and M. Wagemaker, *Nat. Commun.* **6**, 8333 (2015).
- <sup>141</sup>H. Komatsu, H. Arai, Y. Koyama, K. Sato, T. Kato, R. Yoshida, H. Murayama, I. Takahashi, Y. Orikasa, K. Fukuda, T. Hirayama, Y. Ikuhara, Y. Ukyo, Y. Uchimoto, and Z. Ogumi, *Adv. Energy Mater.* **5**(17), 1500638 (2015).
- <sup>142</sup>Y. N. Zhou, J. L. Yue, E. Y. Hu, H. Li, L. Gu, K. W. Nam, S. M. Bak, X. Q. Yu, J. Liu, J. M. Bai, E. Dooryhee, Z. W. Fu, and X. Q. Yang, *Adv. Energy Mater.* **6**(21), 1600597 (2016).
- <sup>143</sup>J. Lim, Y. Li, D. H. Alsem, H. So, S. C. Lee, P. Bai, D. A. Cogswell, X. Liu, N. Jin, Y.-S. Yu, N. J. Salmon, D. A. Shapiro, M. Z. Bazant, T. Tyliszczak, and W. C. Chueh, *Science* **353**(6299), 566–571 (2016).
- <sup>144</sup>T. Yoshinari, T. Mori, K. Otani, T. Munesada, K. Yamamoto, T. Uchiyama, K. Fukuda, Y. Koyama, R. Hagiwara, Y. Orikasa, and Y. Uchimoto, *Chem. Mater.* **31**(18), 7160–7166 (2019).
- <sup>145</sup>T. Yoshinari, K. Yamamoto, M. Nishijima, K. Fukuda, A. Kuwabara, I. Tanaka, K. Maeda, H. Kageyama, Y. Orikasa, and Y. Uchimoto, *ACS Appl. Energy Mater.* **1**(12), 6736–6740 (2018).
- <sup>146</sup>M. Nishijima, T. Ootani, Y. Kamimura, T. Sueki, S. Esaki, S. Murai, K. Fujita, K. Tanaka, K. Ohira, Y. Koyama, and I. Tanaka, *Nat. Commun.* **5**(1), 4553 (2014).
- <sup>147</sup>H. Fujimoto, H. Kiuchi, S. Takagi, K. Shimoda, K.-I. Okazaki, Z. Ogumi, and T. Abe, *J. Electrochem. Soc.* **168**(4), 040509 (2021).
- <sup>148</sup>W. Zhang, D.-H. Seo, T. Chen, L. Wu, M. Topsakal, Y. Zhu, D. Lu, G. Ceder, and F. Wang, *Science* **367**(6481), 1030–1034 (2020).
- <sup>149</sup>X. Lu, A. Bertei, D. P. Finegan, C. Tan, S. R. Daemi, J. S. Weaving, K. B. O'Regan, T. M. M. Heenan, G. Hinds, E. Kendrick, D. J. L. Brett, and P. R. Shearing, *Nat. Commun.* **11**(1), 2079 (2020).
- <sup>150</sup>Y. Orikasa, Y. Gogyo, H. Yamashige, M. Katayama, K. Z. Chen, T. Mori, K. Yamamoto, T. Masese, Y. Inada, T. Ohta, Z. Siroma, S. Kato, H. Kinoshita, H. Arai, Z. Ogumi, and Y. Uchimoto, *Sci. Rep.* **6**, 26382 (2016).
- <sup>151</sup>K. Tachibana, T. Suzuki, C. Kanno, T. Endo, T. Ogata, T. Shimizu, S. Kohara, and T. Nishina, *Electrochemistry* **71**(12), 1226–1230 (2003).
- <sup>152</sup>I. V. Thorat, D. E. Stephenson, N. A. Zacharias, K. Zaghib, J. N. Harb, and D. R. Wheeler, *J. Power Sources* **188**(2), 592–600 (2009).
- <sup>153</sup>C. Fongy, A. C. Gaillot, S. Jouanneau, D. Guyomard, and B. Lestriez, *J. Electrochem. Soc.* **157**(7), A885–A891 (2010).
- <sup>154</sup>C. Fongy, S. Jouanneau, D. Guyomard, J. C. Badot, and B. Lestriez, *J. Electrochem. Soc.* **157**(12), A1347–A1353 (2010).
- <sup>155</sup>J. Shim and K. A. Striebel, *J. Power Sources* **119–121**, 934–937 (2003).
- <sup>156</sup>J. S. Gnanaraj, Y. S. Cohen, M. D. Levi, and D. Aurbach, *J. Electroanal. Chem.* **516**(1), 89–102 (2001).
- <sup>157</sup>M. Doyle, T. F. Fuller, and J. Newman, *J. Electrochem. Soc.* **140**(6), 1526–1533 (1993).
- <sup>158</sup>S.-H. Ng, F. La Mantia, and P. Novák, *Angew. Chem. Int. Ed.* **48**(3), 528–532 (2009).
- <sup>159</sup>K. C. Hess, W. K. Epting, and S. Litster, *Anal. Chem.* **83**(24), 9492–9498 (2011).
- <sup>160</sup>L. O. Valoen and J. N. Reimers, *J. Electrochem. Soc.* **152**(5), A882–A891 (2005).
- <sup>161</sup>M. S. Ding, K. Xu, S. S. Zhang, K. Amine, G. L. Henriksen, and T. R. Jow, *J. Electrochem. Soc.* **148**(10), A1196–A1204 (2001).
- <sup>162</sup>T. F. Fuller, M. Doyle, and J. Newman, *J. Electrochem. Soc.* **141**(1), 1–10 (1994).
- <sup>163</sup>T. F. Fuller, M. Doyle, and J. Newman, *J. Electrochem. Soc.* **141**(4), 982–990 (1994).
- <sup>164</sup>K. C. Hess, J. F. Whitacre, and S. Litster, *J. Electrochem. Soc.* **159**(8), A1351–A1359 (2012).
- <sup>165</sup>K. Mitsuda and D. Takemura, *Electrochemistry* **76**(12), 880–885 (2008).
- <sup>166</sup>P. Maire, A. Evans, H. Kaiser, W. Scheifele, and P. Novák, *J. Electrochem. Soc.* **155**(11), A862 (2008).
- <sup>167</sup>H. Arai, A. Yaguchi, Y. Nishimura, Y. Akimoto, and A. Ikezawa, *J. Phys. Chem. C* **125**(7), 3776–3780 (2021).
- <sup>168</sup>J. Nanda, J. Remillard, A. O'Neill, D. Bernardi, T. Ro, K. E. Nietering, J. Y. Go, and T. J. Miller, *Adv. Funct. Mater.* **21**(17), 3282–3290 (2011).
- <sup>169</sup>M. Otoyama, Y. Ito, A. Hayashi, and M. Tatsumisago, *Chem. Lett.* **45**(7), 810–812 (2016).
- <sup>170</sup>Y. Terada, H. Tanida, T. Uruga, A. Takeuchi, Y. Suzuki, and S. Goto, *AIP Conf. Proc.* **1365**(1), 172–175 (2011).
- <sup>171</sup>H. Tanida, H. Yamashige, Y. Orikasa, Y. Gogyo, H. Arai, Y. Uchimoto, and Z. Ogumi, *J. Phys. Chem. C* **120**(9), 4739–4743 (2016).
- <sup>172</sup>H. Murayama, K. Kitada, K. Fukuda, A. Mitsui, K. Ohara, H. Arai, Y. Uchimoto, Z. Ogumi, and E. Matsubara, *J. Phys. Chem. C* **118**(36), 20750–20755 (2014).
- <sup>173</sup>M. Katayama, K. Sumiwaka, K. Hayashi, K. Ozutsumi, T. Ohta, and Y. Inada, *J. Synchrotron Radiat.* **19**, 717–721 (2012).
- <sup>174</sup>Z. Siroma, J. Hagiwara, K. Yasuda, M. Inaba, and A. Tasaka, *J. Electroanal. Chem.* **648**(2), 92–97 (2010).
- <sup>175</sup>S. Taminato, M. Yonemura, S. Shiotani, T. Kamiyama, S. Torii, M. Nagao, Y. Ishikawa, K. Mori, T. Fukunaga, Y. Onodera, T. Naka, M. Morishima, Y. Ukyo, D. S. Adipranoto, H. Arai, Y. Uchimoto, Z. Ogumi, K. Suzuki, M. Hirayama, and R. Kanno, *Sci. Rep.* **6**(1), 28843 (2016).
- <sup>176</sup>X. Zhang, T. W. Verhallen, F. Labohm, and M. Wagemaker, *Adv. Energy Mater.* **5**(15), 1500498 (2015).
- <sup>177</sup>H. Liu, S. Kazemiabnavi, A. Grenier, G. Vaughan, M. D. Michiel, B. J. Polzin, K. Thornton, K. W. Chapman, and P. J. Chupas, *ACS Appl. Mater. Interfaces* **11**(20), 18386–18394 (2019).
- <sup>178</sup>M. Klett, M. Giesecke, A. Nyman, F. Hallberg, R. W. Lindström, G. Lindbergh, and I. Furó, *J. Am. Chem. Soc.* **134**(36), 14654–14657 (2012).
- <sup>179</sup>S. A. Krachkovskiy, J. D. Bazak, P. Werhun, B. J. Balcom, I. C. Halalay, and G. R. Goward, *J. Am. Chem. Soc.* **138**(25), 7992–7999 (2016).
- <sup>180</sup>D. Takamatsu, A. Yoneyama, Y. Asari, and T. Hirano, *J. Am. Chem. Soc.* **140**(5), 1608–1611 (2018).
- <sup>181</sup>J. I. G. Dawkins, M. Z. Ghavidel, D. Chhin, I. Beaulieu, M. S. Hossain, R. Feng, J. Mauzeroll, and S. B. Schougaard, *Anal. Chem.* **92**(16), 10908–10912 (2020).
- <sup>182</sup>A. C. Forse, J. M. Griffin, C. Merlet, J. Carretero-Gonzalez, A. Rahman, O. Raji, N. M. Trease, and C. P. Grey, *Nat. Energy* **2**(3), 16216 (2017).
- <sup>183</sup>K. Kitada, H. Murayama, K. Fukuda, H. Arai, Y. Uchimoto, and Z. Ogumi, *J. Phys. Chem. C* **121**(11), 6018–6023 (2017).
- <sup>184</sup>K. Kitada, H. Murayama, K. Fukuda, H. Arai, Y. Uchimoto, Z. Ogumi, and E. Matsubara, *J. Power Sources* **301**, 11–17 (2016).
- <sup>185</sup>Z. Li, L. Yin, G. S. Mattei, M. R. Cosby, B.-S. Lee, Z. Wu, S.-M. Bak, K. W. Chapman, X.-Q. Yang, P. Liu, and P. G. Khalifah, *Chem. Mater.* **32**(15), 6358–6364 (2020).
- <sup>186</sup>H. Buschmann, J. Dolle, S. Berendts, A. Kuhn, P. Bottke, M. Wilkening, P. Heitjans, A. Senyshyn, H. Ehrenberg, A. Lotnyk, V. Duppel, L. Kienle, and J. Janek, *Phys. Chem. Chem. Phys.* **13**(43), 19378–19392 (2011).
- <sup>187</sup>K. Minami, F. Mizuno, A. Hayashi, and M. Tatsumisago, *Solid State Ionics* **178**(11–12), 837–841 (2007).
- <sup>188</sup>K. Kandori, H. Yamashige, N. Furuta, T. Nonaka, and Y. Orikasa, *Electrochemistry* **87**(3), 182–187 (2019).
- <sup>189</sup>Y. Kato, S. Hori, T. Saito, K. Suzuki, M. Hirayama, A. Mitsui, M. Yonemura, H. Iba, and R. Kanno, *Nat. Energy* **1**(4), 16030 (2016).
- <sup>190</sup>Y. Kimura, A. Tomura, M. Fakkao, T. Nakamura, N. Ishiguro, O. Sekizawa, K. Nitta, T. Uruga, T. Okumura, M. Tada, Y. Uchimoto, and K. Amezawa, *J. Phys. Chem. Lett.* **11**(9), 3629–3636 (2020).